2020年 3月期
関西大学審査学位論文

Graduate School of Science and Engineering, Kansai University

Nano Physics and Engineering laboratory

Ph. D thesis

Formation of Organic or Inorganic Nanostructures onto Quartz Crystal Microbalance (QCM)-based Biosensor for Improving the Sensing Performance

17D6003

Naoto Asai

Supervisor

Prof. Takeshi Ito

March 2020

2020 年 3 月 関西大学審査学位論文

Formation of Organic or Inorganic Nanostructures onto Quartz Crystal Microbalance (QCM)-based Biosensor for Improving the Sensing Performance

有機・無機ナノ構造を用いた水晶振動子マイクロバランス法の開発とバイオセンサへの応用

関西大学

理工学研究科　総合理工学専攻

ナノ機能物理工学研究室

17D6003

浅井　直人

指導教員　　伊藤　健

Contents

Abstract

【論文要旨】

バイオセンサは，測定対象物を特異的に認識，結合する生体関連物質を検出素子とし，その結合反応を電気信号などの検出可能な信号へ変換するトランスデューサーから構成される．バイオセンサは，医療や健康分野への応用が期待されており，血糖値測定器や妊娠検査キットなど個人が自身の健康状態をチェックする目的に利用されている．バイオセンサの主な課題は，測定試料の微量化，測定感度の向上，測定コストの低減，携帯性の向上などが考えられる．

水晶振動子マイクロバランス(quartz crystal microbalance: QCM)法を利用したバイオセンサは，薄片水晶の両面に電圧印加用の薄膜電極を有する構造を持ち，小型，安価，リアルタイムに測定対象物の検出が可能など多くの利点を有する．QCM 法では，電極上に付着した物質の質量と水晶の固有周波数の変化量が比例することが知られている．そのため，低分子量物質の高感度測定が困難である．センサ電極上にナノ構造を作製し，検出素子を高密度に配列する方法で QCM 法を利用したバイオセンサの高感度化を図った研究が報告されている．しかし，これらの報告では電子線リソグラフィや化学気相成長法を用いてナノ構造を作製しているため，構造の制御が困難かつ，十分な高感度化が果たされてこなかった．また，これらの装置は真空装置と高価な材料を用いるため，ナノ構造の作製コストが高額になる．加えて，センチメートルスケールの面積にナノ構造を作製する場合，作製時間が長期化することも作製コストの増加の一因となる．真空装置によって作製したナノ構造に対し，簡易にナノ構造を形成できる酸化チタン，酸化亜鉛，カーボンナノチューブなどのナノ材料が注目されているが，ナノ構造表面上に特異的な官能基を有さないため，バイオセンサに用いる生体分子を固定する手段が限られる．

本論文では QCM 法を用いたバイオセンサにおいて①湿式プロセスを用

いた大きな比表面積を有する無機ナノ構造と②デオキシリボ核酸(DNA)に基づいた無数の検出素子（アプタマー）を有する有機ナノ構造(DNA origami)を形成することでセンシング性能の向上を試みた結果について報告する．①については冒頭で述べたように，比表面積の大きなナノ構造の表面上に検出素子を高密度に配列することで，より多量の分析物を捕捉することができるため検出シグナルの増幅が果たされる．②については，多量のアプタマーをシート状のDNA origami の任意の場所に配列し，その密度を制御することで多量の分析物の捕捉とシグナルの増幅を図った．

第 2 章では，金電極の陽極酸化によりスポンジ状の金ナノ多孔質構造をQCM センサの電極表面に形成した．印加電圧を調整することで，2 種類の金ナノ多孔質構造が形成された．それぞれの実効表面積は電気化学測定により評価し，真に大きな表面積を有する金ナノ構造の選定をした．QCM 測定では，金ナノ多孔質電極または平面電極を備えた QCM センサを使って抗原抗体相互作用を測定した．両方のセンサで得られた質量変化を比較し，それぞれの検知性能を評価した．比較の結果，金ナノ構造を電極に形成することで，抗原抗体反応による質量変化量が増大した．QCM 測定後，金の多孔質ナノ構造を走査型電子顕微鏡および原子間力顕微鏡で観察し，表面状態を評価した．測定時のバッファーの送液によって，金ナノ多孔質電極が破壊されていることが明らかになった．

第 3 章では，金樹状構造を電気めっきによって QCM センサの金電極上に形成した．溶液中のポリエチレングリコール 1000（PEG1000）濃度と印加電圧を制御し、分岐構造の成長促進を試みた．50 ppm の PEG1000 を含むめっき液中で-0.95 V の電圧を電極に印加することで，最大の実効表面積を有する金樹状構造を得た．また，印加電圧と PEG1000 濃度がめっきに及ぼす影響を走査型電子顕微鏡を用いて評価した．液中の QCM センサの共振抵抗をアドミタンス測定によって測定した．背の高い金樹状構造を電極上に形成すると，QCM センサの共振抵抗が増大し，測定時のノイズに起因することが明らかに

なった． 金樹状構造の有効性を示すため，樹状電極または平面電極を備えた QCM センサを用いて抗原抗体相互作用を検出した．両方のセンサで得られた質量変化を比較し，それぞれの検知性能を評価した．

第 4 章では，水晶上に製膜したアルミニウムを陽極酸化することで，陽極酸化アルミナを電極とする AAO ナノ構造 QCM センサを作製した。この陽極酸化アルミナのナノホールの直径と深さを，陽極酸化時間とポストエッチングにより制御した．アドミッタンス測定により，液相における AAO ナノ構造 QCM センサの共振特性を分析した．さらに，ナノホールの寸法は，抗原抗体反応を測定するために最適化した． AAO ナノ構造 QCM センサの検出性能を従来の平らな電極を持つセンサと比較した結果，検出限界が 2 倍向上した．AAO ナノ構造の大きな表面積が感度向上に起因したことが明らかになった．AAO ナノ構造 QCM センサは，2 つ癌関連タンパク質のタンパク質間相互作用の検出にも使用され，PPI の結合定数を算出するに至った．

第 5 章では，アプタマー結合 DNA origami を QCM センサの金電極上に固定した．アプタマーを DNA origami に組み込むために，2 通りのアセンブリ法①2-step アセンブリ法と②One-pot アセンブリ法を検証した．2-step アセンブリ法では，前もって形成した DNA origami とアプタマーを混合し，25℃から 80℃の 8 種類の温度でアニーリングした．この方法では，アニーリング温度が高くなるにつれ，DNA origami を構成する DNA が本体から解離した．対して One-pot アセンブリ法では，アプタマー結合 DNA origami の全ての材料を一つのチューブに混合し，一度のアニーリングでアセンブリした．この結果，欠損がないアプタマー結合 DNA origami が得られた．この One-pot アセンブリ法で，0〜166 個のアプタマーを DNA origami の任意の場所に組み込み，アプタマー結合 DNA origami が特異的タンパク質と結合したときの周波数変化を評価して最適なアプタマーの数を決定した．アプタマーとタンパク質の相互作用の評価によって，周波数変化がアプタマーの数に依存することが明らかになった．最後に，アプタマー結合 DNA origami でコーティングされた QCM センサの検

知性能を，アプタマーだけを修飾した QCM センサを用いて比較した．アプタマー・タンパク質相互作用における周波数変化をそれぞれのセンサで取得し，検出限界を算出した結果，アプタマー結合 DNA origami を有する QCM センサの検出限界は 2 倍向上した．

Chapter 1: Introduction

1.1 Health and disease among human being

People living in a developed country is interested in "quality of life (QOL)" which deals with their health, and safety. QOL has many definitions that are not only objective matters such as health or environment but also subjective matters such as social activity or individual satisfaction. In the medical or health field, a low level of QOL is recognized as aftereffects by medical treatment, such as significant side effects or functional loss after surgery. In particular, it needs a long time to conquer the cancer and lifestyle-related diseases. A delayed treatment has negative effect not only on the patient but also on their family. On the other hand, the number of patients, who are suffering from lifestyle-related diseases such as cancer and diabetes, is increasing in both developed countries and developing countries. According to the World Cancer Report 2014 [1-1] published by the International Agency for Research on Cancer (IARC), the number of cancer cases has been increased about 11 % every year since 1980. The cancer cases are estimated to increase by 150% in 2030, reaching 22 million. Additionally, the economic burden of the people due to cancer amounts to 227 trillion yen. Then, the developed countries are putting pressure on the medical economy. The International Diabetes Federation (IDF) published the Diabetes Atlas 7th Edition 2015 [1-2], reporting that the number of diabetic patients in 2015 reached 415 million worldwide. The number of patients will increase to 642 million by 2040 in the case of no countermeasure. Antimicrobial-resistance bacteria are also threating human-being these decades. 10 million people will be died due to the infection from the bacteria in 2050 [1-3]. The most dangerous thing is that improper treatment for the antimicrobial-resistance bacteria will induce additional resistance for

antibiotic reagents, and transference the source to other people. The standard countermeasure among these diseases is the diagnosis of diseases at an early stage and the start the accurate treatments as soon as possible.

1.2 Requirements for diagnosis

Diagnostic tests are an important factor of a health care system, providing critical information to patients and healthcare providers. The healthcare providers refer the information to decide the correct medical management for the treatment of health and illness. In diagnosis, healthcare provider measures disease biomarkers quantitatively that are essential to monitor and evaluate each stage of diseases. Highly sensitive detection of a target biomarker would realize prophylactic prevention from diseases by drug administration (prophylactic treatment). In addition, a screening of several markers or several signal transductions from receptors enables to prescribe treatments with appropriate effects to individual patient. A molecular-level diagnostic can reveal not only the presence of biomarkers such as genetic material and pathogen quantitatively but also the mechanism of disease at the genetic, protein, or metabolite level. A variety of molecular therapies have been developed, including the development of new therapeutic genes [1-4], nucleic acid formulations that modulate gene expression [1-5], and drug delivery systems using nano-sized particles [1-6]. All methods are known to be effective against diseases that have been treated ineffectively on the conventional surgical treatments, such as radiation therapy, chemotherapy, and immunotherapy.

Blood glucose meters and home pregnancy test kits are some of the most common diagnostic kits today. The general patient can use the kits easily to confirm the existence

of biomarkers in their own sample such as blood. The urine test is another easy kit available to detect proteins, glucose, bilirubin, hemoglobin, leukocytes, and pathogens. However, we do not obtain advanced diagnostic tests with easy-to-use involving immunoassays for multiplex detection of cancer biomarkers [1-7], cell culturing for bacteria [1-8], and rolling cycle amplification of the gene [1-9]. These examinations can be performed at a hospital. Therefore, it is difficult for general patients to manage daily their health status with regular medical examinations by themselves, following reasons.

1. Specialized knowledge and skills are necessary for an inspection.
2. It takes a long time for the test itself and the test results.
3. It is difficult to measure the extremely low concentration of biomarkers by immunochromatography.
4. The general patient gets confused to choose suitable biomarker even if easy-to-use kits of advanced diagnostic tests are developed.
5. There is no device detecting multiple biomarker at once measurement.

In other words, an inspection method requires quick, simple, and inexpensive measurement procedures to take a result. Such an inspection method promotes people to monitor their health condition daily and to create a motive for receiving a medical examination. As a result, the easy-to-use tests are one of goals to lead the prevention and treatment of diseases.

Here, one of the interesting technologies with easy-to-use is introduced: early cancer detection using animals. In 2015, Hirotsu et al. reported a quantitative cancer

screening test using *Caenorhabditis elegans* (*C. elegans*) [1-10]. In the test, one dropwise of urine from patients was used for cancer detection. After the urine was collected from a cancer patient, it was dropped on a dish. *C. elegans* approached to the sample by preference. In contrast, the test showed a negative response against a sample from healthy. *C. elegans* showed chemotaxis against 15 types of cancer with precision of 95% by using 242 patients. In addition, *C. elegans* could determine the sample even in stage 0 or 1. The advantages of cancer test using *C. elegans* are low invasive detection, low cost, and high sensitivity. Therefore, *C. elegans* may have great potential for early detection of any diseases, exceeding other convenient diagnostic kits. Since an animal was employed to this detection method, the management of a culturing environment is complicated for general people. Therefore, a device using *C. elegans* is not suitable for the use at home. One of the approaches to respond to expectations for early detection of disease is "biosensor," which detects their mechanical, chemical, and biological responses in the microenvironment.

1.3 Biosensing technology

Biosensor is an analytical device that utilizes the excellent molecular recognition ability of organisms and biomolecules for capturing the information from chemical/biological reaction. The biorecognition elements are integrated with a physicochemical transducer. The biosensor produces a digital electronic signal that is proportional to the concentration of a specific analyte [1-14]. The basic configuration of biosensor consists of recognition elements and transducers as shown in Fig. 1-1. The

electronic signal is originally resulted from the change of the ion concentration, gases, light intensity, reflectance, or other mechanisms. These chemical/biological changes are converted by the transducer into electrical signals and outputted to display them on a monitor.

Biosensor can cover a very wide range of applications such as disease detection, food safety, defense, and drug discovery. Therefore, improvement of the sensing performance is required to satisfy the purpose on detection of target analyte in the application. The optimization of properties described below is very important to improve the performance of the biosensor.

Selectivity

Selectivity of biosensor depends on the biorecognition elements to detect a specific target analyte in a sample with many contaminants. The best example is depicted by specificity of antigen antibody interaction.

Reproductivity

Reproductivity is to generate identical responses characterized by the precision and accuracy of the transducer and electronics. Reproducible signals provide the same results every time for experiments and high reliability on the response of the biosensor.

Stability

Stability is robustness against ambient disturbances which cause a drift in the output signals and affect on the precision and accuracy in a biosensor. The stability of the biosensor can be attributed to environmental conditions, such as temperature, pressure,

vibration and radio frequency around measurement system, and the affinity of the biorecognition elements.

Sensitivity

Sensitivity is defined as the ability to confirm the presence of analytes at the lowest concentration. The minimum detectable concentration of analyte is defined as detection of limit (LOD) in the sensing system.

Linearity

Linearity is accuracy of the measured response with a straight line against analyte concentration. In preparation of the calibration curve for the biosensor, a variation of measured values against the straight line shows the precision in the sensing system. Linearity of the biosensor is also associated with the sensitivity.

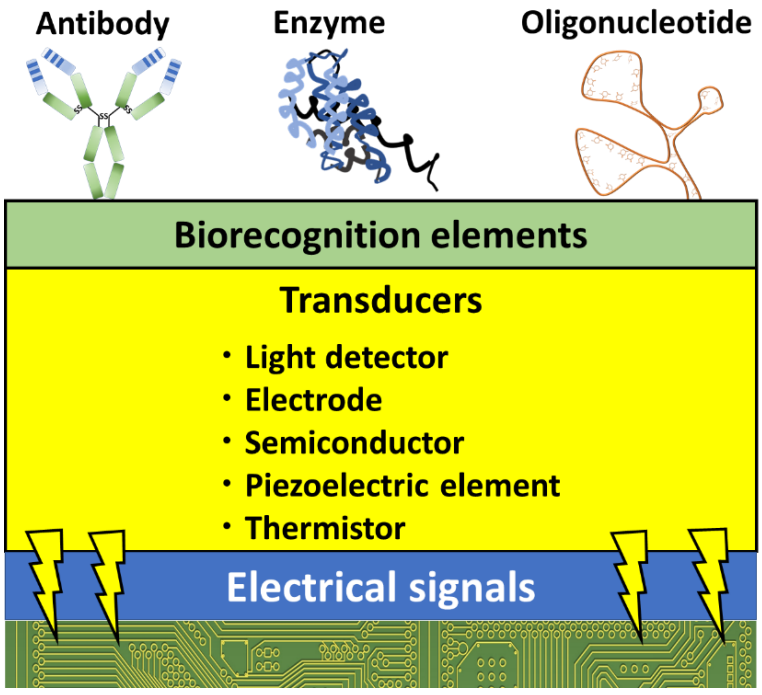

Fig. 1-1 Configuration of biosensor consisted of biorecognition elements and transducers. A chemical reaction is converted to electrical signal via the transducers.

1.4 Recognition elements

Biological materials for the recognition of analyte are classified into two types, enzyme reaction (e. g. enzyme) and affinity types (e. g. antibody and aptamer). First, a sensor using enzyme reaction detects a product from enzymatic reactions associated with the formation of an enzyme-substrate complex transiently. The second sensor uses an antibody that recognize the target analyte specifically and forms a stable complex. It calls as an immunosensor. Immunosensors detect physical and chemical changes associated with stable antigen-antibody reactions. It is important to select the type of biorecognition elements suitable for the detection of the target analyte. Several recognition elements have been utilized below: an antibody [1-15], an oligonucleotide [1-16], or an enzyme [1-17].

1.4.1 Antibody

An antibody is a protein of humoral immunity that is induced *in vivo* as a result of an immune reaction by antigen stimulation. Antibodies are a group of proteins called immunoglobulins (Ig) and are classified into five classes (IgA, IgD, IgE, IgG and IgM). These five immunoglobulins differ in amino acid composition, molecular weight, charge, or sugar content. IgG is mostly contained in the human body and is composed of two identical fragment such as antigen binding (Fab) fragments and constant fragment (Fc), as shown in Fig. 1-2 [1-18]. The Fab fragment consists of the entire light (L) chain and the N-terminal fragment of the heavy (H) chain. The Fc fragment consists of the C-terminal half of the H chain. The antigen binds to the tips of the two Fab regions in the antibody. The H chain and L chain consist of multiple domain structures. A part of the Fab region differs significantly in amino acid sequence between different antibodies, and

a domain containing this part is called variable region (VH and VL). The diversity of the amino acid sequence of the variable region indicates that an organism can produce antibodies recognizing multiple antigens. Among variable regions, there is a hypervariable region having a broad diversity of amino acid sequences. There are three hypervariable regions in each of the H and L chains, and these regions are arranged close to each other with a three-dimensional structure. Moreover, the antigen is determined to bind to the specific antibody at low concentration by this three-dimensional structure with several binding forces such as non-covalent bonds, hydrogen bonds, van der Waals forces, electrostatic interactions, and hydrophobic interactions. Thus, the antibody has been used as a recognition material for the biosensor to measures a target antigen with high sensitivity and selectivity.

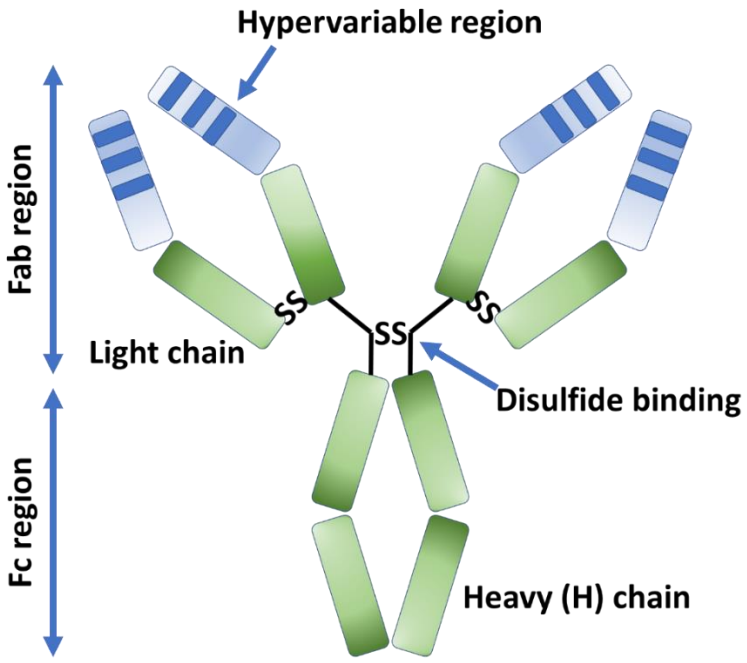

Fig. 1-2 Schematic structure of antibody.

1.4.2 Aptamer

Aptamers are single-stranded RNA or DNA molecules that bind to a target material with high affinity and specificity. The specific aptamer recognizes the target material by taking a complex higher-order structure (conformational change). Aptamers have a wide range of molecular recognizing activity against various materials such as proteins, peptides, antibiotics, and metal ions. Because of its many characteristics, researchers applied it in various fields such as pharmaceuticals and biosensors. The Systematic evolution of ligand by exponential enrichment (SELEX) method to synthesize aptamers was reported in 1990 by the Ellington and Tuerk [1-19, 1-20]. Fig. 1-3 shows the scheme of SELEX method to obtain DNA aptamer by cycling target binding and amplification. In the SELEX method, nucleic acids with the desired activity are screened using a mixture of single-stranded oligo DNAs with different sequences as an initial library. The initial library is chemically synthesized by DNA solid-phase synthesis. The initial library contained approximately 10^{10} to 10^{14} sequences of synthetic oligo DNA. The 40 or 100 bases of the synthetic oligo DNA is used commonly, depending on the screening system and the molecular weight of the target material. For DNA aptamer, the initial library passed an affinity column that immobilized with the target material. The DNA expressing an affinity for the target material is derived from the column and amplified by polymerase chain reaction (PCR). Therefore, a single-stranded DNA is prepared as a secondary library. The amplified library is selected from the initial screening by the affinity column and applied to the next selection again. The repeating these operations concentrates a specific aptamer that binds strongly to the target material. Cloning methods isolate DNA aptamers from the enriched DNA library, and each DNA aptamer is analyzed by sequence analysis and binding affinity. SELEX produces aptamers

with better properties than antibodies as following below.

1. *In vivo* isolation by the SELEX method allows an aptamer to association with several biomaterials such as proteins, antibodies, and cells.

2. An aptamer with high purity can be obtained, and chemical modification is easy to functionalize the terminal group of the aptamer.

3. An aptamer maintains its activity under conditions where the antibody denatured.

4. An activity of aptamer regenerated easily by annealing after being denatured.

These advantages of aptamer can be applied to biosensors by converting structural changes, which induced by binding with target material into sensing signals.

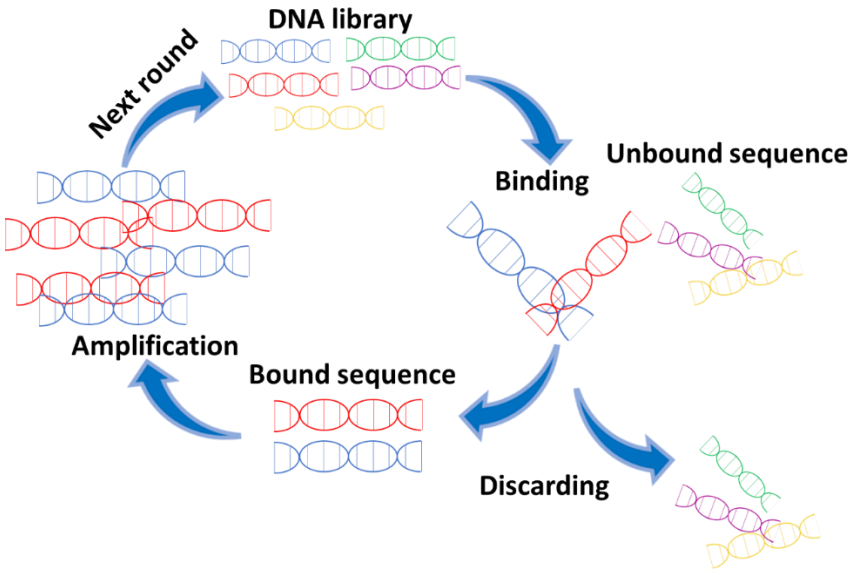

Fig. 1-3 Systematic evolution of ligand by exponential enrichment (SELEX) for screening specific DNA aptamer to bind with target material.

1.4.3. Enzyme

An enzyme catalyzes most chemical reactions in human body. Substrate associates with enzymes and induces a structural change. Specific amino acid side chains in the active site contribute to the specificity of the enzyme. For example, the amino acid with a negatively charged side chains interacts with the positively charged sites of the substrate. The side chains with hydrogen bond group interact with the hydrogen group of the substance. In 1894, Fischer [1-21] proposed a lock and key model to explain the specificity of enzymes for substrate. In this model, the substrate matches the active site of the enzyme so that the key matches the keyhole. In 1958, Koshland [1-22] proposed an induced-fit model for enzyme-substrate binding. In this model, the shape of active site is not entirely complementary to the substrate shape until the substrate bound to the enzyme. The binding of the substrate releases high energy to induces a structural change in the enzyme, which results in a tighter binding between the substrate and the enzyme active site. According to these models, the substrate binds to specific sites on the surface of the enzyme molecule and forms enzyme-substrate complex at a high energy state. The enzyme forms a product by its enzyme reaction and the product is released from the enzyme-substrate complex. Finally, the enzyme returns to its original molecular state and has an affinity with the next substance. In general, the active site conformation closely matches a specific substrate. Therefore, the enzyme is a molecule that can recognize the three-dimensional structure of the substrate.

1.5 Transducer

When the detection element captures some target analyte, an observer is difficult to perceive its chemical reaction and intermolecular interaction. Therefore, the chemical or biological reaction must be extracted as other information. A transducer is a part of electric element that converts changes in chemical/biological reaction into other information, basically electrical signal [1-14, 1-23]. Since the transducer dominates sensitivity, reproducibility, and stability in the biosensor, it is preferred to select suitable transducer for enabling quantitative conversion [1-14, 1-23]. The quantitative measurement of target analyte makes a user to identify not only the presence but also amount of the analyte in a tested sample. Therefore, this feature of transducer makes the biosensor enabling to cover the wide range of analysis application.

Several biosensing technologies with excellent transducers have been reported by using fluorescence resonance energy transfer (FRET) [1-24], paper immunochromatography [1-25], scanning probe or atomic force microscopy (SPM or AFM) [1-26], thermistor [1-27], laser terahertz emission microscope [1-28], electrochemical measurement [1-29], insulated-gate field-effect transistor (ISFET) [1-30] and quartz crystal microbalance (QCM) [1-31], and surface plasmon resonance (SPR) [1-32]. This thesis describes about electrochemical measurement, SPR, and QCM as representative transducers of biosensor.

Recently, affinity-type biosensors using intermolecular interaction have been reported due to easily selection of target biomarkers. Table 1-1 shows a comparison of typical transducers to detect intermolecular interaction. Electrochemical measurement is

a highly sensitive analysis method detecting changes in current or potential derived from some chemical reaction that occurred near an electrode. The measurement system can be miniaturized by a micro-fabrication technology and we can fabricate several small electrodes on a substrate. Therefore, an electrochemical biosensor can achieve multiple detections for several target analytes. However, it is difficult for the sensor to improve the signal against the concentration of analyte. Because the signal-noise ratio is significantly reduced in a microelectrode since signal intensity depends on the size of the electrode. Another disadvantage of electrochemical measurement is not fit to time-dependent monitoring. SPR is one of the highly sensitive and quantitative measurements for intermolecular interactions in real-time without labeling. The principle of measurement is based on the detection of changes in optical properties, especially dielectric constant, generated from the intermolecular interaction over a gold film on a sensor. One of the disadvantages is the limit of detection in-depth direction due to the sensing principle. Thus, it is difficult for SPR to recognize an analyte far away from the gold film. QCM is also unlabeled and real-time measurement that detects quantitatively mass change by intermolecular interaction on a quartz substrate with gold electrodes. The QCM-based sensor can measure several chemical/biological phenomena in a wide-range detection region from the quartz surface. The robust configuration allows other materials to coat on the electrode. In addition, the cost of the device is the cheapest among transducers as shown in Table 1-1. However, the sensor has a low sensitivity for detection of low-molecular-weight materials due to their sensing principle.

In the next section, sensing principles of these transducer are introduced.

Table 1-1 Comparison of representative transducers for intermolecular interaction

	QCM	SPR	Electrochemical measurement
Labeling	No	No	No
Sensitivity	1 ng	1 pg	1 fg
Detecting principle	Mass	Dielectric constant	Current or potential
Time-dependent monitor	Easy	Easy	Difficult
Cost	Inexpensive	Very expensive	Expensive

1.5.1 Electrochemical measurement

Electrochemical measurement is a method evaluating the electrochemical reaction occurring in an electrolysis cell when power supplier applied the various electric signal into the measurement system. The signal responses depend on the concentration and type of chemical substances included in the electrolyte solution. Especially, the current value toward the applied potential can reveal various phenomena at the electrode interface [1-33]. The electrochemical measurement system consists of three electrodes with a potentio/galvanostat. A conductive solid material such as platinum, gold, or carbon is used for counter electrode. Ag/AgCl is mainly selected for the reference electrode. A potential is applied between the reference electrode and the working electrode. The working electrode supplies or accepts electrons to exchange them with oxidant and reductant, as shown in Fig. 1-4. In general, the redox reaction proceeds according to the following reaction formula.

$$\boldsymbol{Oxidant + ne^{-} \rightleftarrows Reductant} \quad (1)$$

Here, e^- is electron. n is number of electrons. This electrochemical reaction takes

place at the electrode/electrolyte interface. The system detects the current flowing between the counter electrode and the working electrode.

The measurement can be broadly divided into amperometry and potentiometry. Amperometry is based on the proportional relationship between the concentration of redox-active species near the electrode surface and the current value during the reaction. A biosensor using an electron transfer by a diffusing substance was reported as an "enzyme electrode" in 1965 [1-34]. The biosensor with this principle is still used as the glucose meter. The electron generated from the enzyme reaction is transferred to the electrode via the mediators.

Potentiometry measures ion concentration dependent on the change in potential between the reference and working electrodes. In the case of a biosensor using lipase as a molecular recognition element, lipases catalyze the reaction of hydrolyzing lipids to generate fatty acids and glycerin [1-35]. The enzyme reaction generates hydrogen ions, which change in the hydrogen ion concentration and cause a potential change on the surface of the working electrode. Therefore, the lipid concentration is measured by detecting the potential change.

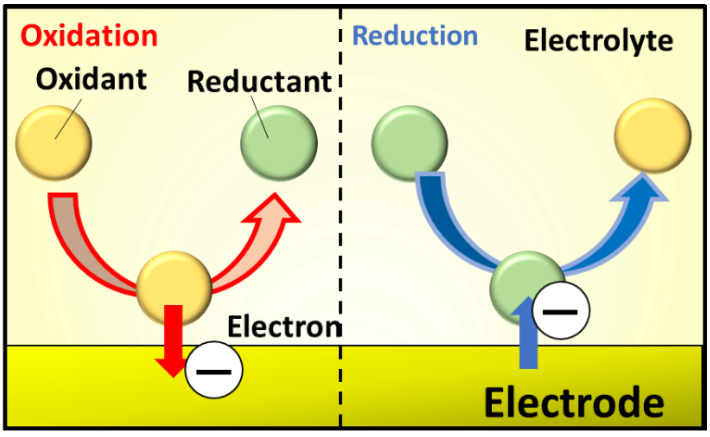

Fig. 1-4 Redox reactions on an electrode to exchange electron with oxidant and reductant.

1.5.2 Surface plasmon resonance (SPR)

Surface plasmon is a resonant state in which electromagnetic waves coupled collective vibrations of free charge on a solid surface [1-36]. The phase velocity of electromagnetic waves and plasmons should be matched to excite surface plasmon with electromagnetic waves. When electromagnetic wave irradiates into an interface having different refractive index, total reflection occurs at a certain incident angle of the irradiated wave (resonant angle) [1-37]. At this time, a specific electromagnetic wave, called evanescent wave, exudes in the media with a small refractive index. This evanescent wave matches the phase velocities of the surface plasmons. Therefore, the evanescent wave is used to excite the surface plasmon resonance (SPR) by the total reflection of the electromagnetic wave on the interface.

Surface plasmons can be excited by irradiating a laser into a device through a prism [1-39], as shown in Fig. 1-5. The evanescent wave is decayed with increasing the distance from the metal surf8ce, while the wave propagates along with the horizontal axis. Surface plasmon resonance condition responds sensitively to changes in dielectric constant of the metal surface. Therefore, when the target analyte absorbed on the metal surface, dielectric constant of the metal surface changes. Finally, the resonant angle shifts toward high wavelength slightly, called red shifts. SPR monitors the association and the dissociation of target analyte near the metal surface [1-39]. When the refractive index changes, the angle of total reflection, and reflectance intensity are proportional to the mass of the bound material. However, the evanescent waves decay exponentially with distance from the interface. SPR can monitor the interaction of molecular near the gold surface. The analyte farther away from the detection region affects insignificantly the

measurement. It is necessary to devise the configuration of SPR to evaluate conformational change of large molecule. In addition, there is a problem which some fluorescence can be disappeared near the metal surface exciting SPR.

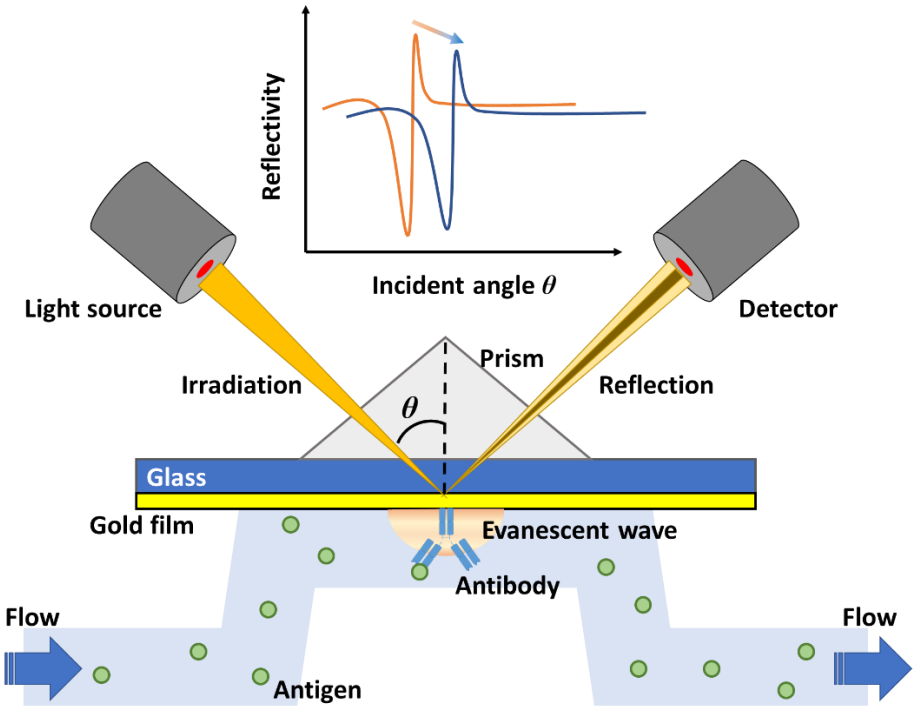

Fig. 1-5 Schematic and configuration of SPR biosensor with a prism and a flow path.

1.5.3 Quartz crystal microbalance (QCM)

A sensor using the quartz crystal microbalance (QCM) method has a simple component and sensing principle. It can be used as a very sensitive microbalance with a low manufacturing cost. Quartz has various characteristics, depending on how to cut them out. Fig. 1-6 shows the quartz crystal with several cutting axes [1-40]. For example, quartz plates cut perpendicular to the x-axis or the y-axis are called a X-cut and a Y-cut, respectively. A quartz plate cut at -45 ° from the z-axis is called a BT-cut. Although these cut axes change the resonance frequency under the influence of temperature, some

examples are used as temperature sensors and hydrogen sensors by utilizing their characteristics. On the other hand, AT-cut quartz crystal, which is cut at 35 ° 15 ' from the z-axis, is used as a sensor substrate because of its low temperature-dependence of oscillation near the room temperature.

The QCM-based sensor consists of the AT-cut quartz with two electrodes on both surfaces. When an AC voltage is applied to both electrodes, shear vibration occurs at a constant frequency in the direction parallel to the crystal plate surface. Because the crystal plate has piezoelectricity, which polarized and distorted in the quartz when applying alternating voltage.

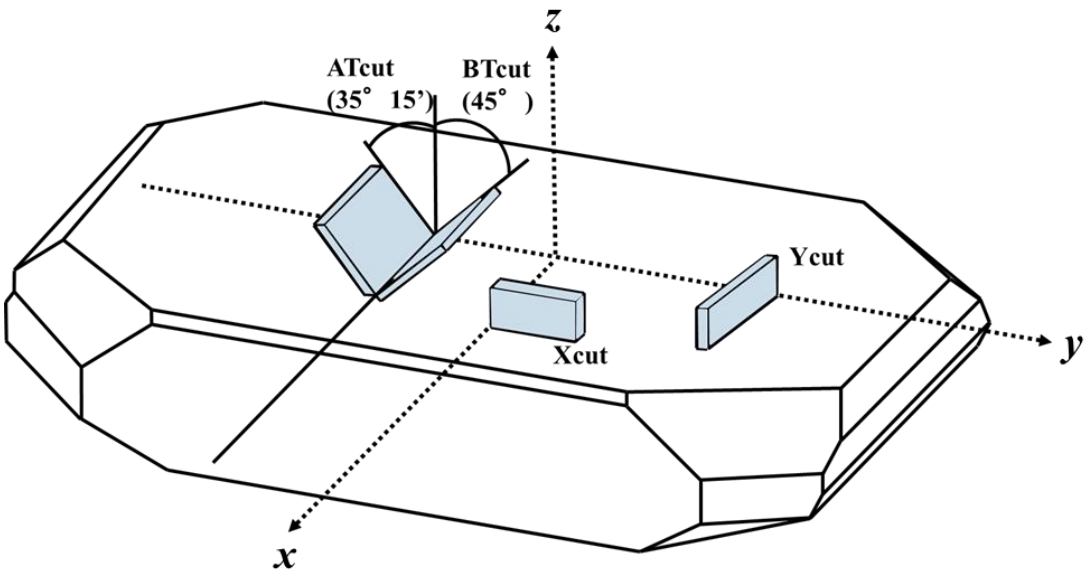

Fig. 1-6 Schematic image of a quartz crystal with several cutting axes.

The QCM-based sensor measures the mass change of the electrode surface corresponding to the substance attachment which lead the change in the resonance frequency of the quartz crystal as shown in Fig. 1-7. Sauerbrey [1-41] reported in 1959 that the frequency shift is proportional to the mass of adsorbed substance on a metal thin film electrode of a quartz plate as a following equation.

$$\Delta F = -\frac{2{F_0}^2}{A\sqrt{\rho_q \mu_q}}\Delta m \tag{4}$$

where, ΔF is the crystal frequency change (unit: Hz), F_0 is the fundamental frequency of crystal (unit: Hz). A is the area of the metal thin film electrode attached to the crystal plate (cm^2). μ_q (2.947×10^{11} g/cm · s^2) is the elastic modulus of the crystal. ρ_q (2.648 g/cm · s^2) is the density of the crystal. Δm is the mass of the substance adsorbed on the electrode.

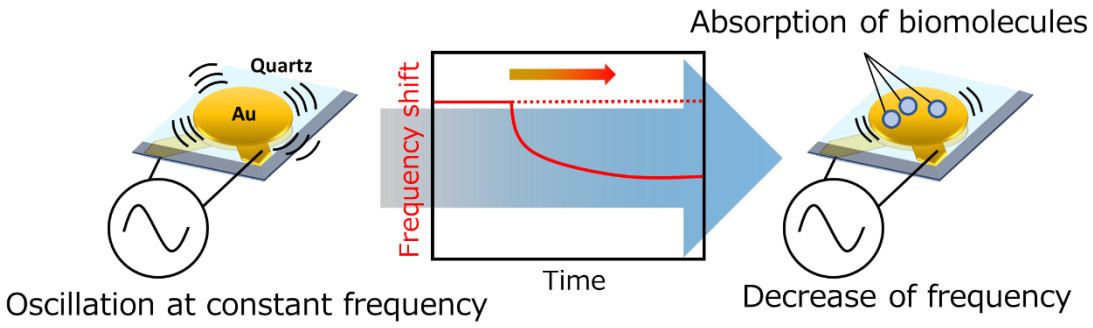

Fig. 1-7 Sensing principle of QCM-based sensor to detect mass change by absorption of target biomolecules.

By observing the vibration of the quartz crystal, energy dissipation factor D can be calculated from the attenuation of the vibration. Furthermore, the viscoelasticity of the

material can be evaluated by using the dissipation factor *D*. A specific QCM method, which enables evaluate the dissipation, is called QCM-dissipation (QCM-D).

There are two oscillation methods for crystal oscillators: the oscillation method and the impedance method [1-42, 1-43]. The oscillation method using the feedback amplifier circuit oscillates the quartz crystal constantly by amplifying a wave of a specific frequency. The frequency has propagated the crystal oscillator and outputted it to the oscillator again. However, in the liquid phase with high viscous resistance, energy loss in the oscillation induces the difference between the input and output to the vibrator, and the feedback amplifier circuit does not work.

On the other hand, the impedance oscillation is a method applying alternative current with several frequencies into both electrode on the quartz [1-43]. The method allows oscillating the quartz in the liquid phase with large viscous resistance. Mass change and viscoelasticity change are correlated between the mathematical equivalence of the mechanical model of QCM and the electrical circuit model of LCR.

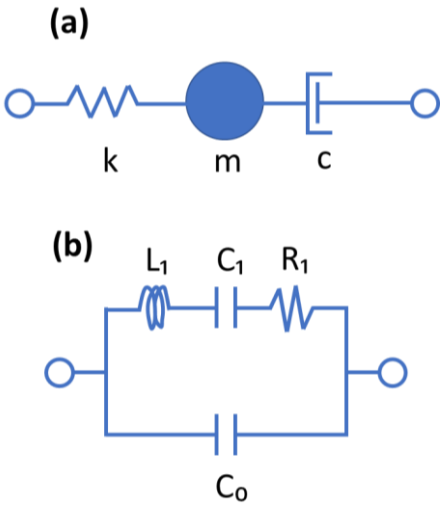

Fig. 1-8 Relationship between mechanical vibration model of QCM device (a) and electrical equivalent circuit of it (b).

The mechanical model is shown in Fig. 1-8 (a). The vibration equation is expressed as follows.

$$\boldsymbol{m\frac{d^2x}{dt^2}+c\frac{dx}{dt}+Kx=F(t)} \tag{5}$$

where, *x* shows the position, the weight is *m*, the friction coefficient is *c*, and the spring constant is *K*.

The electrical equivalent circuit of the quartz crystal is shown in Fig. 1-8 (b). The electrical vibration for L_1, C_1, R_1 is expressed as follows.

$$\boldsymbol{L_1\frac{d^2q}{dt^2}+R_1\frac{dq}{dt}+\frac{1}{C_1}q=V(t)} \tag{6}$$

where q is the charge, and V (t) is the applied voltage.

The electrical equivalent circuit model and the mechanical model can be matched by using the electro-mechanical conversion coefficient *k*. The electro-mechanical conversion coefficient is the efficiency of converting electrical energy applied between the electrodes of a piezoelectric material into mechanical energy. The conversion is presented as $F(t) = kV(t)$, providing the following relationship.

$$\boldsymbol{L_1=\frac{m}{k^2}} \tag{7}$$

$$\boldsymbol{\frac{1}{C_1}=\frac{K}{k^2}} \tag{8}$$

$$\boldsymbol{R_1=\frac{r}{k^2}} \tag{9}$$

Therefore, this analysis method provides the changes in the mass and viscoelasticity of the substance, and also analyze probably the structural change of the

substance in more detail. R_1, L_1, and C_1 correspond to the energy loss of vibration energy, the mass of the crystal unit, and the elasticity of the vibrator.

Admittance analysis produces resonance frequency F, conductance G_{max} at that frequency, and susceptance B, respectively. Fig. 1-9 (a) shows an admittance with real component G and that with imaginary component B against the measurement frequency. The maximum value of G is defined as G_{max}, and the frequency indicating the G_{max}, is defined as the resonance frequency f_s. Fig. 1-9 (b) shows a graph plotting G and B, and f_1 and f_2 to calculate the electrical equivalent circuit constant. The following equation expresses the admittance of the equivalent circuit.

$$\boldsymbol{Y = G + jB = \frac{1}{R_1 + j2\pi f L_1 + 1/j2\pi f C_1} + j2\pi f C_0} \quad (\mathbf{10})$$

$$\boldsymbol{G = \frac{R}{{R_1}^2 + \left(2\pi f L_1 - {1}/{2\pi f C_1}\right)^2}} \quad (11)$$

$$\boldsymbol{B - 2\pi f C_0 = \frac{-(2\pi f L_1 - 1/2\pi f C_1)}{{R_1}^2 + (2\pi f L_1 - 1/2\pi f C_1)^2}} \quad (\mathbf{22})$$

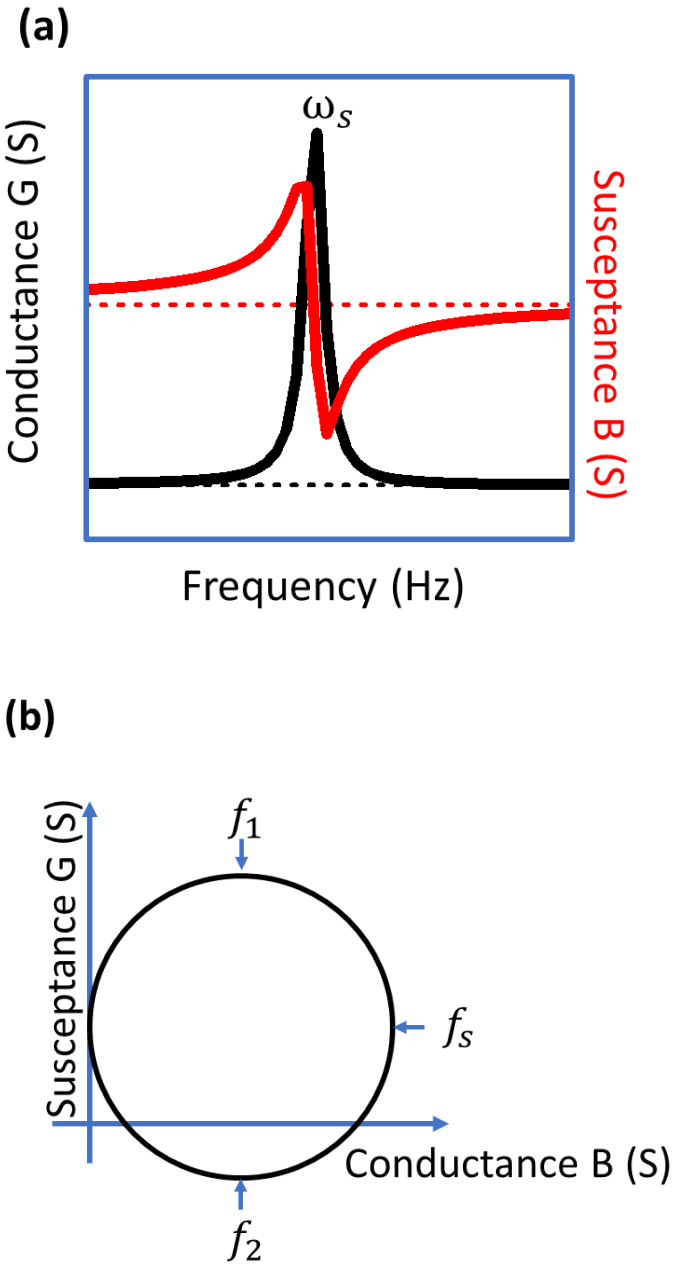

Fig. 1-9 (a) Conductance and susceptance spectrum dependent with frequency. (b) Admittance circle calculated from the results of (a).

1.6 Evaluation of sensing performance

The relationship between the chemical substance and an electrical signal is limited to the range that can be measured by the sensor device, as shown in Figure 1-10. The detection limit indicates the minimum signal that can detect chemical substance at some concentration. In general, the signal-to-noise ratio employs about 3, when the detection limit is calculated. In contrast, output signals from the sensor device sometime shows slight change even if the concentration of target analyte is high. In this case, the sensing system sometime reaches a saturation state of the signal, which is over the detectable concentration based on the sensing principle. The detectable concentration range is called a dynamic range. A device with a lower detection limit and a larger dynamic range can be called higher performance on the sensing device. As shown in Fig. 1-10, a measurement time after reaction and detection of the substance is called the response time of the device.

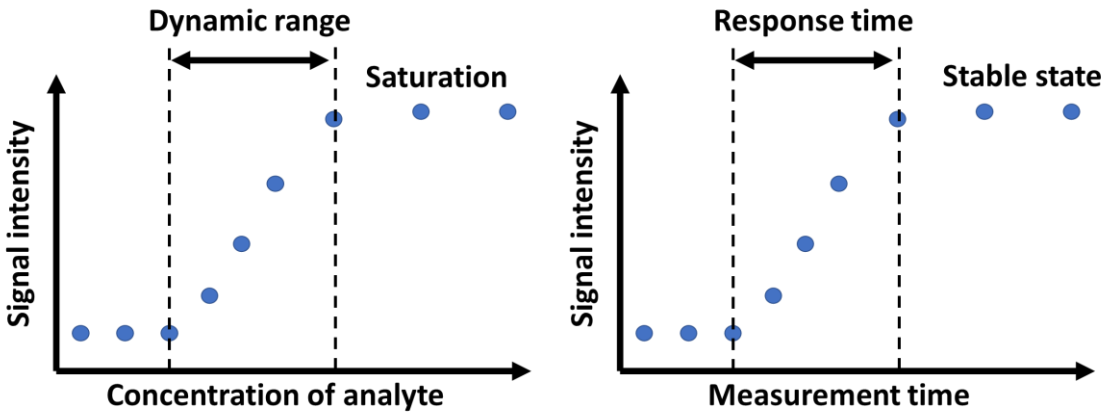

Fig. 1-10 Signal intensity dependent on concentration of substance (left) and time-dependence of a device measuring absorption of target analyte (right).

A detection limit is defined as the minimum amount of an analyte that could be detected as a chemical reaction or an electrical signal of the device. In general, the standard deviation *S* defined below is most commonly used to estimate the degree of variation (amplitude average) of values during repeated measurements.

$$\boldsymbol{S = \sqrt{\frac{\sum_{x=1}^{i}(x_i - \bar{x})^2}{n-1}}} \qquad \textbf{(13)}$$

Here, $\bar{x}$ is an average value for *n* measurement values x_i. The standard deviation is the square root of the unbiased mean square deviation (unbiased variance) divided by *n-1*. A group of data with a sufficient population is represented symmetrically by a mathematical model. The average of the data is populated as a vertex, as shown in Fig. 1-11. The model called a normal distribution or Gaussian distribution. About 68% of the population exists within ± 1*s* from the average. Similarly, about 95% exists within ± 2*s* from the average, and about 99.7% is within ± 3*s* from the average. The detection limit is defined as the minimum amount (average value +3*s*) that detects no analyte in the blank signal distribution with precision with 99.7%. Therefore, the detection limit is considered the lowest amount or concentration that gives a "significantly different" signal from the blank. A concentration corresponding to a value 2 × 1.645*s* = 3.29*s* (= 3*s*) from the average of the blank values is often used as the detection limit concentration.

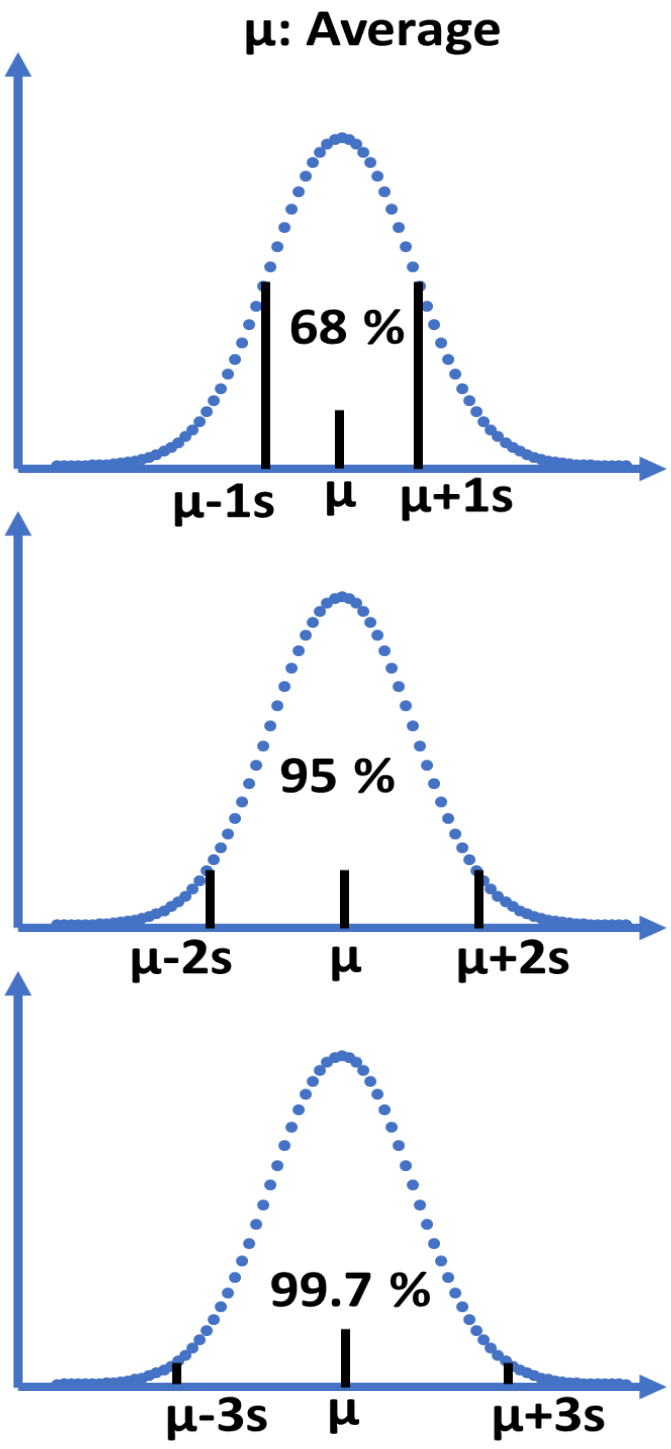

Fig. 1-11 Gaussian distribution and the definition.

1.7 Characteristics of a sensor employing nanostructure

Biosensors are used in various fields such as medical, food engineering, and the environment with a small and inexpensive device. In addition, the target analyte expands to accommodate demands from the market. Therefore, the demands of biosensors are increasing now. Research and development targeting new molecular recognition elements have progressed by integration with microfabrication technology [1-44]. Therefore, the expansion of the detection target will demand further measurement accuracy, dynamic range, sample amount, and measurement time.

Nanostructure has been attracted by the new industrial revolution in information technology [1-45], biotechnology environment [1-46], and energy harvest [1-47]. Because it has many unique advantages such as good electrical conductivity, high surface/volume ratio, and specific optical property. Therefore, the nanostructure has been used for the biosensing application to improve the sensing performance. Localized surface plasmon resonance (LSPR) [1-48] is one of the most famous biosensing application of nanostructure. A nanoparticle is used to excite surface plasmon resonance by localizing electromagnetic field in the nanostructure. The localized surface plasmon matches and absorbs wavelength of irradiated light. An absorbed wavelength depends on the shape of the nanostructure and refractive index based on the dielectric constant surrounding the nanostructure. Therefore, the LSPR can detect target analyte attaching to the surface of the nanostructure [1-48]. In addition, the localization of electromagnetic field in nanostructure has produced a platform of surface enhanced Raman scattering (SERS) for a single molecular imaging [1-49].

The methods of fabricating nanostructure are identified as the dry and wet process [1-50]. Many nanostructures have been fabricated by both top-down and bottom-down

method such as lithography and deposition system of thin-film. The lithography is used to transfer a source pattern to a resist layer on a substrate, then we fabricate the desired structure by etching unnecessary parts. Physical and chemical vapor deposition has manufactured thin-film by deposition of atoms or molecules on the substrate. On the reactive ion etching method, a sample is etched by ions produced from gases in plasma. A combination of these technologies allows to fabricate the nanostructure. The advantages of top-down technology are proceeded miniaturization and high integration of semiconductor. However, a device incorporating with quantum effect requires further miniaturization and higher integration [1-51]. Lithography technology is challenging to meet the requirements by their features such ultra-fine processing, low throughput, cost, and small processing area.

The self-organized nanostructures have drawn attention as a new perspective of microfabrication technology due to a large area production and precise fabrication at a lower cost [1-52]. Lithography technology can not reach to form a structure of the same scale due to the limit of resolution.

1.7.1 Self-assembled monolayer (SAM)

Self-assembled monolayer (SAM) has been actively used to functionalize a surface of a material in recent years because of their ease of preparation and versatility. The SAM compose of two functional groups, one reacts with metal atoms and the other make an intermolecular force. These characteristics allow us to form high-density thin films with nano-scale [1-54].

The formation process of SAM is schematically described in Fig. 1-12 [1-53]. The

substrate is immersed in the solution which target molecules are solved. The target molecules react with metal atoms on the substrate and then bond on the surface chemically. According to the binding process, the bond molecules are aggregated closely and stabilized thermodynamically. When the mono-molecular film is assembled, the adsorption reaction stops because of covering the surface with molecules without any infilling. These features have contributed to develop a study of the biosensor on the immobilization of the recognition elements using a terminal group on the electrode surface.

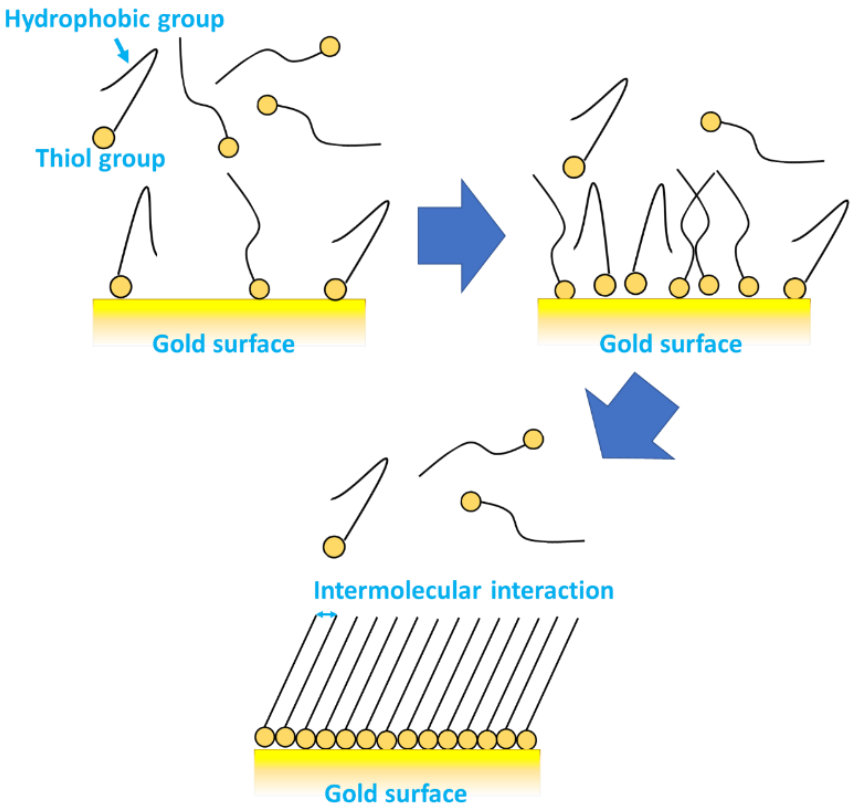

Fig. 1-12 Schematic image of SAM formation process.

1.7.2 Plating

Plating method is one of the most important methods to fabricate the wiring and electrode. By combination of the plating with the other techniques such as a mask or a mold, the plating method can supply the metal-based nanostructure on the substrate. The plating method can be classified into two ways, with or without an electric power source, as shown in Fig. 1-13. The plating with power source is called electroplating. The plating without power source is called electroless-plating.

In the electroplating, the base electrode is connected to a power source, and an electric current is supplied to induce a metal reduction on the surface of the base electrode. Metal ions in the electrolyte receive the electron from the base electrode, and then it is reduced on the surface [1-54]. On the other hand, in the electroless-plating, the metal ion is reduced by a chemical reaction which is occurred using a reducing agent in the solution [1-55]. This metal reduction reaction proceeds only on the surface which is catalyzed by noble metal catalysts such as palladium and platinum. Due to necessity of pretreatment for the substrate in electroless-plating, the electroplating has an advantage that forms thin films of various metal types in a short time. The electroless-plating can form a metal film with a precisely controlled film thickness. In contrast, there are different characteristics of the substrate for the electroplating and the electroless-plating. It needs conducive bulk materials on the electroplating because a thin metal film is reduced and deposited by electrons supplied from a power source. On the other hands, it needs not a power supply to reduce the metal ion on the electroless-plating. Therefore, insulating materials such as plastics and ceramics are available to be metalized on the electroless-plating.

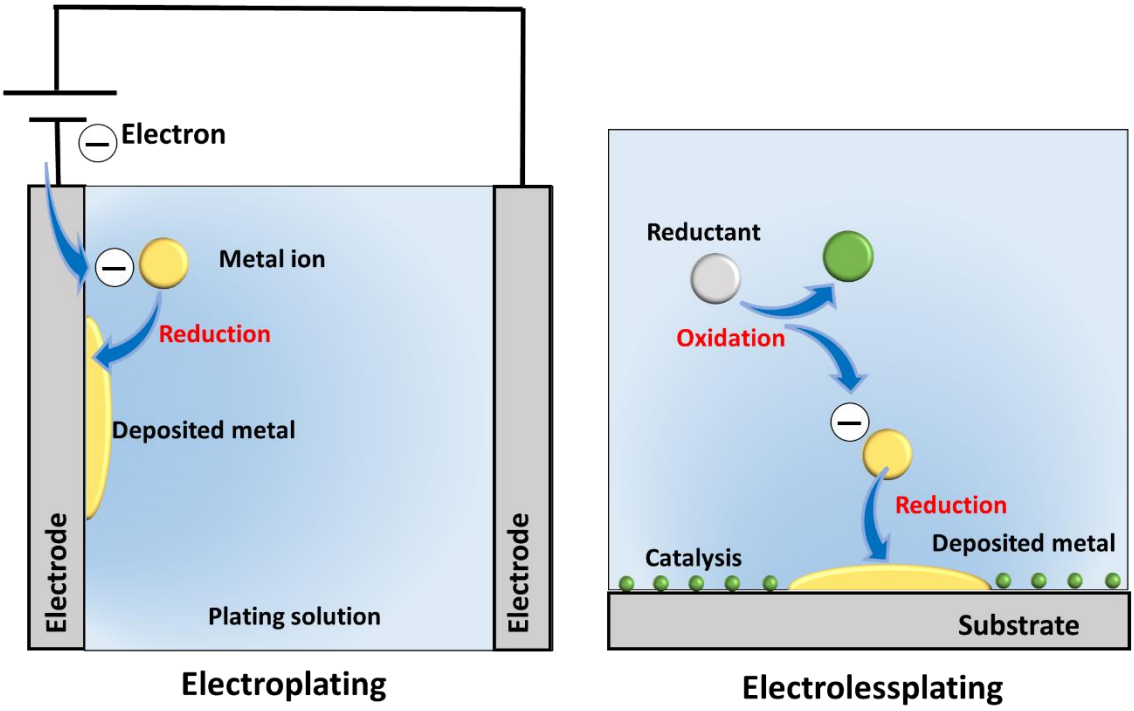

Fig. 1-14 Principles of electroplating and electroless-plating.

1.7.3 Colloidal lithography

As a process using self-organization, the aggregation of molecules by the weak interaction forms a stable molecular-level-ordered structure. By spreading a dispersion liquid containing regularly particles on a solid substrate, the particles form a close-packed structure in a self-organized manner due to surface tension during the volatilization of the solvent (Fig. 1-14). This technology is called as colloidal lithography, which provide us controlled gaps between close-packed particles [1-56]. The polystyrene particles are formed on a solid substrate, which provides a mask with two-dimensional colloidal crystal. Position-selective electroless-plating of capper supplies a honeycomb-like metal pattern along with the gap on the substrate. A similar antidot pattern can be obtained by sputtering a metal film on the substrate instead of electroless-plating [1-57]. The diameter of

polystyrene bead is controlled by oxygen plasma etching because it is composed of organic materials.

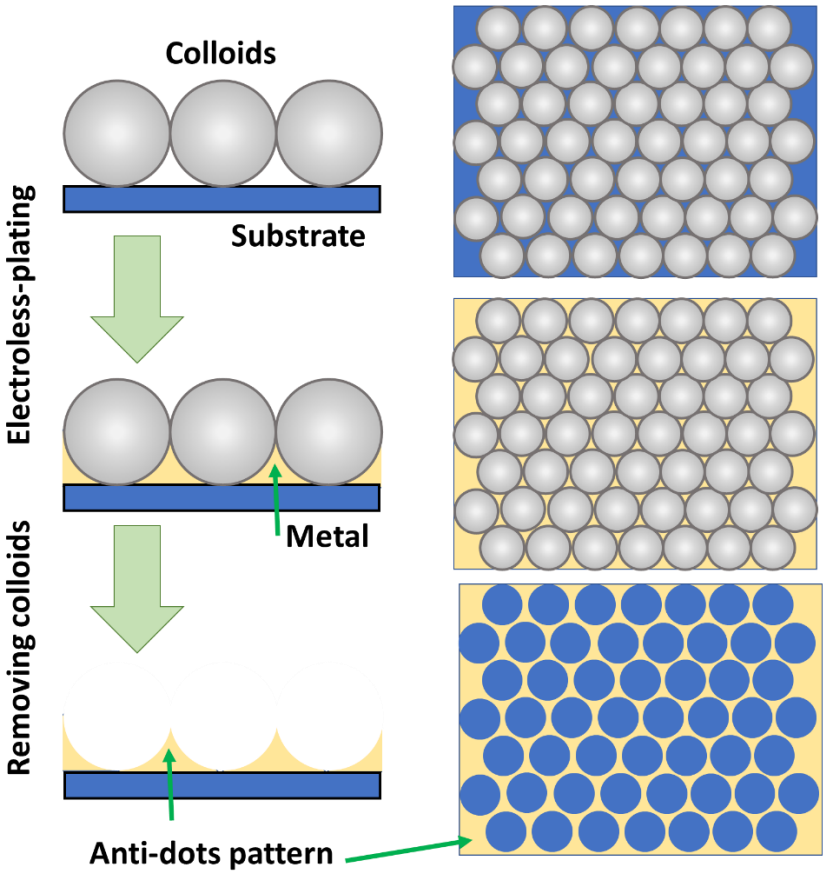

Fig. 1-14 Colloidal lithography with electroless-plating to fabricate anti-dots pattern.

1.7.4 Anodization

Anodization is one of surface treatments forming an oxide film on the metal surface by electrochemical etching. For examples, metals of aluminum, magnesium, and titanium are able to be anodized. Nowadays, anodized aluminum is widely used and is called anodized aluminum oxide (AAO). As shown in Fig. 1-15, AAO has a regularly-arranged porous film obtained by anodizing aluminum. In addition, AAO shows many unique characteristics such as friction resistance, insulation, transparency or translucency

[1-57]. The pore diameter, pitch, and thickness can be controlled by changing the electrolyte solution, applied voltage, and applied time, respectively. On the anodization in acidic solutions less than pH =5, the oxide film is dissolved locally and formed nanoholes with a high aspect ratio [1-57]. In the initial stage of anodization, the surface roughness of aluminum influences the nanohole formation. Therefore, the AAO nanohole diameter and cell size are irregular in the initial stage. However, all nanoholes are regularly arranged in a triangular lattice with equal intervals, according to the growth of nanoholes and stress acting in the in-plane direction. In recent years, templates with regular nanostructures can be easily produced at low cost by using AAO nanoholes instead of electron beam lithography technology that is the expensive and has complicated vacuum equipment [1-58].

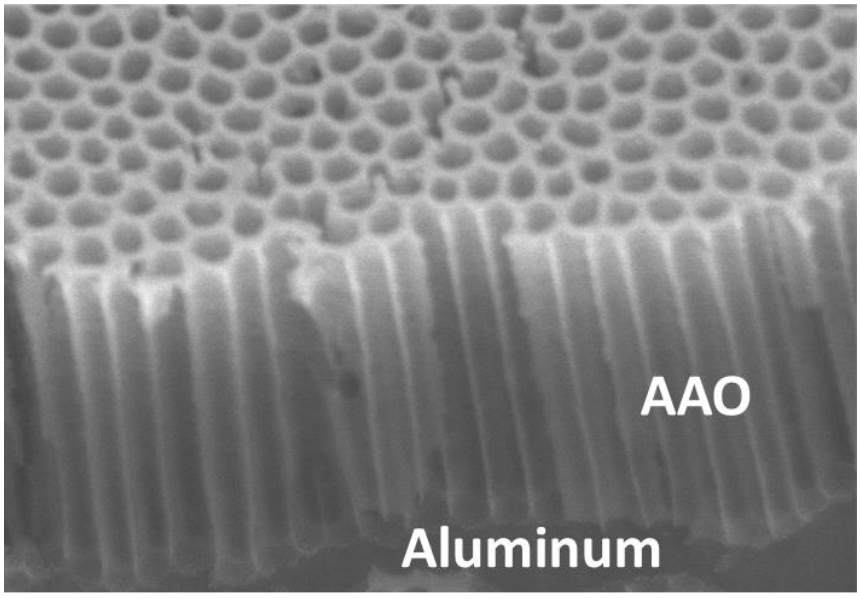

Fig. 1-15 Bird-view scanning electron microscopy (SEM) image of AAO with vertically grown nanoholes.

1.8 Assembly of organic nanostructure using deoxyribonucleic acid (DNA)

Recently, the recognizing function of DNA has drawn attentions of scientists to form self-assembled nanostructure [1-59]. DNA has excellent properties, such as molecular assembly by its base sequence and periodicity of double helix structure. The principle of creating planar 2D DNA nanostructures was proposed in 1982 by Seeman et al. [1-60]. A holiday junction consisted of double-stranded DNA structures that branched in four directions (Fig. 1-16). In the structure, four single-stranded DNA strands are combined each other using complementary base pairs to create a two-dimensional sheet-like structure. This unit is assembled with other units by combination of the terminal of each double-stranded structure. Finally, the numerous units are combined to create a micrometer-sized 2D DNA nanostructure.

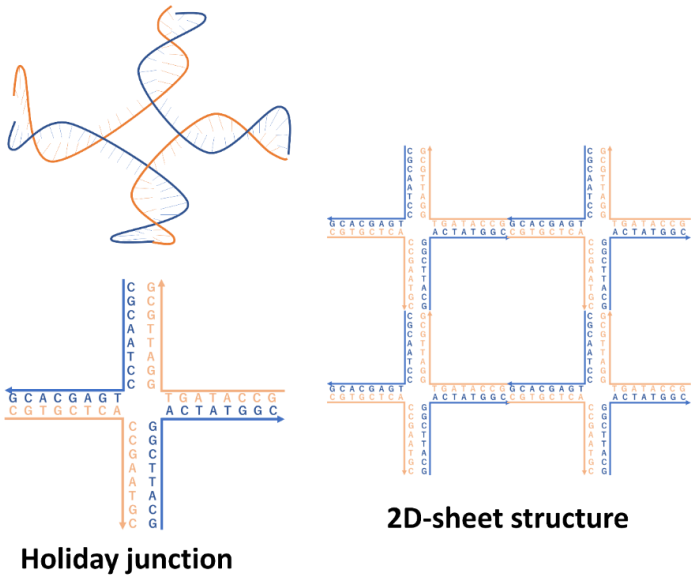

Fig. 1-16 Schematic image of creation of 2D-sheet structure based on holiday junctions.

DNA origami is an application of assembling system in 2D DNA nanostructure. In 2006, Rothmund developed an assembling method of DNA origami corresponding to arbitrary design with 100 nm scale. DNA origami consists of one long single-stranded DNA (7,249 bases in M13mp18) and numerous complementary-strand DNA (called staple strand in 32-mer). By mixing and annealing all of them in solution, a planar structure is formed by self-assembly (Fig. 1-17). During annealing process, each staple strand hybridized complementarily to the specified sequence of long single-stranded DNA. Finally, the long single-stranded DNA is folded into a 2D structure as designed in advance. In the folded planar structure, double-stranded DNAs are aligned in parallel, and the respective staple strands are cross-linked to connect adjacent double-stranded DNAs. The distance of each cross-linkage is 32 base pairs equivalent to 3 turns of the helix. The cross-linked parts of staple strands are faced on the horizontal direction to maintain a planar structure. The periodicity of staple strands in the design maintains the planar structures of DNA origami. Realigning the ends of the structure allows to design complex 2D structures such as triangles, stars, and smile marks [1-61]. In addition, three-dimensional DNA structures can be formed if the adjacent double-stranded DNA structures are bridged at 120 ° and 240 ° and bonded horizontally in a wavy state [1-62]. Since different staple strands are bound to each position of the DNA origami structure, hairpin DNA) or single-stranded DNA can be replaced at any position.

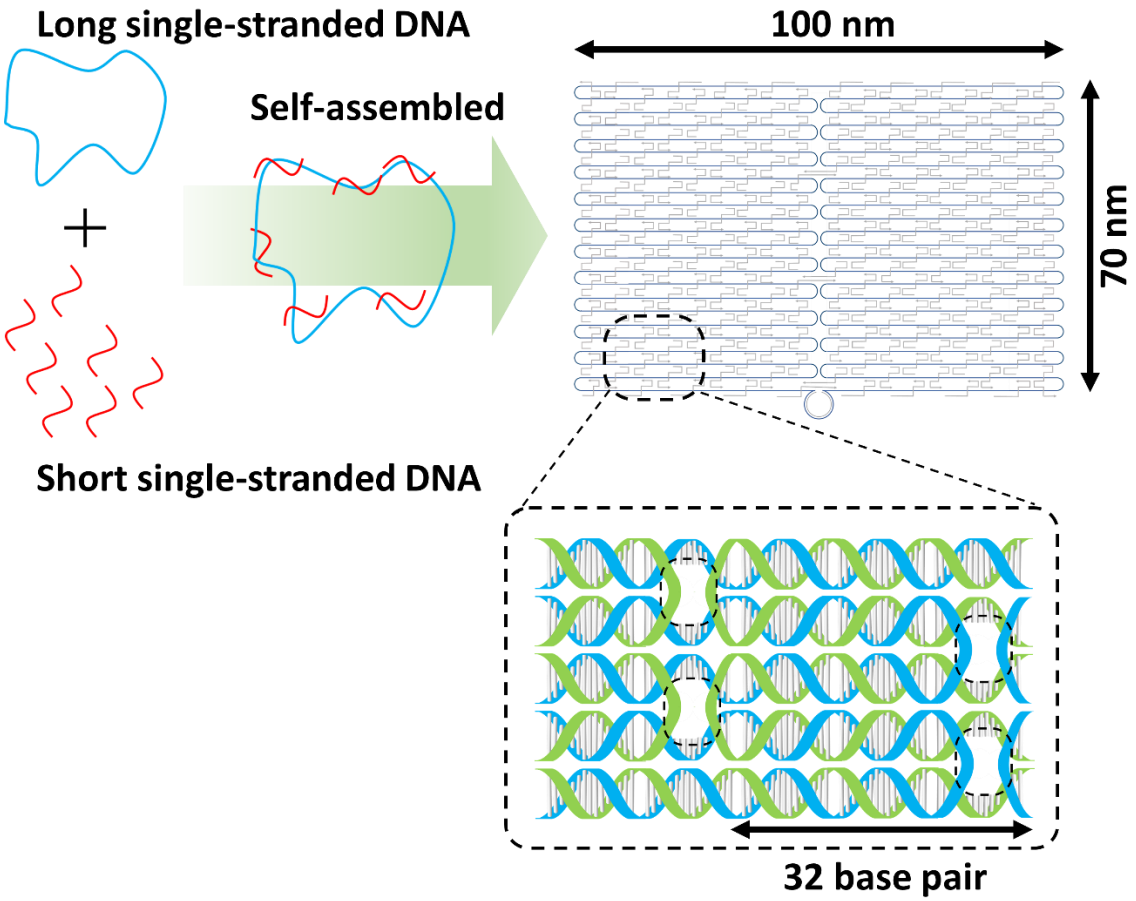

Fig. 1-17 Schematic image of an assembled DNA origami and its enlarged view.

1.9 Outline of this thesis and objective

As mentioned in section 1.2, a novel early detection method for a cancer might be achieved by a screening using *C. elegans*. However, the use of *C. elegans* at home is impossible due to difficult management of culturing environment, and so on. A biosensor, which consists of biorecognition element and transducer, is good approach to understand mechanism of some phenomena in tissue, cell, and organ. The sensing interfaces should be arrayed to capture accurately many information from the complicated phenomena. Semiconductor microfabrication techniques contribute various biosensors to be miniaturized. However, it is difficult to reduce the size of the apparatus maintaining the sensing performance, such as sensitivity. The sensing signals is weakened because the signal intensity depends on the surface area of the electrode, especially for the electrochemical measurement and QCM measurement. As one approach to improve the sensitivity, nanostructures with large surface area were fabricated on the electrode surface of the biosensors [1-63]. Dry process technology is a good approach to fabricate well-controlled nanostructure. However, it is difficult to fabricate nanostructures on the extensive substrate which are in millimeter-or micrometer-scale due to low throughput [1-64].

Furthermore, nanostructure allows to fabricate a unique biosensing device which integrated two or more technologies into one sensing platform [1-65]. The conventional sensing technologies had detected one parameter change induced by biochemical phenomena. Scientists have to detect the isolated phenomena by the divided measurement systems when they investigate two or more reactions. Recently, a combined plasmonic/QCM-based sensor has been presented to understand biochemical phenomena in detail, such as protein-protein interaction [1-66], and structural change of lipid vesicle

[1-67]. The combined plasmonic/QCM-based sensor is fabricated by electron beam or colloid lithography. However, it is difficult to fabricate a regularly ordered nanostructure at a large surface area more than centimeter scale.

In this thesis, inorganic or organic nanostructures, which were fabricated by wet-process, formed on the electrode surface of the QCM-based sensor to immobilize a large quantity of recognition elements. On the measurement of biomolecules interaction by QCM-based sensor, the mass change of the absorbed molecules was monitored without any unexpected chemical reaction such as ions concentration change. According to the measurement principle of QCM, the oscillation from quartz can propagate to the nanostructure. Therefore, a nanostructured QCM-based sensor detects the absorption of biomaterial sensitively due to expanded sensing region. The mass changes would reveal an actual contribution of nanostructure on the biosensing. Additionally, the mechanical stability of the nanostructure is also important for the biosensing application. The flow injection system should be integrated with the biosensing technology to improve throughput and reduce sample volume. Attachment of a flow path on the biosensor would increase viscous friction between the electrode surface and the liquid path. Therefore, the mechanical property of nanostructures was also evaluated by investigation of its viscoelasticity.

In chapter 2, anodizing of the gold electrode produced the sponge-like gold nano-porous structure on the electrode surface of the QCM-based sensor. The anodization condition was adjusted to form several gold nano-porous structures. The effective surface area was evaluated by electrochemical measurement. In the QCM measurement, antigen-antibody interaction was detected by QCM-based sensors with a gold nano-porous or flat surface electrode. The mass changes obtained by both sensors were compared to evaluate

the sensing performance. After the measurement, the gold porous nanostructure was observed by scanning electron microscopy and atomic force microscopy to evaluate the morphology.

In chapter 3, the gold dendrite structure was formed on the gold electrode by electroplating. Polyethylene glycol (PEG) concentration in the solution and applied voltage were controlled to promote the branching structure. The effective surface area of the dendric gold electrode was evaluated by electrochemical measurement. Resonant resistance of the sensor was measured by electrical admittance analysis to evaluate resonance properties in the liquid phase. In the QCM measurement, antigen-antibody interaction was detected by QCM-based sensors with a dendric or flat surface electrode. The mass changes obtained by both sensors were compared to evaluate the sensing performance.

In chapter 4, an anodic aluminum oxide nanohole array was produced on the quartz substrate by anodizing of aluminum film. Several fabrication conditions with post-etching allowed to control the diameter and the depth of nanohole. Electrical admittance analyzed the resonant properties of the nanostructured QCM-based sensor in the liquid phase. In addition, the dimension of nanohole was optimized on the QCM measurement of antigen-antibody interaction. The sensing performance of the AAO-nanostructured QCM-based sensor was compared with the conventional QCM-based sensor on the concentration-dependent frequency shift. The AAO-nanostructured QCM-based sensor was also used for the detection of PPIs, which was Bcl-2 and Bax interaction.

In chapter 5, aptamer-attached DNA origami was assembled on the gold electrode of the QCM-based sensor. The assembling method was optimized to obtain well-form

DNA origami. The number of aptamers embedded with DNA origami ranged from 0 to 166. Several aptamer-attached DNA origamis showed an aptamer-dependent frequency shift due to aptamer-protein interaction. The sensing performance of DNA origami coated sensors were compared with that of the conventional sensor.

1.9 References

1-1	International Agency for Research on Cancer, World Cancer Report 2014, 2014.
1-2	International Diabetes Federation, IDF DIABETES ATLAS Seven Edition 2015, 2015
1-3	Tackling Drug-Resistant Infections Globally: final report and recommendations 2016
1-4	R. Dorfman, Modifier gene studies to identify new therapeutic targets in cystic fibrosis. Curr. Pharm. Des., 2012 18, 674-682.
1-5	S. L. Bøe, J. A. Jørgensen, A. S. Longva, T. Lavelle, S. Sæbøe-Larssen, and E. Hovig, Light-controlled modulation of gene expression using polyamidoamine formulations. Nucleic Acid Ther., 2013 23, 160-165.
1-6	J. K. Patra, G. Das, L. F. Fraceto, E. V. R. Campos, M. del P. Rodriguez-Torres, L. S. Acosta-Torres, L. A. Diaz-Torres, R. Grillo, M. K. Swamy, S. Habtemariam and H.-S. Shin, Nano based drug delivery systems: recent developments and future prospects. J. Nanobiotechnol., 2018 16:71.
1-7	N. Banaei N, A. Foley, J. M. Houghton, Y. Sun, and B. Kim, Multiplex detection of pancreatic cancer biomarkers using a SERS-based immunoassay. Nanotechnol., 2017 28:455101.
1-8	J.-C. Lagier, S. Edouard, I. Pagnier, O. Mediannikov, M. Drancourt, and D. Raoult, Current and Past Strategies for Bacterial Culture in Clinical Microbiology. Clin. Microbiol. Rev., 2015 28, 208–236.
1-9	V. V. Demidov, Rolling-circle amplification in DNA diagnostics: the power of simplicity. Expert Rev. Mol. Diagn., 2002 2, 542-548.
1-10	T. Hirotsu, H. Sonoda, T. Uozumi, Y. Shinden, K. Mimori, Y. Maehara, N. Ueda, and M. Hamakawa, A Highly Accurate Inclusive Cancer Screening Test Using Caenorhabditis elegans Scent Detection. PLOS ONE, 2015 10, e0118699.
1-11	H. M. Robertson, and J. H. Thomas, The putative chemoreceptor families of C. elegans. Worm Book, 2006.

1-12	R. Takahashi, H. Miyazaki, and F. Takeshita, Loss of microRNA-27b contributes to breast cancer stem cell generation by activating ENPP1. Nat. Commun. 2015 6, 7318.
1-13	D. Huh, B. D. Matthews, A. Mammoto, M. Montoya-Zavala, H. Y. Hsin, and D. E. Ingber, Reconstituting organ-level lung functions on a chip. Science, 2010 328, 1662–1668.
1-14	N. Bhalla, P. Jolly, N. Formisano, and P. Estrela, Introduction to biosensors. Essays Biochem., 2016 60, 1–8.
1-15	S. Sharma, H. Byrne, and R. J. O'Kennedy, Antibodies and antibody-derived analytical biosensors. Essays Biochem., 2016 60, 9–18.
1-16	Z. Junhui, C. Hong, and Y. Ruifu, DNA based biosensors. Biotechnol. Adv., 15, 1997 15, 43-58.
1-17	H. H. Nguyen, S. H. Lee, U. J. Lee, C. D. Fermin, and M. Kim, Immobilized Enzymes in Biosensor Applications. Materials., 2019 12, 121.
1-18	H. W Schroeder Jr, and L. Cavacini, Structure and Function of Immunoglobulins. J. Allergy. Clin. Immunol., 2010 125, S41–S52.
1-19	A. D. Ellington, J. W. Szostak, In vitro selection of RNA molecules that bind specific ligands. Nature., 1990 346, 818-822.
1-20	C. Tuerk, and L. Gold, Systematic evolution of ligands by exponential enrichment: RNA ligands to bacteriophage T4 DNA polymerase. Science., 1990 249, 505-510.
1-21	E. Fischer, Einfluss der Configuration auf die Wirkung der Enzyme. Ber. Dt. Chem. Ges., 1894 27, 2985-2993.
1-22	D. E. Koshland, Application of a Theory of Enzyme Specificity to Protein Synthesis. Proc. Natl. Acad. Sci. U. S. A., 1958 44, 98-104.
1-23	P. Mehrotra, Biosensors and their applications – A review, J. Oral. Biol. Craniofac. Res., 2016 6, 153–159.
1-24	N. N. Aye-Han, N. Qiang, and J. Zhang, Fluorescent biosensors for real-time tracking of post-translational modification dynamics. Curr Opin Chem Biol., 2009 13, 392–397.
1-25	B. B. Dzantiev, N. A. Byzova, A. E. Urusov, and A. V. Zherdev, Immunochromatographic methods in food analysis. TrAC Trends in Analytical Chemistry., 2014 55, 81-93.
1-26	A. M. Moulin, S. J. O'Shea, and M. E. Welland, Microcantilever-based biosensors, Ultramicroscopy, 2000 82, 1, 23-31.
1-27	M. Yakovleva, S. Bhand, and B. Danielsson, The enzyme thermistor—A realistic biosensor concept. A critical review. Analytica Chimica Acta, 2013 5, 1-12.

1-28	T. Kiwa, A.Tenma, S. Takahashi, K. Sakai, and K. Tsukada, Label free immune assay using terahertz chemical microscope. Sens. Actuat. B-Chem., 2013 187, 8-11.
1-29	A. Ramanavicius, A. Finkelsteinas, H. Cesiulis, and A. Ramanaviciene, Electrochemical impedance spectroscopy of polypyrrole based electrochemical immunosensor. Biochemi. US, 2010 79, 11-16
1-30	F. Bettaiebaf, L. Ponsonnetb, P. Lejeunec, H. B. Ouadad, C. Marteleta, A. Bakhroufe, N. Jaffrézic-Renaulta, and A. Othmane, Immobilization of E. coli bacteria in three-dimensional matrices for ISFET biosensor design. Bioelectrochemistry. 2007 71, 118-125.
1-31	N. E. Weckman, C. McRae, P. K. Ferrigno, A. Seshia, Comparison of the specificity and affinity of surface immobilised Affimer binders using the quartz crystal microbalance. Analyst., 2016 141, 6278-6286.
1-32	J. F. Masson, Surface Plasmon Resonance Clinical Biosensors for Medical Diagnostics. ACS Sens., 2017 2, 16-30.
1-33	D. Grieshaber, R. MacKenzie, J. Vörös, and E. Reimhult, Electrochemical Biosensors - Sensor Principles and Architectures. Sens., 2008 8, 1400–1458.
1-34	L.C. Clark Jr, C. Lyons, and N. Y. Ann, Electrode systems for continuous monitoring in cardiovascular surgery. Acad. Sci., 1962 102, 29-45.
1-35	M. Pohanka, Biosensors and Bioassays Based on Lipases, Principles and Applications, a Review. Mol., 2019 24, 616-630.
1-36	N.A. Krall, and A.W. Trivelpiece, Principles of Plasma Physics (McGraw-Hill Inc., 1973).
1-37	A. Otto, Excitation of nonradiative surface plasma waves in silver by the method of frustrated total reflection. Z. Phys., 1968 216, 398-410.
1-38	E. Kretschmann, The determination of the optical constants of metals by excitation of surface plasmons. Z. Phys., 1971 241, 313-324.
1-39	M. Piliarik, H. Vaisocherová, and J. Homola, Surface plasmon resonance biosensing. Methods. Mol. Biol., 2009 503, 65-88.
1-40	C. J. Chen, A. Schwarz, R. Wiesendanger, O. Horn, and J. Müller, Three-electrode self-actuating self-sensing quartz cantilever: design, analysis, and experimental verification. Rev Sci Instrum., 2010 81:053702
1-41	G. H. Sauerbrey, Verwendung von Schwingquarzen zur Wägung dünner Schichten und zur Mikrowägung. Z. Phys., 1959 155, 206–222.
1-42	M. Rodahl, and H. Kasemo, A simple setup to simultaneously measure the resonant frequency and the absolute dissipation factor of a quartz crystal microbalance. Rev. Sci. Instrum., 1998 67, 3238–3241.

1-43	L. Daikhin, E. Gileadi, G. Katz, V. Tsionsky, M. Urbakh, and D. Zagidulin, Influence of Roughness on the Admittance of the Quartz Crystal Microbalance Immersed in Liquids. Anal. Chem., 2002 74, 554-561.
1-44	G. Luka, A. Ahmadi, H. Najjaran, E. Alocilja, M. DeRosa, K. Wolthers, A. Malki, H. Aziz, A. Althani, and M. Hoorfar, Microfluidics Integrated Biosensors: A Leading Technology towards Lab-on-a-Chip and Sensing Applications. Sens., 2015 15, 30011–30031.
1-45	H. J. Krenner, C. E. Pryor, J. He, and P. M. Petroff, A Semiconductor Exciton Memory Cell Based on a Single Quantum Nanostructure. Nano Lett., 2008 8, 1750-1755.
1-46	J. L. West, and N. Jhalas, Applications of nanotechnology to biotechnology. Curr. Opin. Biotech., 2000 11, 215-217.
1-47	G. Liu, T. Chen, J. Xu, and K. Wang, Blue energy harvesting on nanostructured carbon materials. J. Mater. Chem. A, 2018 6, 18357-18377.
1-48	B. Sepúlveda, P. C. Angelomé, L. M. Lechuga, L. M.Liz-Marzán, LSPR-based nanobiosensors. Nano Today, 2009 4, 244-251.
1-49	K. E. Shafer-Peltier, C. L. Haynes, M. R. Glucksberg, R. P. Van Duyne, Toward a Glucose Biosensor Based on Surface-Enhanced Raman Scattering. J. Am. Chem. Soc., 2003 125, 588-593.
1-50	H. Ahmed, Nanostructure fabrication. IEEE Proc., 1991 79, 1140-1148.
1-51	I. Berbezier, and M. D. Crescenzi, Self-assembly of nanostructures and nanomaterials. J. Nanotechnol., 2015 6, 1397–1398.
1-52	K. Ariga, M. Nishikawa, T. Mori, J. Takeya, L. K. Shrestha and J. P. Hill, Self-assembly as a key player for materials nanoarchitectonics. Sci. Tech. Adv. Mater., 2019 20, 51-59.
1-53	D. K. Schwartz, MECHANISMS AND KINETICS OF SELF-ASSEMBLED MONOLAYER FORMATION. Annu. Rev. Phys. Chem., 2001 52, 107–137.
1-54	P. C. Andricacos, C. Uzoh, J. O. Dukovic, J. Horkans, H. Deligianni, Damascene copper electroplating for chip interconnections. IBM J. Res. Dev., 1998 42, 567 - 574.
1-55	R. A. WZhou, Electroless nickel-plating on AZ91D magnesium alloy: effect of substrate microstructure and plating parameters. Surf. Coat. Technol., 2004 179, 124-134.
1-56	S.-M. Yang, S. G. Jang, D.-G. Choi, S. Kim, and H. K. Yu, Nanomachining by Colloidal Lithography. Small, 2006 2, 458–475.
1-57	H. Masuda, and K. Fukuda, Ordered metal nanohole arrays made by a 2-step replication of honeycomb structures of anodic alumina. Science, 1995 268, 1466–1468.

1-58	Y. Lei, W. Cai, and G. Wilde, Highly ordered nanostructures with tunable size, shape and properties: A new way to surface nano-patterning using ultra-thin alumina masks. Prog. Mater. Sci., 2007 52, 465-539.
1-59	Y. Sakai, Md. S. Islam, M. Adamiak, S. Chi-Chin Shiu, J. A. Tanner, and J. G. Heddle, DNA Aptamers for the Functionalisation of DNA Origami Nanostructures. Genes 2018, 9(12), 571.
1-60	E. Winfree, F. Liu, L. A. Wenzler, N. C. Seeman, Design and self-assembly of two-dimensional DNA crystals. Nature, 1998, 394, 539
1-61	P. W. K. Rothemund, Folding DNA to create nanoscale shapes and patterns. Nature, 2006, 440, 297-302.
1-62	S. M. Douglas, A. H. Marblestone, S. Teerapittayanon, A. Vazquez, G. M. Church, and W. M. Shih, Rapid prototyping of 3D DNA-origami shapes with caDNAno. Nucleic Acids Res., 2009 37, 5001–5006.
1-63	P. I. Reyes, Z. Zhang, H. Chen, Z. Duan, J. Zhong, G. Saraf, Y. Lu, O. Taratula, E. Galoppini, and N. Boustany, A ZnO Nanostructure-Based Quartz Crystal Microbalance Device for Biochemical Sensing. IEEE SENS. J., 2009 9. 1302-1307.
1-64	Z. Ma, C. Jiang, W. Yuan, and Y. He, Large-scale Patterning of Hydrophobic Silicon Nanostructure Arrays Fabricated by Dual Lithography and Deep Reactive Ion Etching. Nano-Micro Lett., 2013 5, 7-12.
1-65	J. Zhu, S. Huang, J. Ye, X. Zhang, and G. Liu, Design of a quartz crystal with transparent electrode used for both QCM-D and LSPR technology. Sens. Actuat. A-Phys., 2015 229, 141-146.
1-66	D. Hao, C. Hu, J. Grant, A. Glidle, and D. R. S. Cumming, Hybrid localized surface plasmon resonance and quartz crystal microbalance sensor for label free biosensing. Biosens. Bioelectron. 2018 100, 23-27.
1-67	M. P. Jonsson, P. Jonsson, and F. Hook, Simultaneous Nanoplasmonic and Quartz Crystal Microbalance Sensing: Analysis of Biomolecular Conformational Changes and Quantification of the Bound Molecular Mass, Anal. Chem., 2008 80, 7988–7995.

Chapter 2: Anodized Au nano-porous structure to improve a sensitivity on QCM-based sensor

2.1 Brief introduction of Au nano-porous structure

Gold nanoparticles are suitable nanomaterials for biosensing among the noble metal nanoparticles (NPs) due to their biocompatibility, optical properties, electron transport and facile functionalization [2-1, 2-2]. As an example, localized surface plasmon resonance (LSPR) utilized their advantages in biosensing [2-3, 2-4]. The LSPR is excited by the visible light source, and the plasmon field propagates around the gold nanoparticles. The analyte can be detected by the changes in dielectric constant around the nanoparticle. The change in dielectric constant is converted to refractive index change. Looking to the electrochemical measurements, it often utilizes the gold nanoparticle as a catalyst for sensitive detection of redox enzyme and target ligand interaction. Gold nanoparticles can support the transference of electrons between electroactive species and electrodes [2-5, 2-6].

Synthesis technique is important to obtain the specific properties of gold nanoparticles and control the arbitrary shape or size. The tuned dimensions resulted in different optical, catalytic, and electronic properties of the gold nanoparticles. One of the most common methods of Au NP synthesis is the addition of $HAuCl_4$ into boiling trisodium citrate. In this method, the citric acid solution promoted the thermal reduction of $HAuCl_4$ and nucleation of gold particles [2-7]. Several ratios of the citric acid solution and $HAuCl_4$ synthesized a well-dispersed Au NP with diameters ranging from 4 nm to 20 nm. Besides, the Au NP size can be controlled by changing the ratio, temperature, and

reagent addition rate.

Masuda et al. reported a more convenient method of producing gold nanoparticles, which diameter was 20 nm, by anodization of gold thin films in electrolytes such as H_2SO_4, $COOH_2$ and NaOH solutions [2-8]. The technique provided ~~a~~ pure gold NPs with aggregated structure like a sponge. The size of gold nanoparticle was controllable by changing the applied potential. A dealloying from Au-Sn alloy is other method to obtain the sponge-like Au nanostructure. However, the reproduction of dealloying is difficult due to requirement of a strict synthesizing condition such as Au-Sn ratio [2-9]. The properties of anodized nanoparticles are excellent advantages that can be easily applied to biosensing, catalyst, and plasmonic research areas. In biosensing studies, this sponge-like Au nanostructure was used to detect dopamine and p-nitrophenol [2-10, 2-11].

In this chapter, the sponge-like Au nanostructure was obtained on the electrode of a QCM (quartz crystal microbalance)-based sensor by anodizing its electrode in an oxalic acid solution. Au nanostructures were anodized with several fabricating conditions such as the applied potential and anodization time. The effective surface areas of obtained nanostructure were evaluated by electrochemical measurements, scanning electron microscopy (SEM), and atomic force microscopy (AFM). Various anodization conditions allowed several Au nanostructures with different shapes. QCM-based sensors with anodized electrodes were used to measure an antigen-antibody reaction. The large surface area of the anodized Au electrode improved detection capability, comparing with the flat surface electrode and sponge-like nano-porous structure.

2.2 Experimental details

All the reagents for fabricating Au nanostructures and electrochemical evaluation were purchased from Wako Pure Chemical Industries Ltd. Anti-mouse IgG and mouse IgG were purchased from Funakoshi Co., Ltd. SiO_2 wafer was taken from Mitorika Glass Co., Ltd.

At first, Au nanostructures were fabricated on a SiO_2 substrate instead of a quartz substrate. Ti (30 nm thick) and Au (100 nm thick) were sputtered on the SiO_2 substrate by using a DC magnetron sputtering equipment in order. Au nanostructures were obtained by anodizing the gold thin film with a Pt plate as a cathode for 1 minute in the oxalic acid solution (0.3 M). The potential on the anodization was set from 2 to 5 V against the Pt plate. After rinsing the SiO_2 substrate with pure water, nanostructures were observed by SEM (JEOL, JSM-7500F). The effective surface area of Au nanostructure was estimated by cyclic voltammetry (CV) with three electrodes system. Each electrode composed of anodized Au working electrode, Pt wire counter electrode, and Ag/AgCl reference electrode, respectively. Here, an electrolyte was sodium sulfate (0.5 M), including potassium ferricyanide (1 mM). Here, the QCM-based sensor with anodized Au electrode is called as an anodized QCM-based sensor.

The anodic condition was optimized to obtain anodized Au nanostructure with the largest surface area. A QCM-based sensor with anodized electrode measured antigen (mouse IgG)-antibody (anti-mouse IgG) interaction to evaluate the sensitivity. In this experiment, a flow injection system was combined with QCM-based sensor. The QCM-based sensor had a fundamental frequency of 9 MHz and composed of a quartz crystal

sandwiched by Au electrodes with a diameter of 5 mm. 300 nm thick Au film was sputtered on the titanium thin film (50 nm), which was worked as an adhesion layer between a quartz substrate and Au film, by DC magnetron sputtering system. In this study, the QCM-based sensor with a flat gold electrode is called Au-thin-film QCM-based sensor. QCM-based sensor connected to a QCM analyzer (SEIKO EG&G, QCM 922A), and located at a constant temperature chamber to keep room temperature. A micro-syringe pump and sample injector connected to a flow cell with PEEK tubes. The QCM-based sensor equipped with a jig made of ABS resin and PDMS. Phosphate buffered saline (PBS, pH=7.4) was used as a carrier solution with a flow rate of 5 μL/min.

Anti-mouse IgG and BSA immobilized onto the electrode, as written below. At first, 20 μl of anti-mouse IgG was dropped on the electrode for 1 hour for immobilization. After washing with PBS, 20 μl of BSA solution (0.05 wt%) was dropped on it for 1 hour for immobilization. After washing with PBS, the flow cell was set on the sensor and inserted in the thermostatic chamber. A QCM analyzer with the sensor monitored the frequency shift after injection of 100 μL of sample solutions including mouse IgG. Finally, we compared the sensitivity of sensors with/without gold nanostructure by frequency shifts corresponding to the antigen-antibody interaction. Besides, the morphology of the QCM-based sensors was evaluated by AFM (SII Inc., SPA 400) with a tapping mode. The measured area was 1 μm^2.

2.3 Characterization of anodized Au nanostructures

Fig. 2-1 shows the cross-sectional SEM images of anodized Au nanostructures fabricated on the SiO_2 substrate. Each sample were anodized at 2, 3, 4, 5 V for 1 min. The anodization with 3, 4, and 5 V formed sponge-like structures with multi-layer of nanoparticles. The thickness of them was approximately 150 nm. On the contrast, anodization with 2 V formed nanosphere with the diameter of 100 nm on the electrode. The sponge-like Au nanostructure had a large surface area to adsorb the biomaterial, such as antigen, antibody, and enzyme. Masuda et al. applied the several potentials to anodize the gold film and they got different sponge-like structures dependent with applied voltage [2-8]. The diameter of their fabricated nanoparticle was smaller than 20 nm, and the glossy black color originated from the highly porous configuration. The exterior colors of Fig. 2-1 (c), (d), and (e) were changed from red to black with longer anodization in this study. The color changes were caused by surface plasmon resonance and random reflection of visible light. These characteristics matched with Masuda's results. Therefore, the sponge-like structure was composed of Au nanoparticles. However, the sphere structure, as shown in Fig. 2-1 (b), did not change colors.

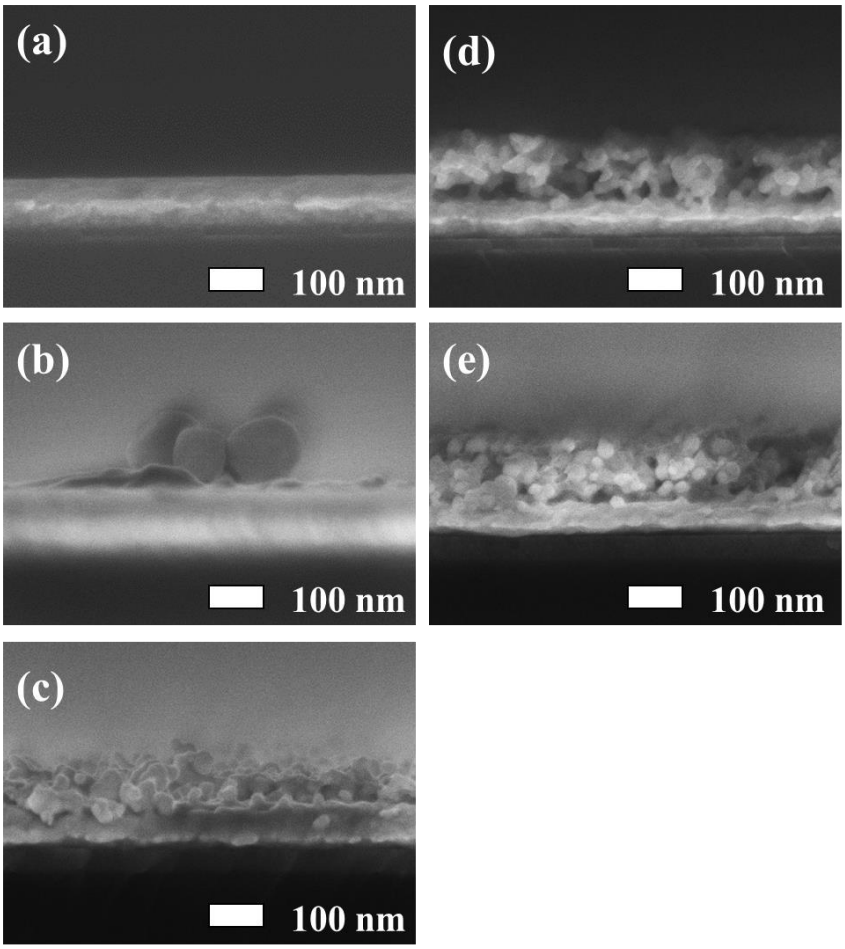

Fig. 2-1. Cross sectional SEM images of Au-thin-film (a) and Au nanostructures obtained by anodization of Au thin film in oxalic acid for 1 minutes (the applied potential of 2 V: b, 3 V: c, 4 V: d, 5 V: e).

Fig. 2-2 shows the schematic images of nanostructure formation at the high and low applied potential. In anodization, the current density might influence on the diameter of the nanoparticle. The superficial Au was oxidized by applying potential, and it formed Au_2O_3 thin layer on the gold. The oxidized Au produced $Au3^+$ and $3e^-$ by electrolyzing. The Au ion reconstructed the gold randomly on the electrode due to its less ion stability.

In addition, bubbles were generated during the anodization and attached on the gold surface. The attachment of bubbles disturbed the electrolyte being contacted to the gold surface. The other surface without bubbles was electrolyzed strongly. Then, the sponge-like nanostructures were formed by the reconstruction and the etch of gold film. The increase of potential promoted to etching the Au structures and decreasing the diameter of nanoparticles.

On the contrast, the milder anodization produced spheres by repeating reconstructed and etched stages as below. First, the surface was oxidized and electrolyzed with the above reasons. After Au^{+3} diffused to the electrolyte, Au reconstructed on the superficial bump. Au_2O_3 was reduced and formed to Au under 2 V of applied potential less than the oxidizing potential of Au. Then, the Au nanosphere formed on the surface. Secondly, the sphere was hardly electrolyzed and oxidized. The current and potential concentrated on the top of the sphere more than gold film or its side surface. The less density of current and potential allowed Au ion to reconstruct on the side surface of the sphere. Therefore, the shape of the nanosphere was nonuniformity (Fig. 2-1 (b)).

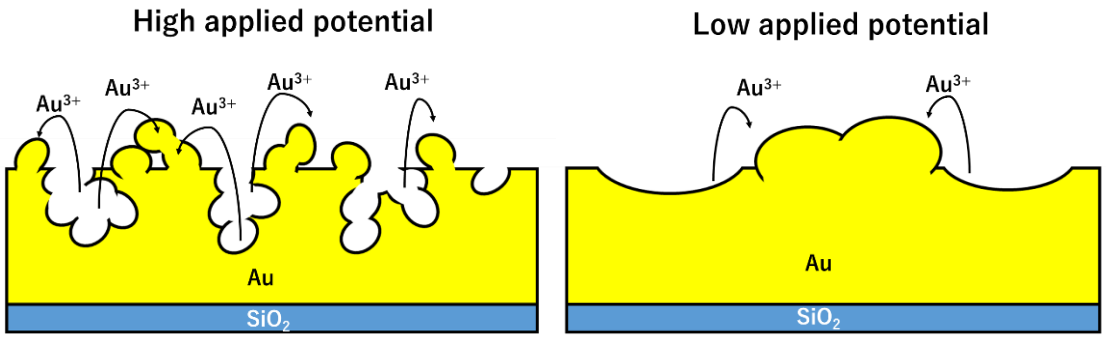

Fig. 2-2. Schematic images of nanostructure formation at high and low applied potential.

2.4 Evaluation of effective surface area by electrochemical measurement

Cyclic voltammetry evaluated the effective surface area by comparing an oxidation peak. The potential range was between 0.1 to 0.5 V vs. the reference electrode, and the sweep rate was 10 mV/s. Here, sample A was a flat gold film without anodization (Au-thin-film). In each anodized Au film, the current values at the oxidation peak increased comparing with that of sample A. This result indicated that an effective surface area enlarged by the anodization. The effective surface was calculated from the oxidation peak current using the following formula [2-12].

$$\boldsymbol{A = \frac{i_p \times 100}{269 \times n \times c \times \sqrt{n \times D \times v}}} \quad (2.1)$$

where, *A*, *ip*, *n*, *c*, *D*, and *v* are the effective surface area (cm^2), oxidation peak current (*A*), reactive electron number (*n*=1, in this study), concentration of potassium ferricyanide (1 mM), diffusion constant of potassium ferricyanide (6×10^{-6} cm^2/s), and the sweep rate (10 mV/s), respectively. Table 1-1 shows the effective surface area calculated using the formula (2.1).

Sample B, which was anodized under the applied potential of 2 V, produced the largest effective surface area. The electrolyte contacted with only the top of the sponge-like structures, decreasing the effective surface area gradually. Therefore, the surface area of nanosphere was larger than that of the sponge-like structures. The high current value indicated the low electrical resistance of the anodized Au nanostructures, and it consisted of pure gold [2-8].

Table 1-1 The oxidation peek current evaluated by cyclic voltammograms (middle column). The effective surface area was calculated by equation (2.1) (right column).

Conditions	Oxidation current value (μA)	Effective surface area (mm^2)
A: Au-thin-film	0.65	9.78
B: 2 V, 1 min	0.74	13.35
C: 3 V, 1 min	0.88	12.36
D: 4 V, 1 min	0.81	11.54
E: 5 V, 1 min	0.76	11.23

2.5 Detection of antigen-antibody interaction by anodized Au nano-porous structure on QCM-based sensor

From the results of CVs, the Au nanosphere structure was selected to improve the sensitivity of QCM sensor. After the Au electrode on the QCM-based sensor was anodized, the anodized QCM-based sensor was used to detect the antigen-antibody reaction. In addition, Au-thin-film QCM-based sensor without anodization was used as a reference. On the antigen injection, a significant frequency shift was observed both on the anodized and Au-thin-film QCM-based sensor, as shown in Fig. 2-3. These frequency shifts were caused by binding of mouse IgG with anti-mouse IgG on the Au electrode. The frequency shifts on the Au-thin-film and anodized QCM-based sensor were 58.4 and 129.9 Hz, respectively. Fig. 2-4 shows the calibration curve of the QCM measurements. Frequency shift of anodized QCM-based sensor (sample B) was twice as that of the Au-thin-film QCM-based sensor. The detection limit was about 0.5 μg/ml.

Fig. 2-5 shows AFM images of the Au-thin-film and anodized surface of QCM-based sensor. Surface roughness (Rz_{jis}) of Au-thin-film and anodized QCM-based sensor were 2.8 nm and 111.3 nm, respectively. Here, Rz_{jis} is a ten-point average roughness (Japanese Industrial Standard, B0601, 2001). AFM observed the diameter of the

nanoparticle as approximately 100 nm, which was a similar diameter analyzed by the SEM, as shown in Fig. 2-1 (b). The surface roughness on the anodized electrode of QCM-based sensor was much larger than that on Au-thin-film QCM-based sensor. Sputtering methods fabricated the smooth Au electrode on the Au-thin-film QCM-based sensor. Other anodized QCM-based sensors C, D, and E did not reach a steady-state in the frequency shift during PBS flowing before antibody injection. Fig. 2-6 shows the surface SEM images of anodized QCM-based sensor with anodizing potential at 3 V before and after flowing PBS. The Au nanostructure dissociated from the Au electrode surface due to its frangible rigidity. The dissociated Au nanostructure resulted in a decrease of the effective surface area.

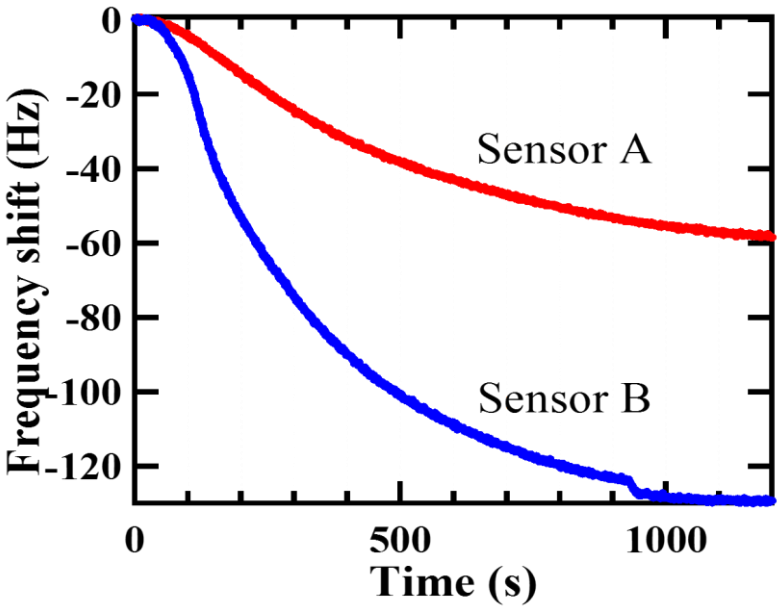

Fig. 2-3 Time dependent frequency shifts of the Au-thin-film QCM-based sensor (A) and anodized QCM-based sensor (B) on antigen-antibody interaction. The flow rate was 5 μL/min. 100 μL of mouse IgG (10 μg/mL) was injected.

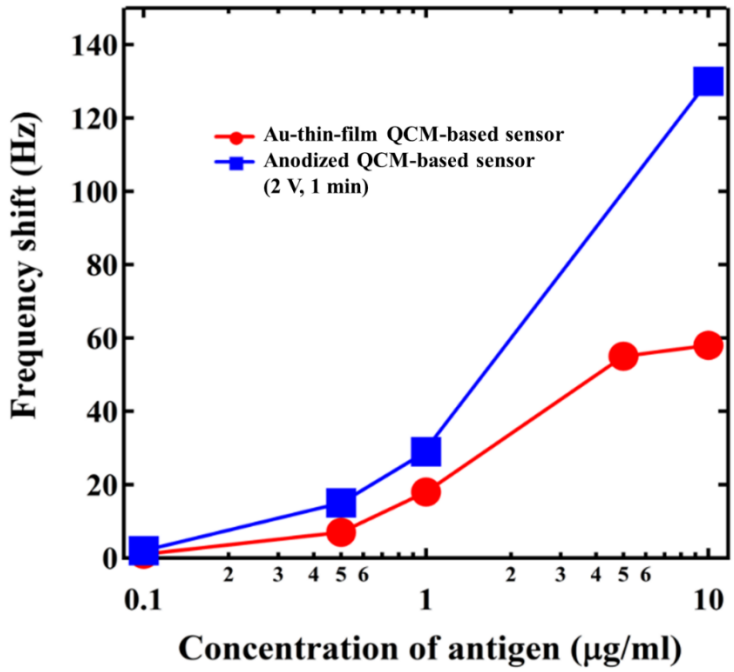

Fig. 2-4. The calibration curves on the detection of mouse IgG. Red circles and blue squares are detected by using anodized QCM-based sensor and Au-thin-film QCM-based sensor, respectively.

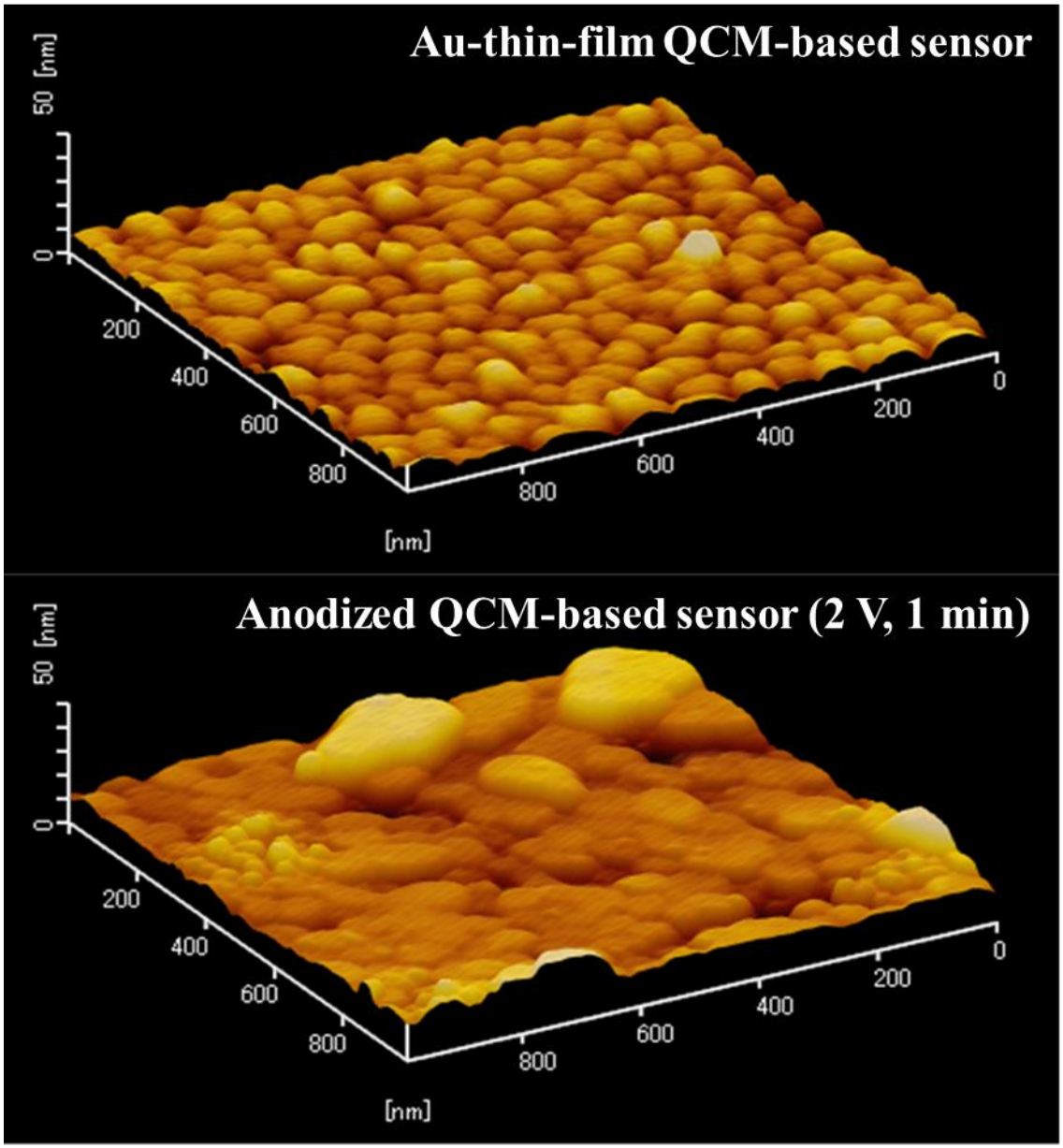

Fig. 2-5. AFM images of the surface of the Au-thin-film and anodized Au QCM-based sensor. The applied potential was 2 V to fabricate the anodized QCM-based sensor. Scan area was 1 μm^2.

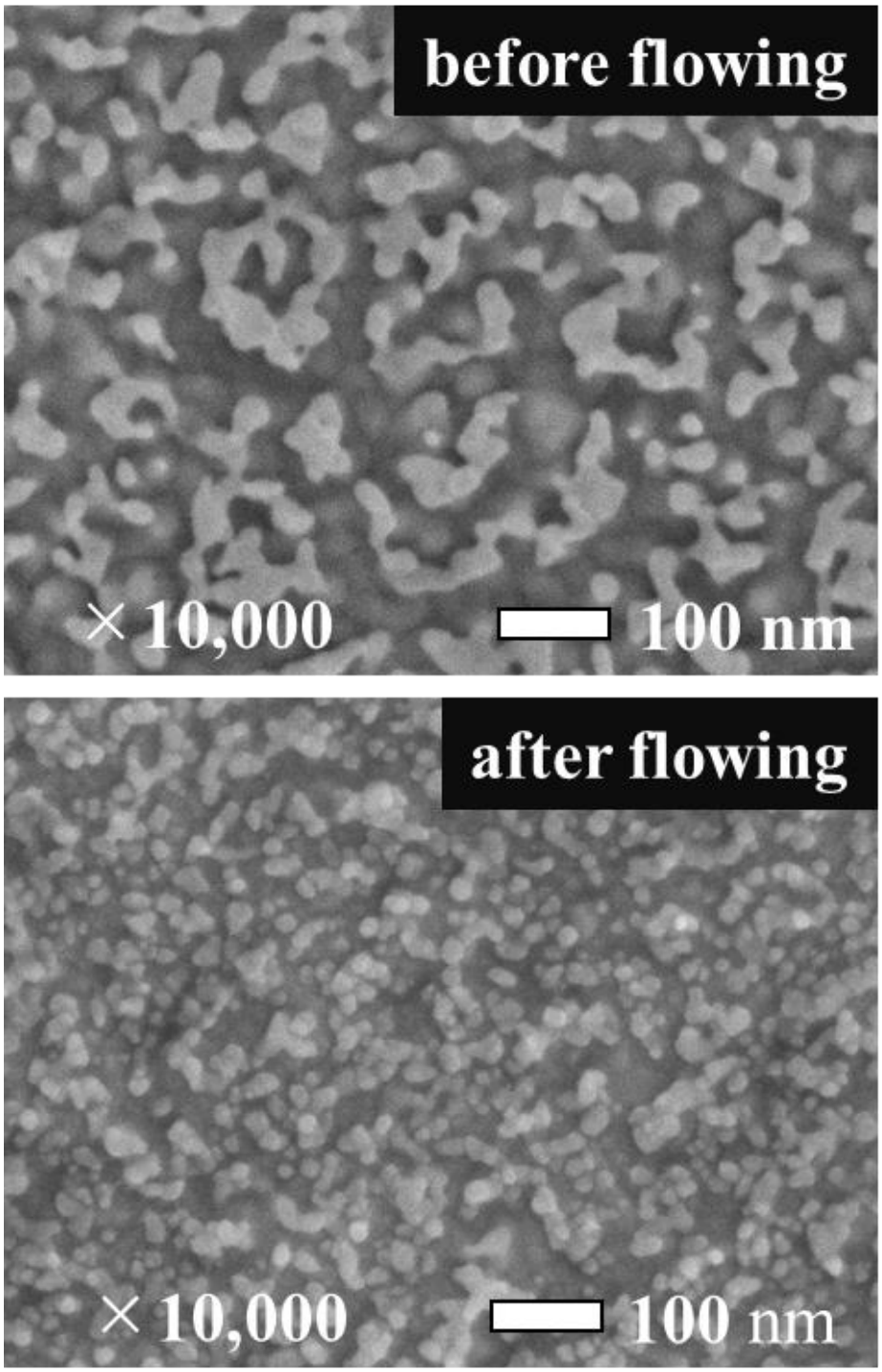

Fig. 2-6. Surface SEM images of the anodized Au on the QCM-based sensor (3 V, 1 min) before (upper) and after (lower) the PBS flowing.

2.6 Conclusions

Anodization of gold film conducted the Au nanostructures on the electrode of the QCM-based sensor. Nanospheres and sponge-like Au nanostructures were formed by anodization with the applied potential of 2 V, and over 3 V, respectively. The effective surface areas of these nanostructures were evaluated by electrochemical measurement, SEM, and AFM. The results indicated that the higher applied potential promoted to originate fragile nanostructures. QCM measurement was performed to evaluate the sensitivity of the anodized QCM-based sensor. A comparison of the frequency shift on antigen-antibody showed that the sensitivity of the anodized Au QCM-based sensor was higher than that of Au-thin-film QCM-based sensor. However, the sponge-like structure on the electrode was dissociated readily by flowing buffer solution. The higher anodizing potential originated the fragile configuration of Au nanostructure.

References

2-1	Y. Li, H. Schluesener, and S. Xu, Goldnanoparticle-based biosensors. Gold Bull., 2010 43, 29–41.
2-2	V. Biju, Chemical modifications and bioconjugate reactions of nanomaterials for sensing, imaging, drug delivery and therapy. Chem. Soc. Rev., 2014 43, 744–764.
2-3	S. Chen, M. Svedendahl, R.P.V. Duyne, and M. Ka´lll, Plasmon-enhanced colorimetric ELISA with single molecule sensitivity. Nano Lett. 2011 11, 1826–1830.
2-4	N. C. Veitch, Horse radish peroxidase: a modern view of a classic enzyme. Phytochemistry, 2004 65, 249–259.
2-5	M.L. Mena, P. Yáñez-Sedeño, and J.M. Pingarrón, A comparison of different strategies for the construction of amperometric enzyme biosensors using gold nanoparticle-modified electrodes. Anal. Biochem., 2005 336, 20–27.
2-6	B. Willner, E. Katz, and I. Willner, Electrical contacting of redox proteins by nano technological means. Curr. Opin. Biotechnol., 2006 17, 589–596.
2-7	J. Turkevich, P.C. Stevenson, and J. Hillier, A Study of the Nucleation and Growth Processes in the Synthesis of Colloidal Gold. Discuss. Faraday Soc., 1951 11, 55-75.
2-8	K. Nishio, and H. Masuda, Anodization of Gold in Oxalate Solution To Form a Nanoporous Black Film. Angew. Chem., Int. Ed., 2011, 50, 1603-1607.
2-9	J. Xu, T. Kou, and Z. Zhang, Anodization strategy to fabricate nanoporous gold for high-sensitivity detection of p-nitrophenol. Cryst. Eng. Comm., 2013, 15, 7856-7862.
2-10	Y. Pei, M. Hu, F. Tu, X. Tang, W. Huang, S. Chen, Z. Li, and Y. Xia, Ultra-rapid fabrication of highly surface-roughened nanoporous gold film from AuSn alloy with improved performance for nonenzymatic glucose sensing. Biosens. and Bioelectron., 2018 117, 758–765.
2-11	A. Kumar, J. S. G. Selva, J. M. Gonçalves, K. Araki, and M. Bertotti, Nanoporous gold-based dopamine sensor with sensitivity boosted by interferant ascorbic acid. Electrochimica. Acta., 2019 322, 134772.
2-12	A. J. Bard, and L. R. Faulkner, ELECTROCHEMICAL METHOD FANDAMENTALS AND APPLICATIONS, (John Wiley & Sons, New Jersey, 2001) p.231.

Chapter 3: Electroplated Au dendrite nanostructure for improvement of a sensitivity on QCM-based sensor

3.1 Brief introduction of Au dendrite nanostructure

Scientists have studied the unique electrical and optical properties of three-dimensional metal nanostructures with high aspect ratio. The 3D metal nanostructures are traditionally formed on the electrode surface by electrochemical deposition with a template. The metal nanostructures have potential applications in plasmonics and biosensors. Recently, specific 3D nanostructures, which are similar to flower, tree and dendrite, have attracted considerable attention in chemical/biological research fields [3-1 – 3-3]. One of their unique characteristics is large surface area, which based on many blanching from the stem structure. The large surface area with the blanching contributes to promotion of photocatalytic activity [3-4] and immobilization of biomaterial [3-5]. In addition, the dendrite structure has excellent mechanical properties due to restricting excessive deformation. The structure dissipates the shear energy bands by propagating the high shear stress to the longitudinal direction in its construction [3-6].

Formation of dendrite nanostructure is often estimated to require an additive or a template for the growth of blanch structure in nanodendrite. Chen et al. reported that Ag dendrites were generated by the thermal reduction method in the presence of polyvinyl alcohol (PVA) using a photoreduction technique [3-7]. Xie et al. used a sponge-like nickel alloy as a template, reducing agents to synthesize Ag dendritic nanostructure [3-8]. In the fabricating method using additive, the diffusion of ions and anisotropic crystal growth play an essential role in branching from the stem structure.

In this chapter, dendritic gold nanostructures were introduced as one of the attractive and functional materials obtained by electroplating. Since the blanching depends on the ion diffusion with the electroplating condition, a dendritic structure with a large surface area can be obtained under appropriate conditions. In addition, dendritic Au nanostructures allow biomaterials to be immobilized on its gold surface via thiol linkages. Therefore, the dendrite Au nanostructures formed on the electrode of QCM-based sensor by varying the electroplating time, applied potential, and concentration of an additive. SEM observed several dendrite Au nanostructures depending on different electroplating conditions. Cyclic voltammetry estimated the effective surface area and determined the optimal electroplating condition. Finally, antigen-antibody interactions were monitored by QCM measurements with dendritic electrodes. The frequency shifts were evaluated to compare the sensitivity of two QCM-based sensors with dendrite structure and flat thin film.

3.2 Experimental details

All the reagents used for Au nanostructure fabrication and electrochemical evaluation were purchased from Electroplating Engineering of Japan (EEJA) and Wako Pure Chemical Industries. Anti-mouse IgG and mouse IgG were purchased from Funakoshi.

The dendrite Au nanostructures were fabricated on a SiO_2 substrate instead of a quartz substrate. Ti (30 nm thick) then Au (100 nm thick) were sputtered on the SiO_2 substrate using DC magnetron sputtering equipment. Au nanostructures formed on the Au thin film by electroplating with a Pt plate (cathode) and Ag/AgCl electrode (reference). The electroplating performed for 5 min using the Au plating solution containing poly

(ethylene glycol) (PEG1000, 50 ppm). The potential for electroplating was set from -0.9 to -1.05 V. Here, the QCM-based sensor after the electroplating is called dendrite QCM-based sensor. After rinsing the substrate with pure water, nanostructures were observed by SEM (JEOL JSM-7500F). We used the cyclic voltammetry (CV) composed of a three-electrode system to estimate the effective surface area of the dendrite Au nanostructures on the SiO_2 substrate. Each electrode composed of the Au thin film as a working electrode, a Pt mesh counter electrode, and the Ag/AgCl as a reference electrode. Here, an electrolyte contained sodium sulfate (0.1 M) and potassium ferricyanide (10 mM).

The interaction between an antigen (mouse IgG) and an antibody (anti-mouse IgG) was evaluated using QCM-based sensor. These reagents were adjusted with phosphate-buffered saline (PBS; pH = 7.4). In this experiment, a well-type cell combined with the QCM-based sensor. The QCM-based sensor had a fundamental frequency of 9 MHz. The diameter of the Au electrode on a QCM-based sensor was 5 mm. 300 nm thick Au film was sputtered on the titanium thin film (50 nm), which was worked as an adhesion layer between a quartz substrate and Au film, by DC magnetron sputtering system. In this study, the QCM-based sensor with a flat electrode is written as Au-thin-film QCM-based sensor. The QCM-based sensor was connected to a QCM analyzer (Seiko EG&G QCM 922A) and placed in a constant-temperature chamber to maintain room temperature.

Anti-mouse IgG and BSA immobilized on the electrode surface by thiol linkages, as shown below. The sensor was rinsed by PBS buffer after each immobilization. First, 25 μl of anti-mouse IgG of (100 μg/ml) was dropped and immobilized on the electrode for 10 min. 25 μl of BSA solution (0.01 wt%) was dropped and immobilized on it for 10 min to avoid nonspecific adsorption. The sensor chip combined with the well-type cell. Then, the cell with the chip placed at a thermostatic chamber. 495 μL of PBS was added

dropwise into the measurement cell, and the QCM analyzer monitored the frequency shift. After the frequency reached the steady-state, 5 µl of mouse IgG (10 µg/ml in total) was injected into the flow cell. The frequency shift on the antigen-antibody was measured to compare the sensitivity of Au-thin-film and dendrite QCM-based sensor.

3.3 Characterization of electroplated Au dendrite nanostructures

Fig. 3-1 shows the cross-sectional SEM images of electroplated dendrite Au nanostructures on Au/Ti/SiO_2 substrates. Each sample was electroplated under -0.9 (Fig. 3-1 (a)), -0.95 (Fig. 3-1 (b)), -1.0 (Fig. 3-1 (c)), and -1.05 V (Fig. 3-1 (d)) vs. the reference electrode for 5 min in the Au plating solution containing PEG1000 (50 ppm). The tallest dendrite structure was obtained under -0.95 V. A diameter of dendrites became larger on the higher applied potential. The gap between the dendrite structures narrowed according to the increase of the applied potential. The colors of the electroplated electrodes in Fig. 3-1 (a)-(c) appeared dark brown due to the diffuse reflection of visible light by the nanostructures. In contrast, the color of the electrode in Fig. 3-1 (d) showed light brown since the morphology of the electroplated structure became nearly flat, and the dendrite structures did not form on the electrode. Fig. 3-2 shows surficial SEM images of the electroplated structures on the Au/Ti/SiO_2 substrates. The electroplating conditions were the applied potential of –0.9 V for 5 min in the Au plating solution containing PEG1000 (50, 100, and 200 ppm, respectively). Fig. 3-2 (a) shows that the surface area of nanostructure was enlarged because of branching. In contrast, barnacle-like nanostructures with a size of 200–300 nm were formed under the electroplating condition with the PEG1000 concentration of 100 ppm, as shown in Fig. 3-2 (b).

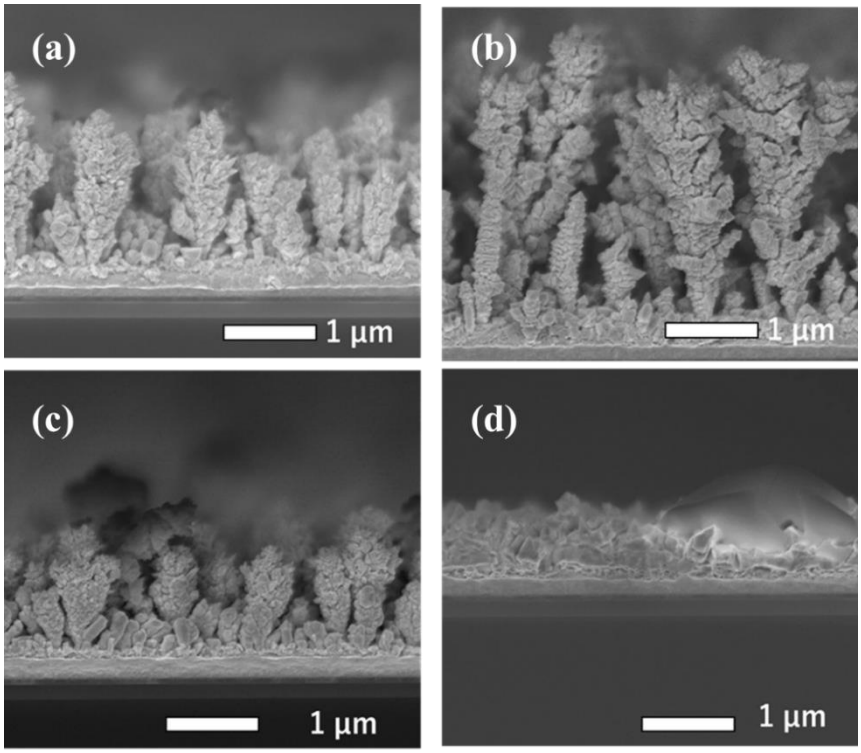

Fig. 3-1 Cross-sectional SEM images of the dendrite structures. All samples were applied the potential for 1 min. The applied potential was varied from -0.9 to -1.05 V: (a) -0.9, (b) -0.95, (c) -1.0, and (d) -1.05 V.

These nanostructures shaped trapezoidal, and the center of each structure dented with the shape of a reverse pyramid. By electroplating under a condition with the PEG1000 concentration of 200 ppm, nanocrystals were formed as approximately 100 nm, as shown in Fig. 3-2 (c). From these results, the morphology of the nanostructure depended on the PEG1000 concentration. The higher PEG1000 concentration inhibited the diffusion of Au ion by its absorption onto the electrode. Therefore, the inhibition of PEG100 promoted to grow a flattened film. SEM could observe an organic material with low conductivity. The branch structure formed by the different deposition rate on the substrate surface with PEG1000 adsorbed sparsely adsorbed.

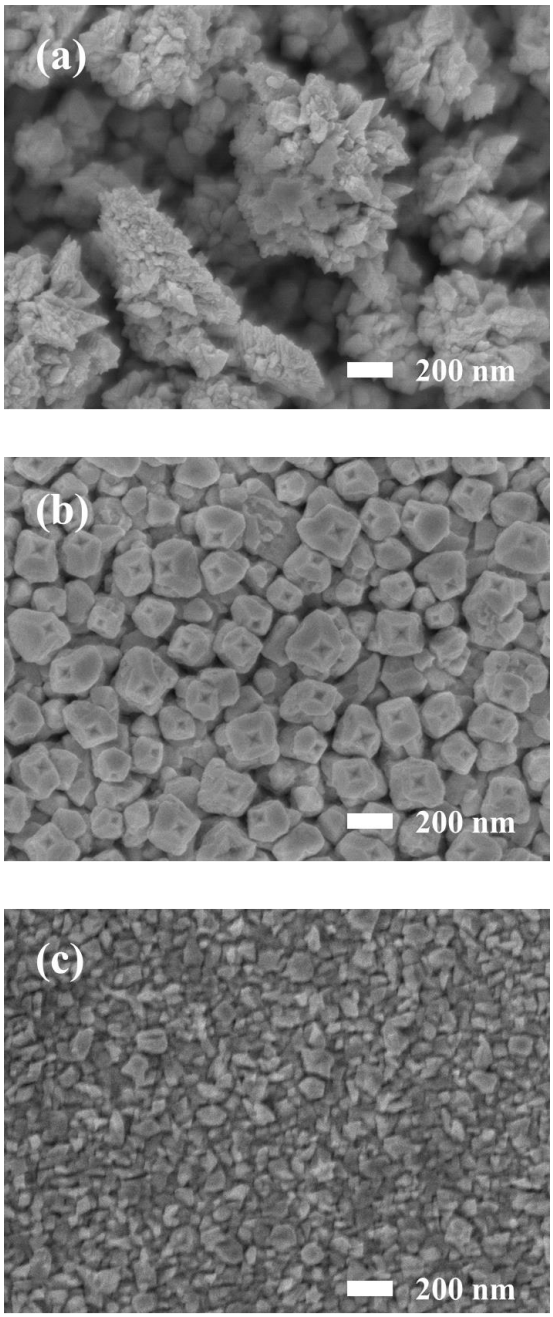

Fig. 3-2 Surficial SEM images of electroplated structures formed on the substrates under -0.9 V for 5 min in the Au plating solution containing different amounts of PEG1000: (a) 50, (b) 100, and (c) 200 ppm.

The growth process of dendrite structures was evaluated by the cross-sectional SEM images, as shown in Fig. 3-3 (a)-(e). The potential of -0.95 V was applied to form these structures. The electroplating time varied from 1 to 5 min. The Au electroplating solution contained PEG1000 (50 ppm). Fig. 3-3 (a) shows that small needles with a length of approximately 100 nm. The growth of the needles could be basis of a seed layer and a core of dendrite structures. In this condition (electroplating for 1 min), the branched structures were not observed. Nanopillars with small branches were obtained by the electroplating for 1.5 min, as shown in Fig. 3-3 (b). The concentration of the electric field promoted the vertical growth of the needles. Nanopillars was formed horizontally by the electroplating for 2 min, as shown in Fig. 3-3 (c). Several pyramidal branches formed from the small branches of the nanopillars. The height of the dendrite structures reached over 1 μm with increasing electroplating time, according to Fig. 3-3 (d). The dendrite structures were formed with a large surface area, as shown in Fig. 3-3(e), because numerous branches were formed from the top of the dendrites. In addition, the resonance resistance in the liquid phase was measured to compare the sensitivity of several QCM-based sensors with the Au-thin-film and dendrite structure (the potential of -0.95 V was applied for 1, 1.5, 2, 2.5, and 5 min). PBS buffer was used for this examination. The obtained resonance resistances were 360.58, 495.95, 610.31, 2514.23, over 10000, and over 40000 Ω respectively. The dramatic increase of the resonance resistances caused due to the morphology changes of the dendrite structures shown in Fig. 3-3. The dendrite structure contacted the buffer with each blanch structure. The contact between the buffer solution and dendrite structure absorbed oscillating energy which generated and propagated from the quartz. The energy was further dissipated due to the enlarged surface area contacting with solution according to the growth of dendrite structure. In addition, a

material with high density and toughness, such as gold, could absorb much energy because of the damped oscillation which related to the density and Young' modulus of the material. Therefore, the resonance resistance became higher due to the delayed propagation of the oscillation and the enlarged contact area according to the growth of the dendrite structure. This result agreed with other groups [3-9, 10].

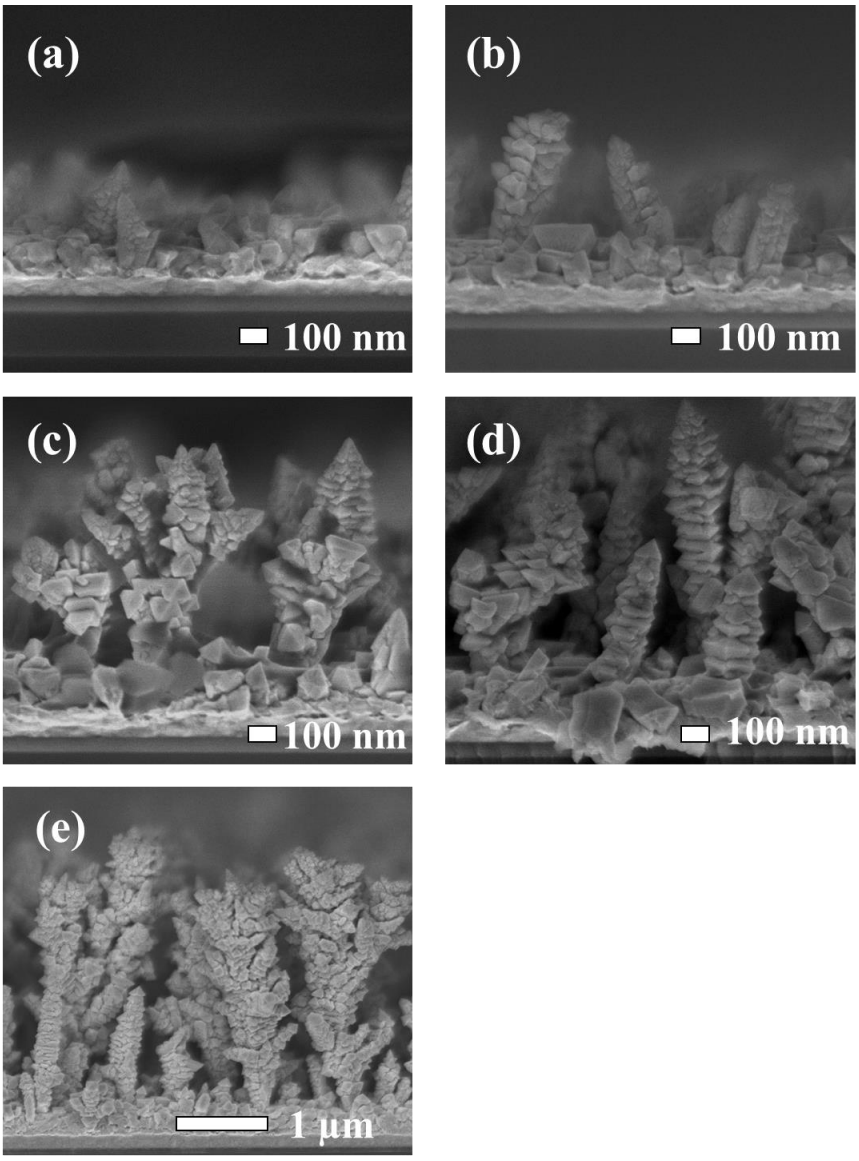

Fig. 3-3 Cross-sectional SEM images of the dendrite structure. The applied potential was -0.95 V. The Au electroplating solution contained 50 ppm of PEG1000. The electroplating time was set from 1 to 2.5 min: (a) 1, (b)1.5, (c) 2, (d) 2.5, and (e) 5 min.

3.4 Evaluation of effective surface area by electrochemical measurements

CV evaluated the effective surface area of the dendrite structures on the Au/Ti/SiO_2 substrates. The potential range was from -0.1 to 0.5 V vs. the reference electrode, and the sweep rate was 10 mV/s. Fig. 3-4(a) shows the cyclic voltammograms of the electrodes with several dendrites, which electroplated with several potential ranging from -0.9 to -1.05 V for 5 min. Fig. 3-4 (b) shows an enlarged view around the oxidation potential. The largest oxidation peak was obtained under the applied potential of -0.95 V. On the condition, the surface area was calculated to be 12.90 mm^2. This value was larger than that on the flat surface area (9.78 mm^2). By using the current at the oxidation peak, the effective surface area (A) was calculated from following equation [3-11].

$$\boldsymbol{A = \frac{i_p \times 100}{269 \times n \times c \times \sqrt{n \times D \times v}}} \quad \textbf{(3.1)}$$

where A, i_p, n, c, D, and v are the effective surface area (mm^2), the oxidation peak current (A), the reactive electron number (n=1 in this study), the concentration of potassium ferricyanide (10 mM), the diffusion constant of potassium ferricyanide (6×10^{-6} cm^2/s), and the sweep rate (10 mV/s), respectively. The magnitude of the oxidation peaks corresponded to the size of the nanostructure.

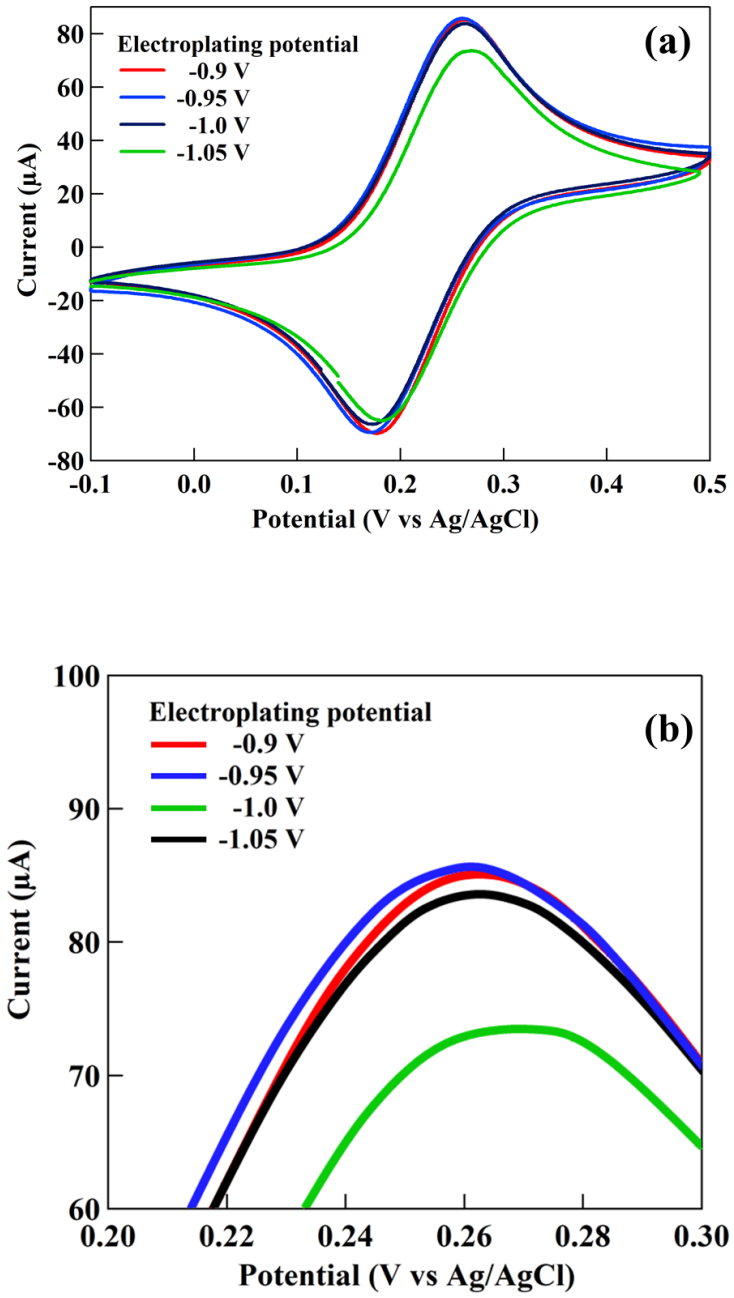

Fig. 3-4 Cyclic voltammograms (CVs) of the Au dendrite structures deposited on Au/Ti/SiO_2 substrates (red line: -0.9 V, blue line: -0.95 V, black line: -1.0 V, green line: -1.05 V). The electroplating time was 5 min for all samples. CVs (b) is enlarged figure of CVs (a). Cyclic voltammetry was performed in an electrolyte containing of sodium sulfate (0.1 M) and potassium ferricyanide (10 mM).

3.5 Detection of antigen-antibody reaction by dendrite QCM-based sensor

The dendrite QCM-based sensors measured antigen-antibody interaction to evaluate itself sensitivity. The dendrite structures were formed on the electrodes under -0.95 V for 1, 1.5, and 2 min. Au-thin-film QCM-based sensor worked as a reference to compare the frequency shift. The time-dependent frequency shift was shown in Fig. 3-5. Mouse IgG solution was loaded at 0 seconds. The measured frequency shifts were approximately 40, 80, and 110 Hz for the dendrite QCM-based sensors with electroplating time for 1, 1.5, and 2 min, respectively. In contrast, the frequency shift was approximately 55 Hz on Au-thin-film QCM-based sensor. The energy dissipation of dendrite QCM-based sensors was measured before the antigen-antibody interaction. The energy dissipation increased from 6, 33, and 131 $\times 10^{-6}$, according to the dimension of dendrite structure. These values agreed well with the morphology and the increase of frequency shift. Table 3-1 shows the standard deviation of the frequency shift due to the antigen-antibody interaction calculated from the results for four dendrite QCM-based sensors. For the dendrite QCM-based sensors under -0.95 V for 2 min, one of the samples did not operate. The standard deviation of the above dendrite chips was so high (42.72). In contrast, the standard deviation of other dendrite QCM-base sensor was low (10.89). One of the reasons was the low reproducibility of the dendrite structures, which formed by electroplating. The branch structure formed into various directions when the electroplating time was long. Therefore, the reproducibility was reduced to fabricate the dendrite QCM-based sensor, which had numerous branch structures, under -0.95 V for 2 min.

Table 3-1 Reproducibility of frequency shifts of the dendrite QCM-based sensor.

Sample	Frequency shift (Hz)				Average of frequency shift (Hz)	Standard deviation
-0.95 V, 1.5 min	80	70	80	100	83	10.89
-0.95 V, 2 min	110	30	80	N. D.	70	42.72

N. D.: No detected

The frequency shift of dendrite QCM-based sensor was smaller than that of the Au-thin-film QCM-based sensor. One of the reasons might be the inhibition of antibody immobilization by PEG1000, which adsorbed on the dendrite structure. Therefore, oxygen plasma treatment performed to remove the PEG1000 from the surface of dendrite QCM-based sensors, formed by electroplating for1, 1.5, and 2.5 min. After the oxygen plasma treatment, the antigen-antibody interaction measured with the same condition above. On the dendrite QCM-based sensor by electroplating for 1 and 1.5 min, the frequency shifts increased to approximately 60 and 110 Hz, respectively.

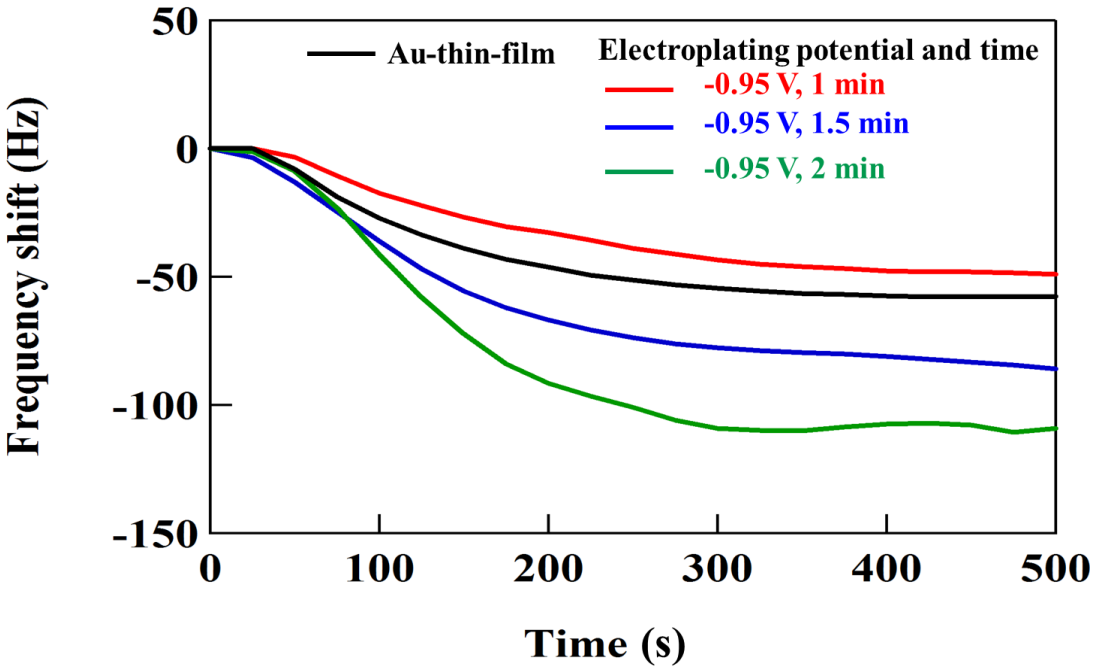

Fig. 3-5 Time-dependent frequency shifts of the dendrite and the Au-thin-film QCM-based sensors on the detection of the antigen-antibody interaction (red line: -0.95 V; 1 min, blue line: -0.95 V, 1.5 min, green line: -0.95 V, 2 min; and black line: Au-thin-film).

On the other hand, the frequency shift decreased to 90 Hz on the dendrite QCM-based sensor, which formed by electroplating for 2 min. The change in frequency shift resulted from the morphology change of the dendrite structures. SEM images (Fig. 3-7) showed the morphology of the nanostructure before and after the oxygen plasma cleaning. The dendrite structures were rounded, and some parts of nanostructures were broken after the oxygen plasma cleaning. Such damage might have occurred in the plasma treatment or during the preparation of the sensor chip.

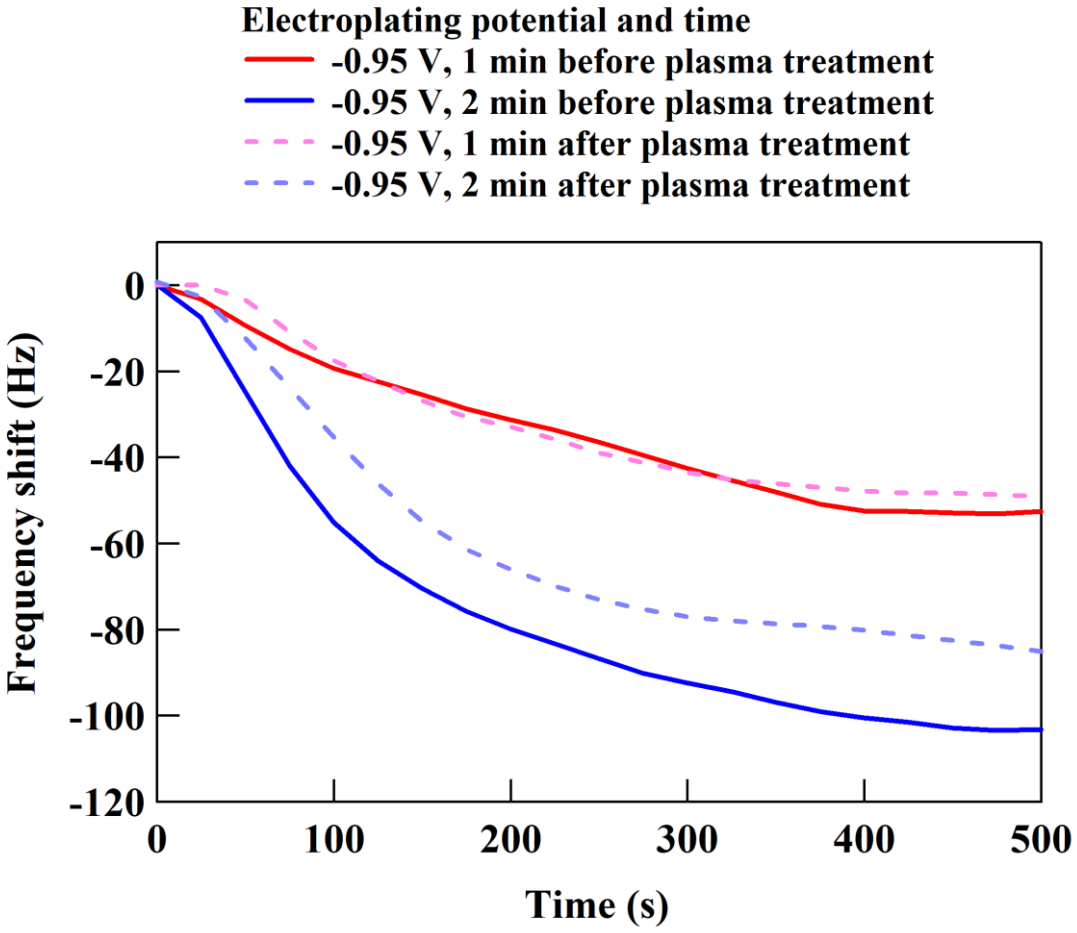

Fig. 3-6 Time-dependent frequency shifts of the dendrite QCM-based sensor before and after O_2 plasma cleaning to remove PEG1000 from the dendrite surface.

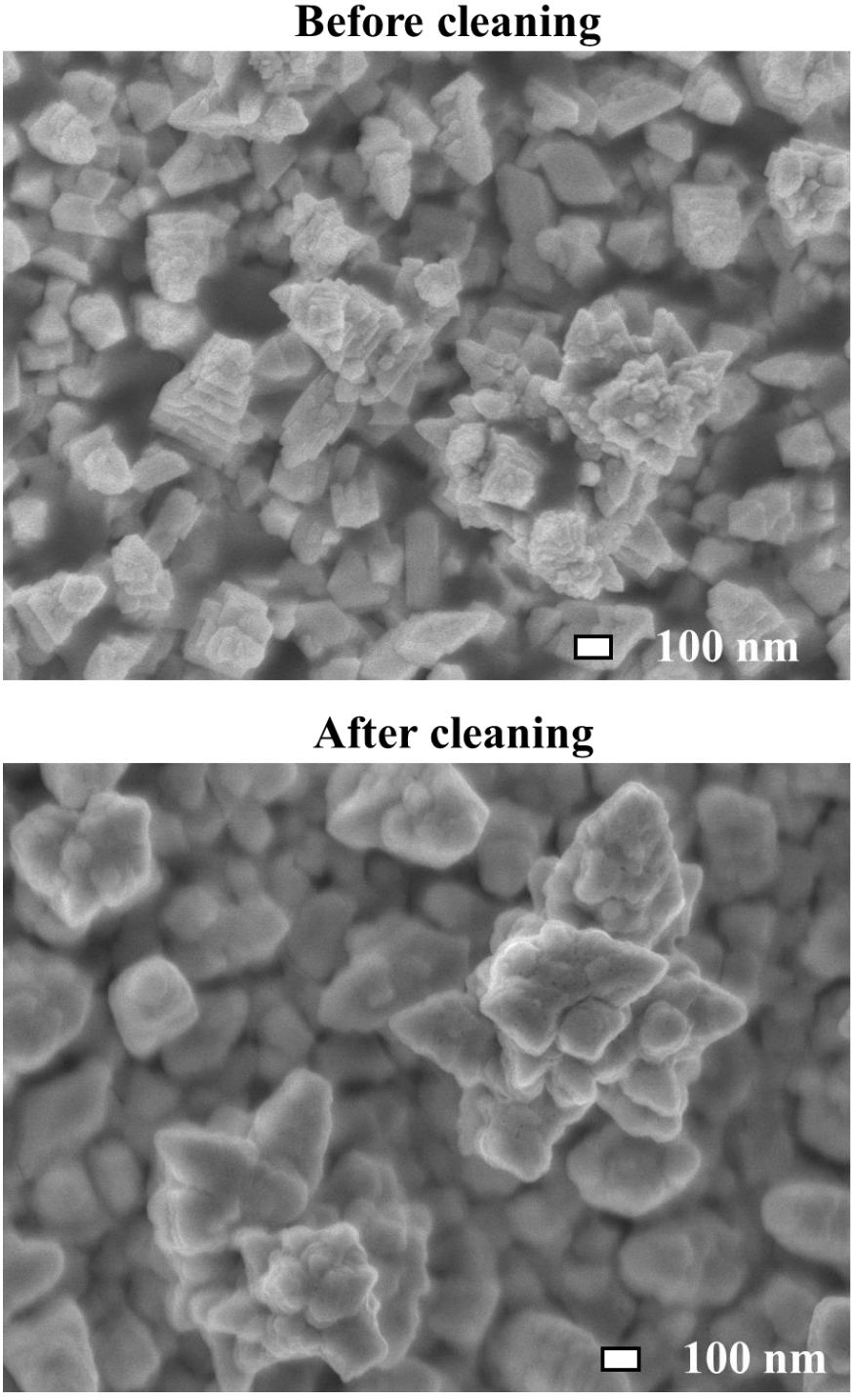

Fig. 3-7 Surface SEM images of the dendrite QCM-based sensor before (upper) and after (lower) O_2 plasma cleaning to remove PEG1000 from the dendrite surface.

3.6 Conclusions

Au dendrite structure was obtained on the electrode of a QCM-based sensor by electroplating to increase the surface area. Suitable electroplating conditions were the applied potential of -0.95 V and an electroplating time of 5 min to fabricate dendrite structure on the electrode of QCM-based sensor. Under these conditions, the tallest dendrite structure and the largest surface area were obtained, which was confirmed by SEM images and CVs. The dendrite QCM-based sensor, which fabricated by the electroplating time of 2.5 min under -0.95 V, did not operate to detect the conductance of the QCM because the resonance resistance was too high. When measuring an antigen-antibody interaction, frequency shifts of 40, 80, and 110 Hz were obtained by the dendrite QCM-based sensors electroplated for 1, 1.5, and 2 min, respectively. The sensitivity was improved compared with that of Au-thin-film QCM-based sensor.

The morphology of Au nanostructures changed drastically dependent with PEG1000 concentrations of 50, 100, and 200 ppm, forming dendrite, cube, and rough surface, respectively. Applied potential of -0.95 V was employed on these conditions. The height of dendrite Au nanostructures depended on the electroplating time. In addition, resonance resistance in liquid phase increased with the height. The highest dendrite Au nanostructure could be expected to obtain the largest frequency shift on antigen-antibody interaction. However, the noise level and standard deviation on the measurements were too large to obtain the accurate frequency shifts. The height of dendrite structure influenced on the oscillation of quartz crystal in liquid phase. The obtained resonance resistance showed the large dissipation of oscillating energy when the well-grown dendrite structure had many blanching. This chapter showed that the sensitivity related to the shape of the nanostructure.

References

3-1	X. Wen, Y.-T. Xie, M. W. C. Mak, K. Y. Cheung, X.-Y. Li, R. Renneberg, and S. Yang, Dendritic Nanostructures of Silver: Facile Synthesis, Structural Characterizations, and Sensing Applications. Langmuir 2006, 22, 4836-4842.
3-2	S. Thirumalairajan, K. Girija, V. Ganesh, D. Mangalaraj, C. Viswanathan, and N. Ponpandian, Novel Synthesis of LaFeO3 Nanostructure Dendrites: A Systematic Investigation of Growth Mechanism, Properties, and Biosensing for Highly Selective Determination of Neurotransmitter Compounds. Cryst. Growth Des. 2013 13, 291−302.
3-3	S. W. Lee, S. A. Cheon, M. Il Kim, and T J. Park, Organic–inorganic hybrid nanoflowers: types, characteristics, and future prospects. J Nanobiotechnol. 2015 13, 54.
3-4	H. Chen, and S. Yang, Hierarchical nanostructures of metal oxides for enhancing charge separation and transport in photoelectrochemical solar energy conversion systems. Nanoscale Horiz., 2016,1, 96-108.
3-5	P. Shende, P. Kasture, and R.S. Gaud Nanoflowers: the future trend of nanotechnology for multi-applications, Artificial Cells, Nanomedicine, and Biotechnology, 2018 46, 413-422.
3-6	G. He, J. Eckert, W. Löser, and L. Schultz, Novel Ti-base nanostructure–dendrite composite with enhanced plasticity, Nat. Mater., 2003 2, 33–37.
3-7	Y.Zhou, S. H. Yu, C. Y. Wang, X. G. Li, Y. R. Zhu, Z. Y. Chen. A Novel Ultraviolet Irradiation Photoreduction Technique for the Preparation of Single-Crystal Ag Nanorods and Ag Dendrites. AdV. Mater. 1999, 11, 850-852.
3-8	J. P. Xiao, Y. Xie, R. Tang, M. Chen, X. B. Tian, Novel Ultrasonically Assisted Templated Synthesis of Palladium and Silver Dendritic Nanostructures. AdV. Mater. 2001, 13, 1887.
3-9	J. Kondoh, Y. Matsui, S. Shiokawa, and W. Wlodarski, Enzyme-immobilized SH-SAW biosensor, Sens. Actuators., 1994 B 20, 199-203.
3-10	S. J. Martin, G. C. Frye, K. O. Wessendorf, Sensing liquid properties with thickness-shear mode resonators, Sens. Actuators A, 1994 44, 209-218.
3-11	A.J. Bard, and L. R. Faulkner, ELECTROCHEMICAL METHOD FANDAMENTALS AND APPLICATIONS, (John Wiley & Sons, New Jersey, 2001) p.231.

Chapter 4: Anodic Aluminum Oxide (AAO) nano-porous structure to improve a sensitivity on QCM-based sensor

4.1 Brief introduction of AAO nanostructure

Porous materials have been used in various research and industrial fields due to their large surface area, high rigidity, and high stability [4-1]. One of the features of porous films can absorb target materials such as gases or ions because of its large surface area with the high aspect ratio [4-2]. Therefore, the porous material is used to a filter and a solid catalyst. Although the porous materials are often consisted of inorganic composite such as silica, alumina, and titanium basically, an organic porous membrane has also been attracted attention because of easy-to-fabricate, environment friendly and biocompatibility. The organic porous membrane can be obtained by immersing a polymer mixture in a suitable gelling solution [4-3]. Another method to obtain a polymeric porous membrane is stretching of polytetrafluoroethylene (PTFE) shirt [4-4]. The use of organic materials allowed to form the porous structure easily. However, it is difficult to get a regularly ordered film with well-controlled thickness.

Sol-gel method is one of a process to fabricate a porous film in a liquid phase. A silica porous material is synthesized by polycondensation of silica alkoxides [4-5]. After mixing silica alkoxide and polymer with a strict stoichiometric ratio, the mixture forms a skeletal structure with the spinodal phase separation phenomenon. The mixture is annealed at 1500 ℃ and then the formed gel is removed efficiently from the skeletal structure. The strict stoichiometric ratio and annealing condition influenced on the controllability of the dimension of pore size significantly [4-6].

Anodization is one of electrochemical etching methods that forms a porous oxide film with enormous nanopores on the metal surface. Self-organized nanohole arrays are

formed downward from the surface with controllable dimensions [4-7]. Optimal anodic condition provides well-aligned arrays with triangle lattice and high aspect ratio. An electron beam lithography is known as a conventional technique for fabricating nanostructures with accurate dimension. However, this method is not suitable for large-scale production. In addition, the surface of the porous oxide film is functionalized with amino groups, epoxy groups, mercapto groups, and so on. The functionalization allowed the porous alumina to bind with other organic molecules or metals.

The above chapters found that structural durability, density, and rigidity of nanostructure contributed to the sensitivity of the QCM-based sensor. A theoretical simulation analyzed the rigidity of nanowire and nanohole array by applying vibration to the structures [4-8]. The nanohole array showed higher rigidity than nanowire from the point that propagating and dissipating the stress efficiently [4-8]. Therefore, the sensitivity of the QCM-based sensor would be improved by adopting the nanohole array to the electrode. In this chapter, AAO nanostructures were fabricated on a quartz substrate by anodizing an aluminum thin film in an oxalic acid solution. By changing the deposition time of the Al thin film, the thickness of AAO was ranged from 200 to 1000 nm. A diameter of the nanohole was changed from 45 to 80 nm by etching AAO nanostructures with phosphate acid solution. The calculated surface area of the AAO nanostructure could be enlarged as 13-folds than that of the Au thin-film surface. Electric admittance measurement analyzed the sensitivity of all QCM-based sensors with AAO nanostructure in a buffer solution to compare its contact surface area to the liquid phase. A large amount of biomolecule immobilized on the enlarged surface area. The results induced the improvement of the sensitivity. Therefore, the AAO-nanostructured QCM-based sensor is used to monitor antigen-antibody interaction to optimize the dimension of the

nanostructure. In addition, the sensing performance of both sensors was evaluated by a comparison of frequency shift corresponding to antigen-antibody interactions. Furthermore, the AAO-nanostructured QCM-based sensor attempted to detect an interaction between Bcl-2 (molecular weight: 26 kDa) and Bcl-2-associated X protein (Bax, molecular weight: 21 kDa) as an application of detection of protein-protein interaction. Finally, the dissociation rate constant was evaluated for the antigen-antibody and Bcl-2-Bax interactions.

4.2 Experimental details

All the reagents used for AAO nanostructure fabrication were purchased from Wako Pure Chemical Industries. Anti-mouse IgG and mouse IgG were purchased from Funakoshi Co., Ltd. QCM-based sensor (QA-A9M-AU(M)(SEP), SEIKO EG&G) had the Au electrodes on both sides of quartz with the electrode diameter of 5 mm and thickness of 300 nm. The fundamental frequency of the QCM-based sensor was 9 MHz. A QCM analyzer (QCM 922A, Seiko EG&G) swept resonant frequency with overtone (N=1) from 8.7 MHz to 9.2 MHz.

Fig. 4-1 shows a schematic image of the fabricating process for the AAO-nanostructured QCM-based sensor. Titanium thin film (thickness of 25 nm) and Aluminum thin films (thicknesses were 200, 400, 700, and 1000 nm) were deposited on a quartz substrate (fundamental frequency: 9 MHz) in order by using DC magnetron sputtering equipment. The diameter of the electrode was set to be 5 mm. An AAO nanostructure was obtained by anodizing the Al thin film in 0.3 M oxalic acid solution with a glassy carbon electrode as the counter electrode. The applied potential was set as 40 V. This anodic condition was suitable for the formation of a self-assembled nanohole

array [4-9]. After the anodization, the nanohole diameter was enlarged to 40, 60, and 80 nm by immersing in 5 wt% phosphoric acid solution. The immersing performed for 30, 60, and 90 min, respectively. The nanostructure was fabricated on one side of the quartz substrate. The other side coated with Indium Tin Oxide (ITO) and Au (25 and 100 nm thicknesses) using the sputtering method in order.

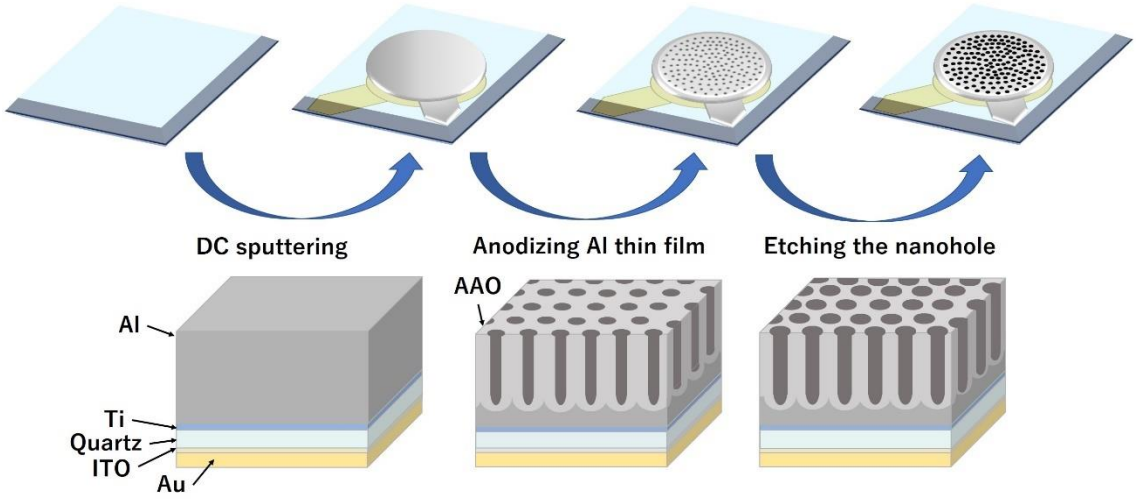

Fig. 4-1 Schematic image of fabricating process of QCM-based sensor with AAO nanostructure.

A self-assembled monolayer (SAM) with an amino terminal group was formed on the surface of the AAO nanostructure to immobilize with biomolecules, as shown in Fig. 4-2 [4-10]. The SAM was formed as below procedures: the AAO-nanostructured QCM-based sensor was immersed for 1 h at 65 ºC in a toluene solution of 3-aminopropyltriethoxysilane (toluene: 3-aminopropyltriethoxysilane = 99:1). After sonicating with 2-propanol, SAM became stable with the dehydration reaction of SAM by baking for 30 min at 110 ºC. Then, stable SAM formed on the surface of the AAO-nanostructure.

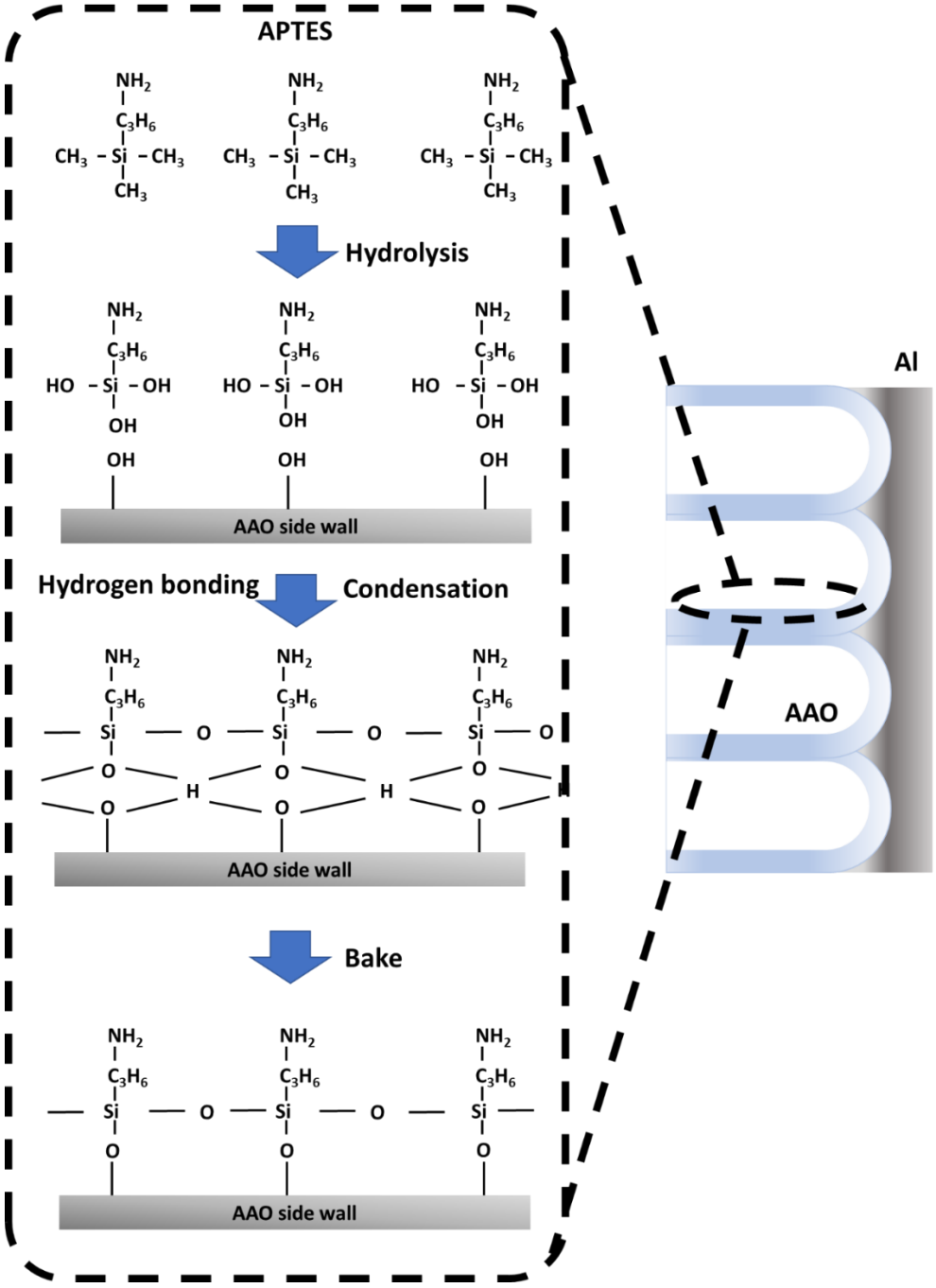

Fig. 4-2 Schematic image of SAM formation on a surface of AAO nanostructure. SAM made of APTES with NH_2 as their terminal groups is used to immobilize biomolecule via amid linkage.

The interaction between an antigen (mouse IgG) and an antibody (anti-mouse IgG) was evaluated using the QCM-based sensor. 10 mM tris(hydroxymethyl)

aminomethane (Tris-HCl; pH = 7.4) was used as a buffer solution. The QCM-based sensor was connected to a QCM analyzer and placed at a constant-temperature chamber to maintain room temperature.

A total of 25 μL of anti-mouse IgG (100 μg/mL) coated on the electrode for 30 min. After rinsing the sensor with Tris-HCl, 25 μL of BSA solution (0.01 wt%) coated on the sensor surface and kept for 30 min to avoid nonspecific adsorption. Here, the anti-mouse IgG and BSA immobilized on the amino group of the SAM [4-10].

The QCM-based sensor was combined with a well-type cell (QA-CL4PK, SEIKO EG&G). After loading of 495 μL of Tris-HCl into the well-type cell, the QCM counter started monitoring the frequency shift. After the frequency reached the steady-state, the frequency shift on the antigen-antibody reaction was measured by injecting 5 μL of mouse IgG (10 μg/mL in final concentration). In addition, the frequency shifts depending on the thickness and the diameter of the AAO nanostructure were evaluated. Here, Au-thin-film QCM-based sensor with flat electrode was used as a reference. The calibration curves were obtained using final IgG concentration ranging from 0.1 to 100 μg/mL.

4.3 Morphology of AAO nanostructures

Scanning electron microscopy (SEM) observed the surface and side view of AAO nanostructure, as shown in Fig. 4-3 (a), (b), and (c). All nanostructures were fabricated on the SiO_2/Si substrate to avoid image distortion caused by electric charge. The diameter in Fig. 4-3 (a) and (b) was approximately 60 nm and 40 nm, respectively. The nanohole diameter depended on the immersing time in the phosphoric acid solution. The nanoholes in AAO nanostructure were vertically well aligned and distributed evenly on the substrate. The thickness of the AAO nanostructure was about 1000 nm, as shown in Fig. 4-3 (c).

Although AAO nanostructure has an advantage that nanohole array can be formed evenly, the nanohole diameter and growth direction distributed randomly at the top of the AAO nanostructure comparing to those at the bottom. The reason attributed to the first formation of small nanoholes, which was electrolyzed and grown along with the grain boundary of the as-sputtered Al thin film [4-9]. According to the growth of the nanoholes, the diameter of nanoholes and structure growth direction were uniform at the bottom.

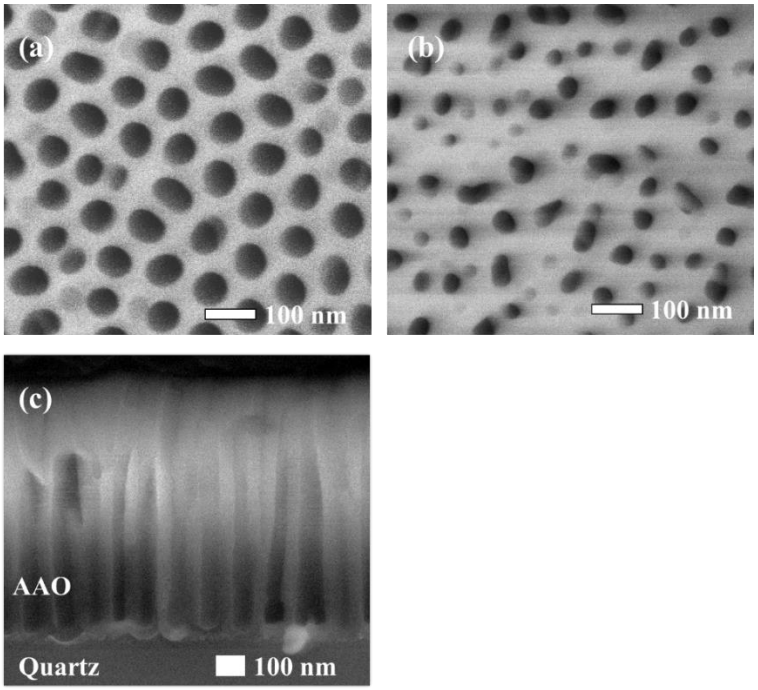

Fig. 4-3 SEM images showing the morphology of AAO nanostructures. Top view of the AAO nanostructure with nanohole diameter of 60 nm (a) and 40 nm (b). Cross section image of AAO nanostructure with 1000 nm thickness (c).

4.4 Comparison of resonant characteristics of AAO-nanostructured and Au-thin-film QCM-based sensors

The resonant characteristics in the air were measured by electrical admittance, as shown in Fig. 4-4 (a). Here, the AAO-nanostructured QCM-based sensor had nanohole array with a diameter of 60 nm and a thickness of 700 nm. The resonant frequency in this

work was evaluated by using the conductance peak. The peak value of the AAO-nanostructured QCM-based sensor (conductance = 0.103 S) was increased comparing with one of the Au-thin-film QCM-based sensor (conductance = 0.066 S), as shown in Fig. 4-3 (a). Zhu et al. compared mass sensitivity of Au and ITO electrodes on the quartz crystal [4-11]. The ITO electrode showed the higher mass sensitivity than the Au electrode due to a density and material rigidness. Their results suggested that mechanical properties on the electrode affected resonant characteristics of QCM-based sensor. In this work, the Vickers hardness of aluminum oxide and gold are 14.5 GPa and 216 MPa, respectively. The oscillation generated from a quartz surface could propagate efficiently without large decay in AAO-nanostructured electrode comparing with the gold electrode. Additionally, the resonant frequency increased from 8.95 MHz to 9.01 MHz. The mass-loaded on the surface of the quartz was decreased due to the density of the materials. The densities of aluminum oxide and gold are 3.95 and 19.32 g/cm^3. Each mass loaded on the quartz were calculated as 19.5 μg (AAO nanostructure) and 113.6 μg (Au-thin-film) which were estimated from electrode conditions (diameter: 5 mm, thickness: 700 nm in AAO nanostructure and 300 nm in Au-thin-film, nanohole diameter: 60 nm, nanohole density: 100 holes per μm^2). On the AAO-nanostructured QCM-based sensor, their excellent hardness and lower density contributed to the efficient propagation of the oscillation from the quartz to its structure. Therefore, the AAO-nanostructured QCM-based sensor had a sharp conductance peak concerning the mass sensitivity and the resonant frequency.

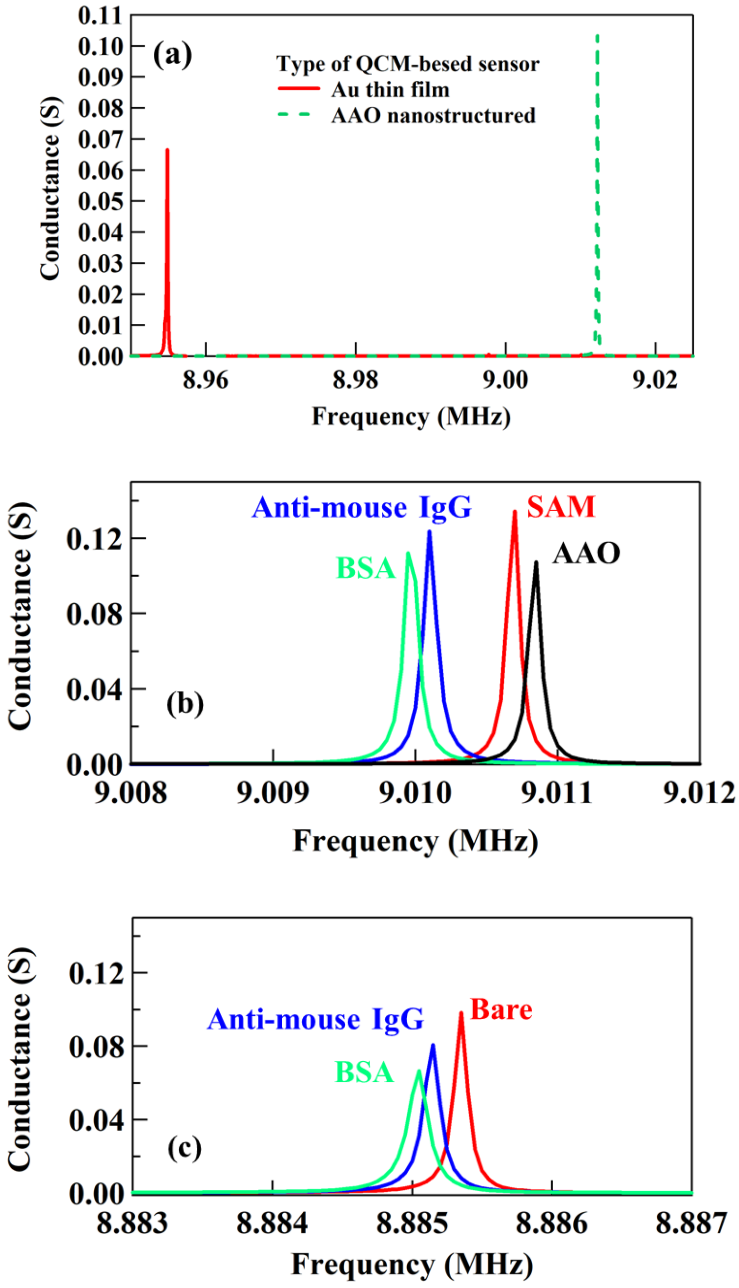

Fig. 4-4 Results of admittance measurements for QCM-based sensors. (a): Resonant characteristics of AAO-nanostructured (dashed green line) and Au-thin-film (solid red line) QCM-based sensors. (b), (c): Resonant characteristics of AAO-nanostructured QCM-based sensor (b) and Au-thin-film QCM-based sensor (c) through the coating process for the IgG detection.

Table 4-1 Resonant resistances dependent with the thickness and diameter of AAO nanostructure. All the measurements were carried out in 10 mM Tris-HCl buffer. Unit of conductance was Ω.

AAO thickness (nm)	AAO nanohole diameter (nm)		
	40	60	80
200	328.2	358.3	414.6
400	334.6	374.5	679.2
700	339.9	392.2	826.1
1000	341.7	434.1	1083.6

Electrical admittance measurement performed to analyze the resonant resistance in the buffer solution with various AAO nanostructured QCM-based sensors, and the results were listed in Table 4-1. The resonant resistance expresses the loss of oscillation energy by the solvent in the surrounding medium. These results indicated the loss of oscillation energy increased in the buffer solution because of the enlarged contact area of AAO nanostructure for the buffer solution. Fig. 4-4 (b) shows the resonant characteristics of the AAO-nanostructured QCM-based sensor with a thickness of 700 nm and a nanohole diameter of 60 nm after the binding of SAM, anti-mouse IgG, and BSA. All measurements were performed in the air. In each preparation step, the resonant frequency shifted with -150, -500, and -450 Hz, respectively. The mass load increased according to each preparation step since the biomolecules accurately immobilized on the surface of the AAO nanostructure [4-12]. The 2-3 folds amount of antibody was immobilized on the AAO surface comparing the flat Au surface, as shown in Fig. 4-4 (b) and (c). Therefore, the AAO-nanostructured QCM-based sensor could detect the anti-mouse IgG and IgG interaction with large frequency shifts.

4.5 Optimization of the dimension of AAO nanostructure in QCM measurement

Frequency shifts by the antigen-antibody interaction were evaluated to optimize the dimension of the nanostructure, as shown in Fig. 4-5. Mouse IgG was injected into a well-type cell with the QCM-based sensor at 0 s. In this work, a frequency shift at 200 s was defined as the maximum value because of the saturation of frequency shift on the Au-thin-film QCM-based sensor. The frequency shift did not reach the equilibrium state in the buffer solution with some pulse-like noises on the AAO-nanostructured QCM-based sensor with a nanohole diameter of 80 nm. Therefore, the measurement did not perform in the above condition. This behavior was observed in the previous research [4-13], and the Au dendrite structure improved the sensitivity of the QCM-based sensor. However, an extensive noise caused from the dimension of a large Au dendrite structure. The physical and mechanical properties of gold, such as large height and low rigidity of the nanostructure, led an unstable state with significant noise by the large resonant resistance. Mouse IgG adhesion changed the resonant frequency shift to -45 Hz on the Au-thin-film QCM-based sensor. When the nanohole diameter was 60 nm, the obtained frequency shifts were -96, -114, -130, and -140 Hz according to the AAO thickness, as shown in Fig. 4-5 (a). When the nanohole diameter was 40 nm, the obtained frequency shifts were -75, -90, -100, and -105 Hz according to the AAO thickness, as shown in Fig. 4-5 (b). The frequency shift increased with the nanohole diameter for all AAO thicknesses. Biomolecules diffuse difficulty into the small nanoholes because of physical and electrostatic inhibitions, as reported by Orita et al. [4-14].

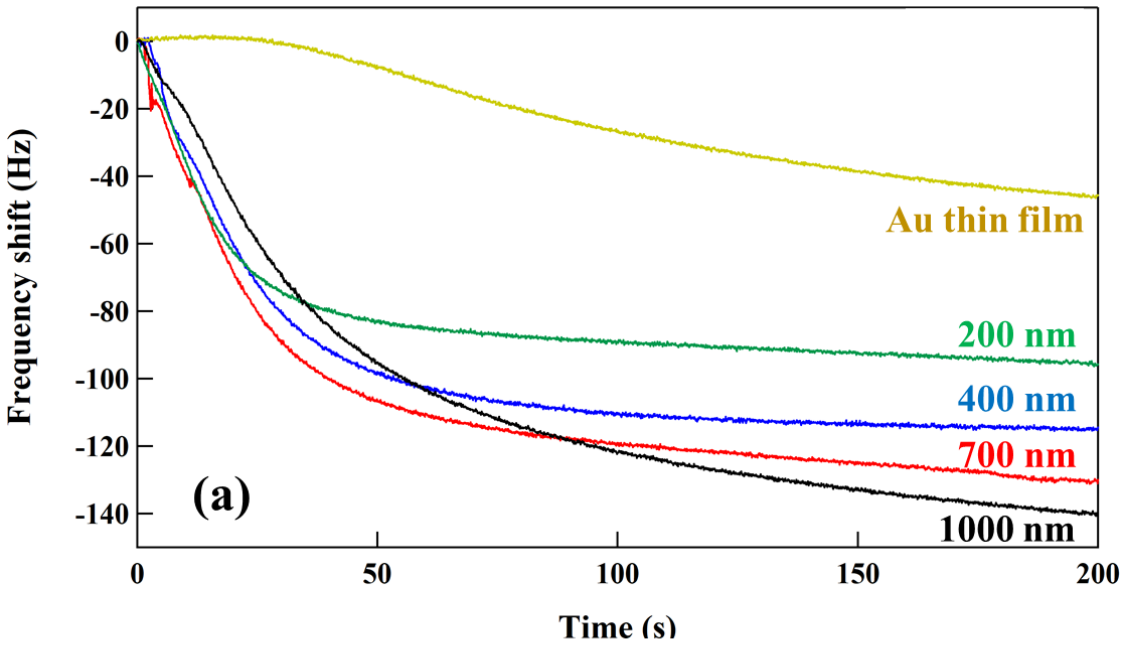

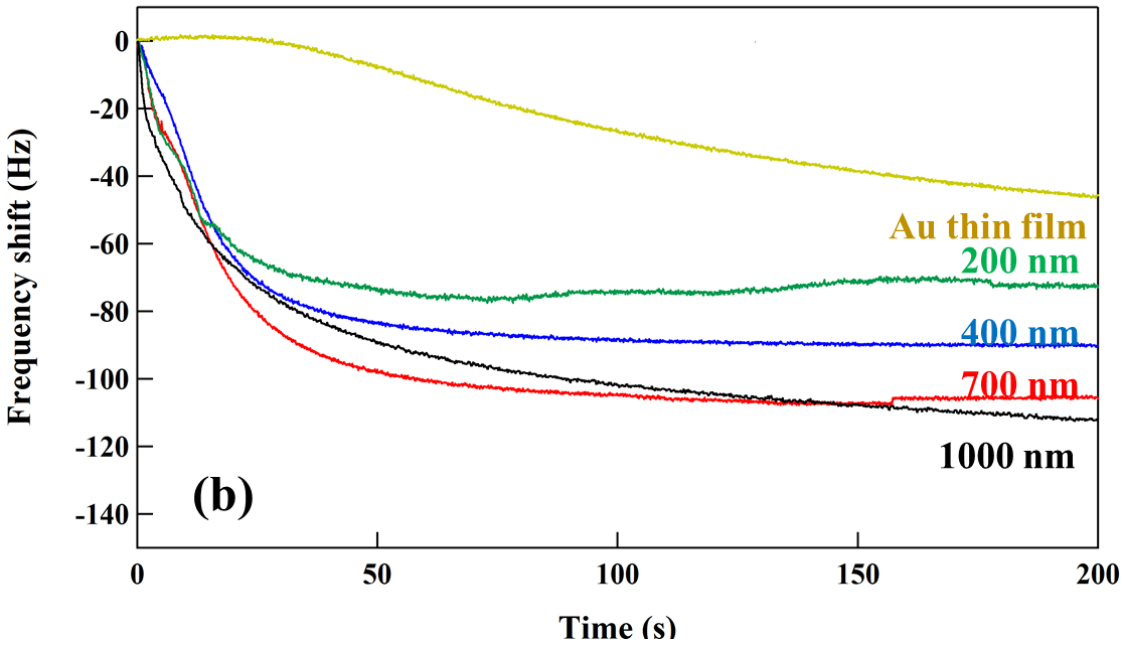

.

Fig. 4-5 Time-dependence frequency shifts on the interaction between anti-mouse IgG and mouse IgG. Thickness and diameter of AAO nanostructure were changed from 200 to 1000 nm. (a) and (b) show the results with nanohole diameter of 60 and 40 nm, respectively. Both spectra colors show thickness of AAO nanostructure (red line: 200 nm, blue: 400 nm, green: 700 nm, black: 1000 nm, yellow: Au-thin-film).

Fig. 4-6 shows the standard deviation and average values of the obtained frequency shift for the antigen-antibody interaction. AAO nanostructure on the quartz had a nanohole diameter of 60 nm and a thickness of 200, 400, 700, and 1000 nm. Final concentration 10 μg/ml of mouse IgG was used for this experiment. The average values of the obtained frequency shift were -98.5, -111.5, -141.2, and -148.7 Hz, respectively. These data were an average of four independent QCM measurements. The frequency shift increased linearly with the thickness of the AAO, ranging from 200 to 700 nm, as shown in Fig. 4-6.

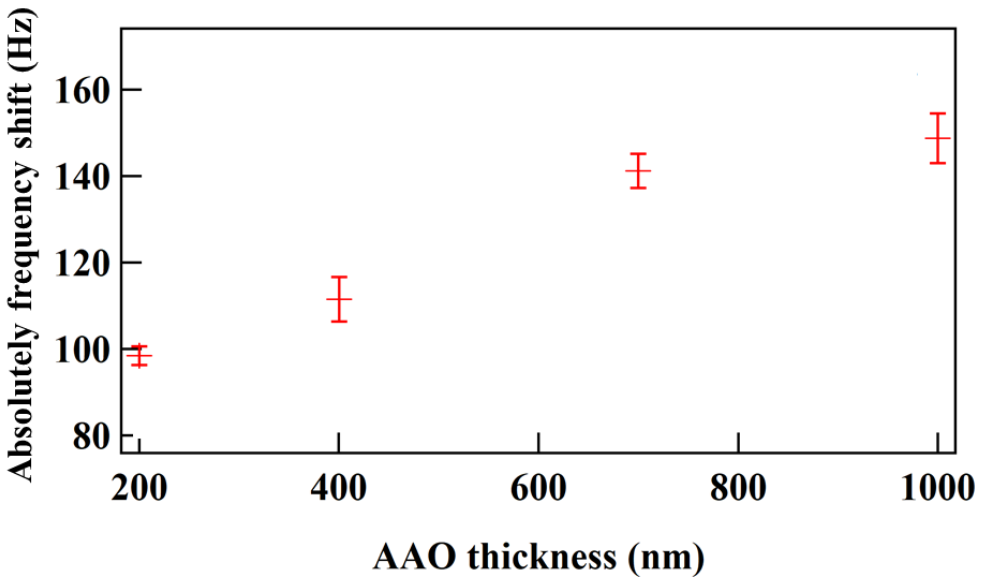

Fig. 4-6 Frequency shifts with standard deviation were measured via the antigen-antibody interaction depending on thickness of AAO nanostructure.

The results indicated that the AAO-nanostructured QCM-based sensor detected efficiently target antigen on this range. As mentioned in Fig. 4-4, the top of the nanostructure could not contribute to improving the sensitivity due to the large oscillation energy loss in the buffer solution. Another research group reported that the oscillation,

which generated from the surface of the quartz, decayed gradually with a distance from the quartz surface in the buffer solution [4-15]. Correctively, the AAO nanostructure of 1000 nm thickness was not suitable for the measurement. Then, the optimal dimension of AAO nanostructure for QCM was determined as a thickness of 700 nm and a nanohole diameter of 60 nm.

4.6 Detection of antigen-antibody interaction and evaluation of sensing performance of AAO-nanostructured QCM-based sensor

Both QCM-based sensors were compared by calibration curves at the IgG concentration ranging from 0.1 to 100 μg/mL, as shown Fig. 4-7. The frequency shifts saturated at more than 10 μg/mL for both QCM-based sensors. The increase ratio of the frequency shifts on the AAO-nanostructured QCM-based sensor to the reference was calculated from 2 to 3. Because AAO nanostructure expanded the adsorption surface area by its high aspect ratio nanohole array. The calibration curves fitted the plots with a linear regression model. The correlation coefficients (R^2) were calculated as 0.9884 (AAO-nanostructured) and 0.9917 (Au-thin-film). These values indicated a strong correlation between the plots and the regression model in the linear area. The detection limits were calculated as 0.20 and 0.48 μg/mL for the mouse IgG according to signal/noise = 3 with the regression model. The noise levels were ±1 Hz in the AAO-nanostructured QCM-based sensor and ±3 Hz in the Au-thin-film QCM-based sensor.

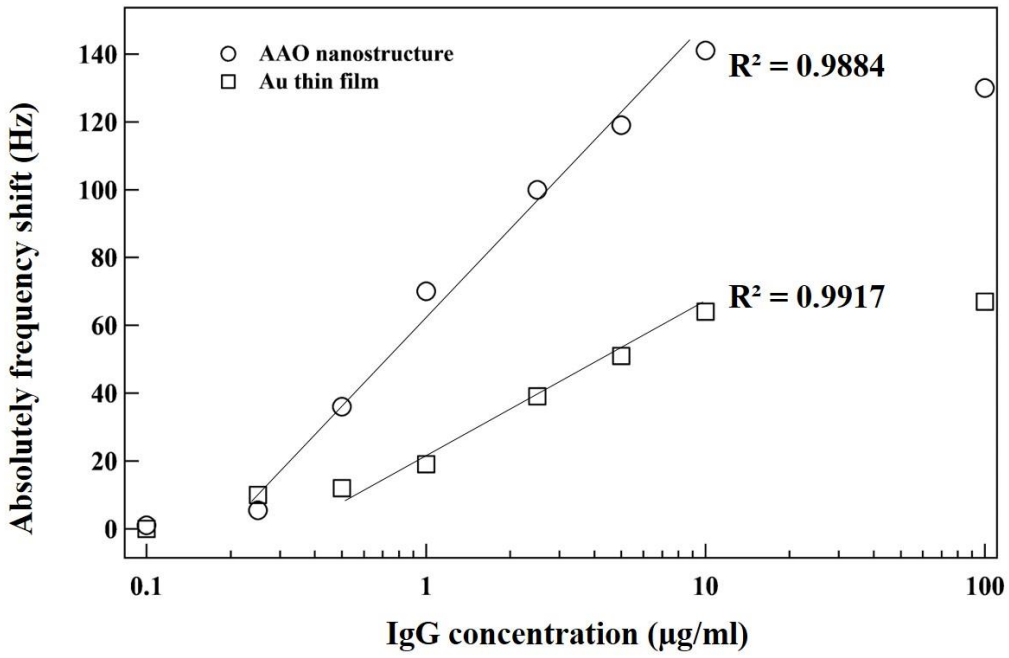

Fig. 4-7 Calibration curves measured by AAO-nanostructured and Au-thin-film QCM-based sensors. AAO nanostructure with 700 nm thickness and 60 nm diameter was fabricated on the quartz. Circles show results by AAO-nanostructured QCM-based sensor. Squares show results by Au-thin-film QCM-based sensor.

Table 4-2 shows the saturation times for the obtained frequency shifts. In this case, the mouse IgG concentration ranged from 0.5 to 10 μg/mL. The saturation time was defined as $0.9 \times \Delta f$. The diffusion distance between the buffer solution and the sensor surface could contribute to the shorter saturation time. In this study, AAO-nanostructured QCM-based sensor had thicker electrode than that of Au-thin-film QCM-based sensors. In addition, the saturation time depended on the thickness of AAO nanostructure, as shown Fig. 4-5. Table 4-2 further shows that the saturation time decreased with increasing the mouse IgG concentration. The diffusion of mouse IgG in the entire buffer solution was affected by the concentration of mouse IgG. Therefore, the diffusion could be quicker at high concentration of mouse IgG.

Table 4-2 Saturation time obtained by both sensors with/without AAO nanostructures having nanohole diameter of 60 nm and thickness of 700 nm. IgG concentration ranged from 0.5 to 10 μg/mL.

IgG concentration (μg/mL)	Type of QCM-based sensor	
	AAO-nanostructured	Au thin film
0.5	177	180
1	159	164
2.5	108	114
5	113	116
10	93	112

Unit: second

4.7 Impact of detecting Bcl-2 and Bax interaction

In the program to develop a novel methodology to detect PPI inhibitors, some scientists have focused on the interaction between Bcl-2 (molecular weight: 26 kDa) and Bcl-2-associated X protein (Bax, molecular weight: 21 kDa). Inhibiting this interaction will lead to the apoptosis of cancer cells. Members of the Bcl-2 family of proteins are essential in regulating apoptosis [4-16]. Many research groups investigated the effects of Bcl-2, Bcl-extra large (xL), and Bax protein in the regulation of the apoptosis of mesangial cells [4-17]. Binding of Bax to the pocket of Bcl-2 suppressed apoptosis of the cells. Therefore, Bcl-2 inhibitors are potent candidates for the treatment of cancer. Most research groups have used ELISA and western blot analysis to detect Bcl-2-related interactions [4-18, 4-19], and a few groups have attempted to use SPR [4-20]. However, no group has ever shown the possibility of using a QCM to measure the interaction of Bcl-2 and Bax. Considering the molecular weight of Bax and Bcl-2, a conventional QCM-

based sensor misses occurring the interaction due to its low sensitivity.

The above section discussed the improvement of the sensitivity by the large surface area of AAO nanostructure. The AAO-nanostructured QCM-based sensor detected the anti-mouse IgG and IgG interaction with 2-3 folds larger frequency shifts comparing the Au-thin-film QCM-based sensor. However, the molecular weight of IgG was 150 kDa that both QCM-based sensor detects easily. Here, the AAO-nanostructured QCM-based sensor attempted to detect the Bax and Bcl-2 interaction as a biosensing application for low-molecular-weight biomaterials. A successful detection will let the AAO-based QCM-based sensor to contribute to the development of the inhibitor in the drug discovery field.

4.8 Experimental details

The evaluation of the sensing performance determined the optimal dimension of AAO nanostructure. Then, the thickness of 700 nm and the diameter of 60 nm were adopted to AAO nanostructure to detect PPIs. Anti-Bcl-2 (mAbs), Bcl-2, and bovine serum albumin (BSA) were purchased from Funakoshi Co., Ltd. 4-(2-hydroxyethyl)-1-piperazineethanesulfonic acid (HEPES, 10 mM, pH=7.6) was used as a buffer solution. After modification of SAM on the AAO surface, 25 μL of anti-Bcl-2 (100 μg/mL) was added dropwise to the electrode for 30 min to bind it on the AAO-nanostructure. After washing with HEPES buffer solution to prevent the nonspecific adsorption of anti-Bcl-2, 25 μL of BSA solution (0.01 wt%) was added dropwise over 30 min to avoid nonspecific adsorption. Then, it was rinsed by the HEPES buffer solution again. Here, the anti-Bcl-2 and BSA immobilized on the AAO surface by amide linkages between the amino group

on the SAM and the carboxyl group included in the biomolecules. In contrast, QCM-based sensor with Au flat electrode was used as a benchmark. The electrode was coated by only dropping solution, including anti-Bcl-2 (100 μg/mL) and BSA (0.01 wt%) in order. These proteins bound on the Au electrode through thiol binding. These QCM-based sensors combined with a measurement cell, which connected to a flow injection system. The measurement cell had a flow cell, an inlet, and an outlet made of poly(dimethylsiloxane) (PDMS). The depth and diameter of the flow cell were 1 and 5.5 mm, respectively. The QCM-based sensor and the measurement cell placed at the constant-temperature chamber to maintain the room temperature. The sensor connected to a QCM analyzer. The overtone number set to three (n=3); thus, the operating frequency was 27 MHz. A syringe pump controlled a flow rate of 5 μl/min. the frequency shift was measured corresponding to the antigen-antibody reaction by injecting Bcl-2 firstly. Consequently, we also load several concentrations of Bax to demonstrate the interaction between Bcl-2 and Bax. All injected volume was 50 μl.

4.9 Resonant characteristics of AAO-nanostructured QCM-based sensor according to Anti Bcl-2 immobilization

The resonant characteristics of the fabricated QCM-based sensors during the preparation process are shown in Fig. 4-8. Here, Fig. 4-8 (a) shows the characteristics of the QCM-based sensor coated with the AAO-nanostructured electrode and Fig. 4-8 (b) shows those for the Au-thin-film QCM-based sensor. All the measurements were carried out in air. The antibody immobilization resulted in -1200 Hz of the frequency shift on the AAO-based QCM-based sensor. In the case of the flat Au electrode, the immobilization of antibody decreased in the resonant frequency to -400 Hz. In fact, the frequency shift

on the AAO-nanostructured electrode was three times larger than that on the flat surface in the antibody-binding process. The result indicated that the mass load of the antibody increased owing to the large surface area of the AAO nanostructure. In addition, the resonant frequency did not change after the binding of BSA for both electrodes. The data indicate that there was very little space for the binding of BSA to the electrode surface. Therefore, the increase of mass resulted from the biomolecules immobilized accurately on the surface of the AAO nanostructure.

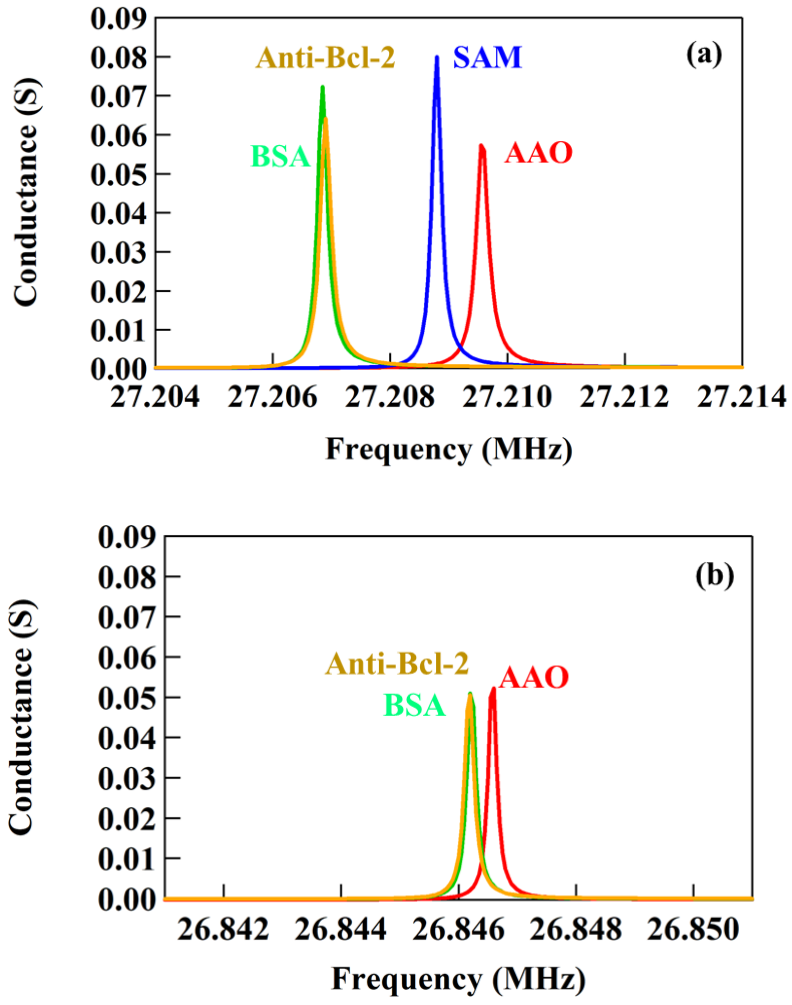

Fig. 4-8 Resonant characteristics of QCM-based sensor with the AAO nanostructure (a) and Au-thin-film (b) after each preparation process by using admittance measurements.

4.10 Measuring time-dependent frequency shifts corresponding to Bcl-2 and Bax interaction

The interaction between an antigen (Bcl-2) and an antibody (anti-Bcl-2) and interaction between two proteins of Bcl-2 and Bax were evaluated using the QCM-based sensors with AAO nanostructure or Au-thin-film. Firstly, a real-time monitoring carried out to measure the frequency shift corresponding to the adhesion of Bcl-2 to anti-Bcl-2, following that for the adhesion of Bax to Bcl-2. These conditions were the same for the fabricated QCM-based sensor with AAO nanostructure. In this experiment, Bcl-2 (10 µg/mL) was injected after the resonant frequency reached the steady-state. After measuring the interaction between anti-Bcl-2 and Bcl-2, Bax (10 µg/mL) was also injected to monitor the interaction between Bcl-2 and Bax. The obtained time-dependent frequency shift is shown in Fig. 4-9. Arrows in the figure show the time on the sample injection. The resonant frequency on both electrodes started to decrease approximately 20 min after the Bcl-2 injection. For the Au-thin-film, the resonant frequency decreased slightly with flowing the Bcl-2 solution over the sensor. However, the frequency shift increased until zero-level again after the reaction. Then, there was hardly any frequency shift after Bax injection since Bcl-2 did not interact on the anti-Bcl-2. In contrast, the AAO-nanostructured QCM-based was able to detect the interaction of Bcl-2 and anti-Bcl-2 from the point that remained the frequency shift after the interaction. In this case, the frequency shift was about 36 Hz. In addition, the resonant frequency also started to decrease about 23 min after Bax injection. The frequency shift was about 37 Hz.

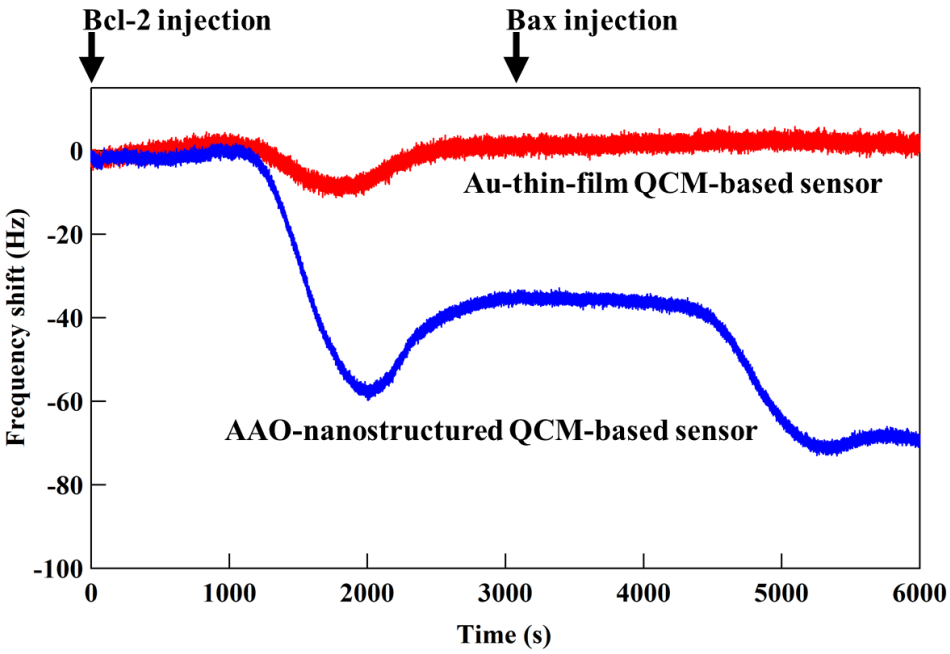

Fig.4-9 Time-dependent frequency shifts corresponding to Bcl-2 and Bax injection. Gray and black lines represent the Au-thin-film and the AAO-nanostructured QCM-based sensors, respectively.

4.11 Continuous measurement of Bcl-2 and Bax interaction with several concentrations

The limit of detection (LOD) was evaluated for both interaction: anti-Bcl-2 and Bcl-2 interaction, and Bcl-2 and Bax interaction. Fig. 4-10 shows the time-dependent frequency shift after the injection of Bcl-2 (2 μg/mL), subsequently injection of some concentrations of Bax (from 0.5 to 10 μg/mL) in sequence. Here, arrows in the figure show the injection samples. As a result, the sensor detected the interaction as shown the frequency shift on the Bax concentration of 0.5 μg/mL. In addition, the absolute frequency shift increased with the Bax concentration. Analytical curves of anti-Bcl-2 and Bcl-2 interaction, and Bcl-2 and Bax was shown in Fig. 4-11, and 12, respectively. LODs on the condition of S/N=3 for Bcl-2 and Bax were calculated as 0.57 μg/mL and 0.55 μg/mL,

respectively. If it is possible to reduce the noise level (0.6 Hz) of the detection system, LOD will be improved. As a result, the AAO-nanostructured QCM-based sensor detected the frequency shifts corresponding to the PPIs.

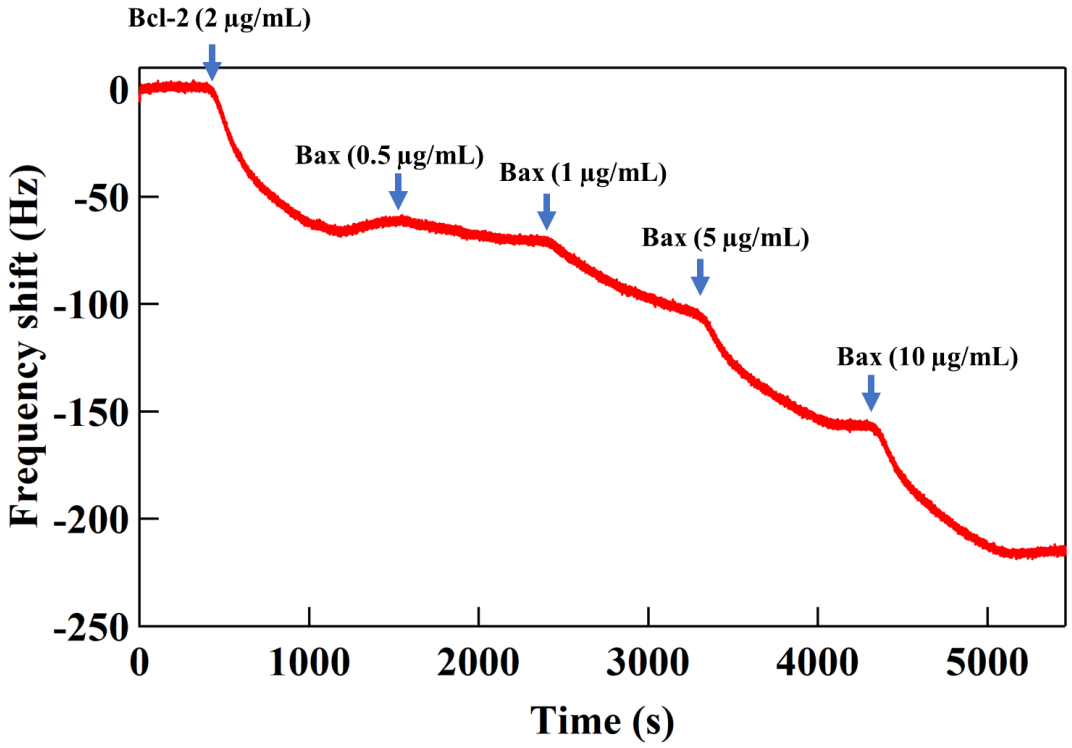

Fig. 4-10 Time-dependent frequency shift after the injection of Bcl-2 (2 µg/mL), subsequently injection of some concentrations of Bax (0.5, 1.0, 5.0, and 10 µg/mL) in sequence.

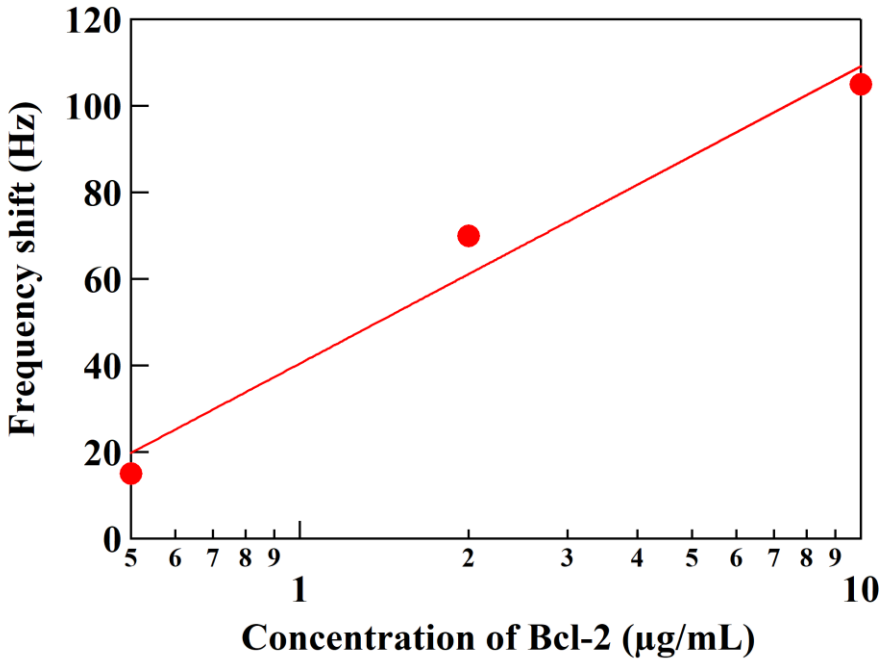

Fig. 4-11 Analytical curve of anti Bcl-2 and Bcl-2 interaction.

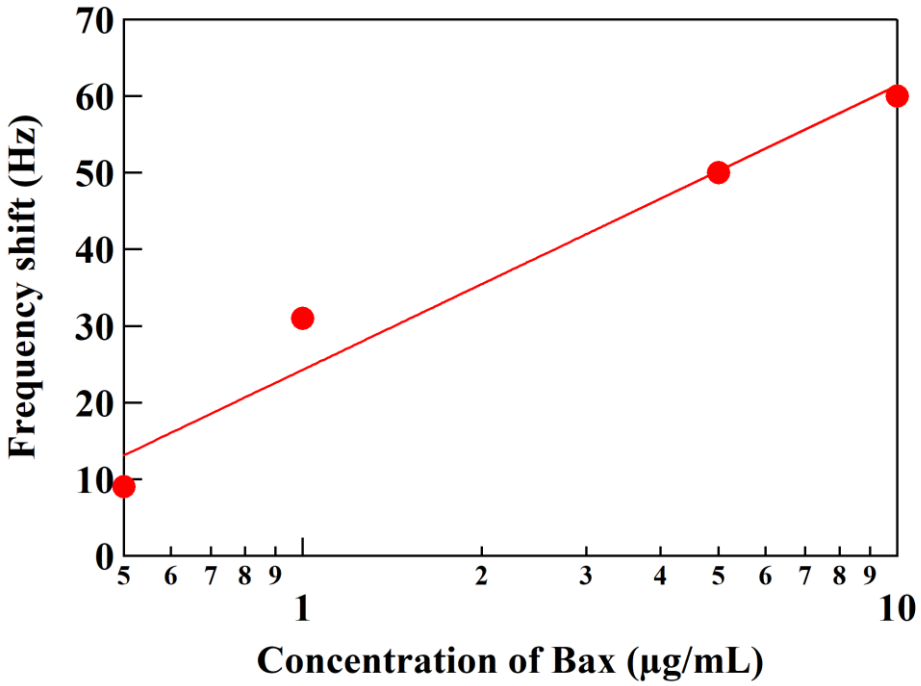

Fig. 4-12 Analytical curve of Bcl-2 and Bax interaction. Here, the concentration of Bcl-2 was set as 2 μg/mL.

4.12 Evaluation of the dissociation rate constant based on the frequency shift by the AAO-nanostructured QCM-based sensor

The dissociation rate constant of IgG was evaluated from the frequency shifts as shown in Fig. 4-7. Fig. 4-13 shows the normalized concentration of mouse IgG for the frequency shift depended on the mouse IgG concentration which was calculated using the following equation [4-21, 4-22].

$$\frac{\boldsymbol{T}}{\boldsymbol{\Delta m}} = \frac{\boldsymbol{T}}{\boldsymbol{\Delta m_{max}}} + \frac{\boldsymbol{K_d}}{\boldsymbol{\Delta m_{max}}} \quad \cdot\cdot\cdot (\mathbf{4.1})$$

where, T, Δm, Δm_{max}, Kd are target concentration (nM), the mass change per unit area of an electrode in the measurement (ng/cm^2), the maximum mass change per unit area of an electrode in the measurement (ng/cm^2), and the dissociation rate constant of the interaction (nM), respectively. The sensitivity of 1.18 ng/Hz was adopted to calculate the mass changes. Dissociation rate constants on AAO nanostructured and Au-thin-film QCM-based sensors were calculated as 5.68, and 9.84 nM, respectively. As the results, the dissociation rate constants on AAO nanostructured was improved. There are two reasons to understand the increase in the dissociation rate. First is an increase in the probability of the interaction due to a large amount of antibody on the AAO surface [4-14]. Second is a localization of ion or molecular inside the nanopore by restricting their diffusion into a bulk buffer solution [4-23]. These reasons increased the quantity of weak antigen-antibody interaction, then, the dissociation rate was improved. Therefore, the AAO-nanostructured QCM-based sensor could catch the weak interaction with the improved dissociation rate constant.

Fig. 4-14 shows the normalized concentration of Bax for the frequency shift depended on the Bax concentration. The dissociation rate constant was calculated as 53.5

nM, based on the equation (4.1). All proteins belonging to the Bcl-2 family have the Bcl-2 Homology (BH) domain, and four different BH domains are known as BH1, BH2, BH3, and BH4. Bcl-2/Bax heterodimer formation consists of a tail-to-tail interaction that requires the central region of Bax, including the Bcl-2, BH1, BH2, BH3, and BH3 domains [4-24]. The affinity of the heterodimer formation depended on the length of the BH3 domain. Kale et al. [4-25] reported that the dissociation-rate in this study was expected as 28 peptide length of BH3 in the Bax protein which contributed to associate with the Bcl-2. The flowing buffer solution dissociated the Bax that associated weakly with the Bcl-2, as shown in the increased frequency shift after the PPIs on the Au-thin-film QCM-based sensor. However, on the AAO-nanostructured QCM-based sensor, the frequency shift maintained a significant change. Accorded to the above reason, the AAO-nanostructured QCM-based sensor detected the Bcl-2/Bax interaction with low association rate by its large surface area and the restriction of their diffusion.

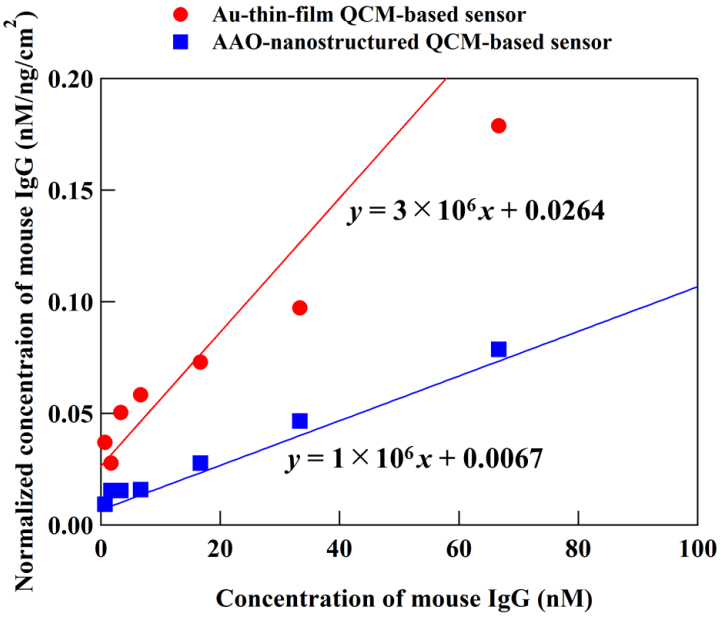

Fig. 4-13 Analysis of the dissociation rate constant calculated using the results on anti-mouse IgG and IgG interaction.

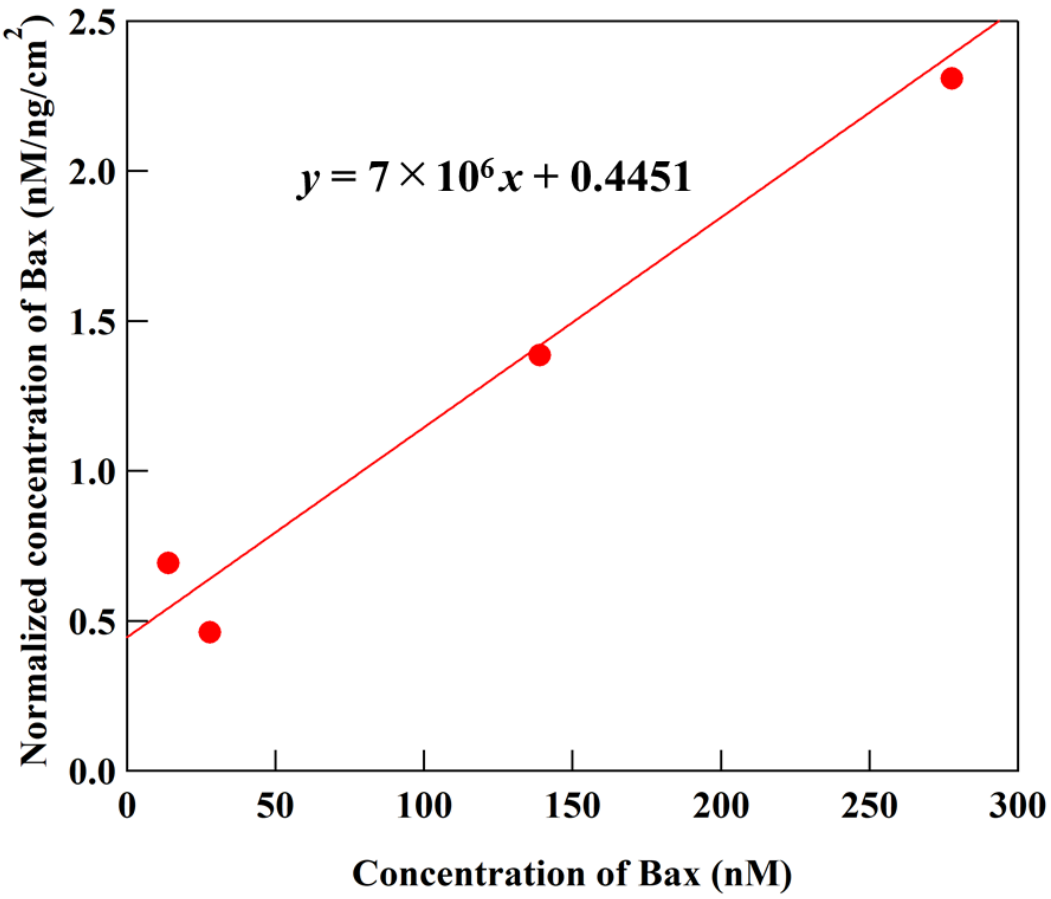

Fig. 4-14 Analysis of the dissociation rate constant of the Bcl-2 and Bax interaction. Bcl-2 concentration immobilized on the surface of AAO nanostructure was 2 μg/mL.

4.13 Conclusions

AAO nanostructure was fabricated on the electrode of a QCM-based sensor to improve the sensitivity by enlarging the adsorption surface area. The thickness of the AAO nanostructure was approximately 200, 400, 700, and 1000 nm. The nanohole diameter was approximately 40, 60, and 80 nm. The pitch at each nanohole was 100 nm. From the conductance peak analysis, the mass sensitivity improved by the fabrication of AAO nanostructure on the quartz. Additionally, the large dimension of AAO nanostructure influenced on the resonant resistance in the buffer solution. In the QCM

measurement for the antibody-antigen reaction, the obtained frequency shifts depended on the dimension of AAO nanostructure. These results indicated that the frequency shift increased owing to the increase in the surface area of the AAO nanostructure. In the case of the AAO-nanostructured QCM-based sensor, the detection limit improved on comparison of calibration curves for detection of anti-mouse IgG and IgG interaction. In addition, the AAO-nanostructured QCM-based sensor applied to assess PPIs between anti-Bcl-2 and Bcl-2 and between Bcl-2 and Bax. Comparing to the Au-thin-film QCM-based sensor, the AAO-nanostructured QCM-based sensor detected accurately all reaction that was not detectable for the Au-thin-film QCM-based sensor. AAO nanostructure improved the sensing performance of QCM-based sensor by its large surface area which supported to immobilize large amount of antibody. Additionally, the AAO-nanostructured QCM-based sensor enabled to evaluate the dissociation-rate constant of the weak interaction due to its improved sensing performance. In the evaluation of the antigen-antibody interaction, the constant was dissociation-rate improved from 9.84 to 5.68 nM. The length of BH3 domain in the Bcl2-Bax interaction was estimated from its dissociation rate of 53.5 nM. The results in this chapter showed the high performance of the AAO-nanostructured QCM-based sensor that enabled to detect biomaterials interaction with large signal, large dynamic range, high sensitivity, and evaluable dissociation rate.

References

4−1	K. V. Horoshenkov, A Review Of Acoustical Methods For Porous Material Characterisation. J. Sound Vib., 2017 22, 92-103.
4-2	H. Du, J. Li, J. Zhang, G. Su, X. Li, and Y. Zhao, Separation of Hydrogen and Nitrogen Gases with Porous Graphene Membrane. J. Phys. Chem., 2011 11, 23261-23266.
4-3	K. Rezwana, Q. Z. Chena, J. J. Blakera, and A. R. Boccaccini, Biodegradable and bioactive porous polymer/inorganic composite scaffolds for bone tissue engineering. Biomaterials., 2006, 27 3413-3431.
4-4	K. Kurumada, T. Kitamura, N. Fukumoto, M. Oshima, M, Tanigaki, and S. Kanazawa, Structure generation in PTFE porous membranes induced by the uniaxial and biaxial stretching operations. J. Membrane Sci., 1998 149, 51-57.
4-5	T. Hashimoto, M. Itakura, and H. Hasegawa, Late stage spinodal decomposition of a binary polymer mixture. I. Critical test of dynamical scaling on scattering function. J. Chem. Phys., 1986 85, 6118-6128.
4-6	K. Nakanishi, Pore Structure Control of Silica Gels Based on Phase Separation. J. Porous Mater., 1997 4, 67-112.
4-7	P. Hoyer, K. Nishio, and H. Masuda, Preparation of regularly structured porous metal membranes with two different hole diameters at the two sides, Thin Solid Films, 1996 286, 88-91.
4-8	M. Sera, R. Matsumoto, and N. Miyazaki, Tensile Deformation Analyses of a Gold Nanowire Using Molecular Dynamics and Parallel Replica Method. Transactions of JSCES, Paper No. 20120008
4-9	S. Shingubara, S. Maruo, T. Yamashita, M. Nakao, and T. Shimizu, Reduction of pitch of nanohole array by self-organizing anodic oxidation after nanoimprinting. Microelectron. Eng., 2010 87, 1451-1454.
4-10	E. J. Sin, Y. S. Moon, J. O. Lim, J. S. Huh, S. Y. Choi, and Y. S. Sohn, Surface modification of aluminum oxide for biosensing application. Biomed. Eng. Appl. Basis Commun., 2012 24, 111-116.
4-11	J. Zhu, S. Huang, J. Ye, X. Zhang, and G. Liu, Design of a quartz crystal with transparent electrode used for both QCM-D and LSPR technology. Sens. Actu. A, 2015 229, 141-146.

4-12	A. A. Feiler, A. Sahlholm, T. Sandberg, and K. D. Caldwell, Adsorption and viscoelastic properties of fractionated mucin (BSM) and bovine serum albumin (BSA) studied with quartz crystal microbalance (QCM-D). J. Coll. Interf. Sci., 2007 315, 475-481.
4-13	N. Asai, H. Terasawa, T. Shimizu, S. Shingubara, and T. Ito, Highly sensitive quartz crystal microbalance based biosensor using Au dendrite structure. Jpn. J. Appl. Phys., 2017 57, 02CD01.
4-14	T. Orita, M. Tomita, M. Harada, and K. Kato, Binding activity of avidin to the biotin within mesoporous silica materials for bioanalytical applications. Anal. Biochemi., 2012 425, 1-9.
4-15	Z. Lin, and M. D. Ward, The Role of Longitudinal Waves in Quartz Crystal Microbalance Applications in Liquids. Anal. Chem., 1995 67, 685-693.
4-16	M. H. Kang, and C. P. Reynolds, Bcl-2 inhibitors: targeting mitochondrial pathways in cancer therapy. Clin. Cancer Res., 2009 15, 1126-1132.
4-17	J. Chen, H. Zhou, A. Aguilar, L. Liu, L. Bai, D. McEachern, C. –Y. Yang, J. L. Meagher, J. A. Stuckey, and S. Wang, Structure-based discovery of BM-957 as a potent small-molecule inhibitor of Bcl-2 and Bcl-xL capable of achieving complete tumor regression. J. Med. Chem., 2012 55, 8502-8514.
4-18	F. A. C. G. Sousa, T. C. Paradella, Y. R. Carvalho, and L. E. B. Rosa, Comparative analysis of the expression of proliferating cell nuclear antigen, p53, bax, and bcl-2 in oral lichen planus and oral squamous cell carcinoma. Ann. Diagn. Pathol., 2009 13, 308-312.
4-19	J.-F. Li, S.-J. Zheng, L.-L. Wang, S. Liu, F. Ren, Y. Chen, L. Bai, M. Liu, and Z.-P. Duan, Glucosylceramide synthase regulates the proliferation and apoptosis of liver cells in vitro by Bcl-2/Bax pathway. Mol. Med. Rep., 2017 16, 7355- 7360.
4-20	M. Kim, S. O. Jung, K. Park, E. J. Jeong, H.-A. Joung, T-H. Kim, D-W. Seol, and B. H. Chung, Detection of Bax protein conformational change using a surface plasmon resonant imaging-based antibody chip. Biochem. Biophys. Res. Commun., 2005 338, 1834-1838.
4-21	Y. Zhang, V. Telyatnikov, M. Sathe, X. Zeng, and P. G. Wang, Studying interaction of α-gal carbohydrate antigen and proteins by quartz-crystal microbalance. J. Am. Chem. Soc., 2003 125, 9292-9293.
4-22	Y. Ebara, K. Itakura, and Y. Okahata, Kinetic studies of molecular recognition based on hydrogenbonding at the air-water interface by using a high sensitive quartz-crystal microbalance. Langmuir, 1996 12, 165-5170.
4-23	Y. Nakasaka, T. Tago, K. Yano, and T. Masuda, Diffusion Mechanisms within Microporous and Mesoporous Materials in Gas and Liquid Phases. Membrane, 2007 32, 332-339.

4-24	M. Sattler, H. Liang, D. Nettesheim, R. P. Meadows, J. E. Harlan, M. Eberstadt, H. S. Yoon, S. B. Shuker, B. S. Chang, A. J. Minn, C. B. Thompson, and S. W. Fesik, Structure of Bcl-xL-Bak Peptide Complex: Recognition Between Regulators of Apoptosis. Science, 1997 275, 983–986.
4-25	J. Kale, E. J. Osterlund, and D. W. Andrews, BCL-2 family proteins: changing partners in the dance towards death. Cell Death Differ., 2018 25, 65-80.

Chapter 5: DNA origami nanostructures with aptamer as recognition elements to improve a sensitivity on QCM-based sensor

5.1 Brief introduction of aptamer-attached DNA origami

The large surface area of nanostructure on a transducer allowed a biosensor to capture many target analytes and increase the sensing performances [5-1]. A dry-process with top-down and bottom-up methods has fabricated nanostructures with controllable dimensions on the transducers [5-2]. However, the throughput of the process is quite low due to the requirements of a vacuum system, numerous etching-deposition processes, a drawing process of a mask pattern and so on. In contract, a wet-process with self-assembling formation has allowed to form conveniently 3D nanostructures on the transducer with centimeter-scale [5-3]. However, the control of the dimensions depends on ions or molecular diffusion in a liquid phase. A slight difference at a formation condition causes the variation of dimension on nanostructure.

One of other approaches to improve the sensing performances is the development of recognition elements with good affinity, high selectivity, and high stability. Recently, the recognizing function of DNA has drawn attentions of scientists to form self-assembled nanostructure [5-4]. DNA has excellent properties, such as molecular assembly by its base sequence and periodicity of double helix structure. These features enabled DNA nanostructure with densely integrated aptamers [5-5, 5-6]. However, the most studies employed several complicated *in situ* processes to enhance the sensing signal in a biosensor using DNA nanostructure. For an example of such studies, Zhao et al. used dendric DNA nanostructure to detect p53 gene as target analyte [5-7]. Specific aptamers against p53 genes were firstly immobilized on an electrode surface of QCM-based sensor.

After hybridizing p53 genes with the aptamers, complementary DNA structure with blanches were additionally hybridized with the aptamer as the basis of next amplification. Finally, second aptamers were additionally hybridized with the DNA structure to capture other p53 genes. By repeating these processes, dendric DNA nanostructure was assembled to amplify exponentially the sensing signal. However, that repeating process was too complicated for the end-user to obtain the amplified signal. Additionally, their strategy led to overestimate the detected concentration or dissociation rate of analyte by detecting a whole structure.

In 2016, Godonoga et al. assembled a DNA origami with specific aptamers to malaria biomarkers [5-8]. DNA origami was assembled from one long-stranded DNA (scaffold DNA) and numerous short-stranded DNAs (staple DNAs). The self-assembly formation allowed to control the size and shape of DNA origami according to an initial design. In addition, replacement the short-stranded DNA with aptamer endowed the DNA origami with specificity to target analyte. From these features, aptamer-attached DNA origami achieved stability and homogeneity to capture malaria biomarker in human blood plasma. Coating DNA origami on the sensor surface in advance could substitute the above complicated amplifying process that employed to form dendric DNA nanostructure. However, there is a question how aptamers on DNA origami affects its affinity with an analyte since the number of aptamers can be arranged from 0 to around 200.

In this chapter, aptamer-attached DNA origami was employed as recognition elements of a QCM-based sensor. For biosensing application, the DNA origami should be immobilized onto a gold electrode surface of the QCM-based sensor. Therefore, thiol modified DNA was used as anchor of DNA origami. DNA origami were assembled with flexible anchoring or adhesive anchoring extensions. Two types of anchoring extensions

were extended from 3’ or 5’ of staple strands, respectively. The anchoring extensions were optimized by a comparison in frequency shifts of hybridized DNA origami. Two assembling methods were demonstrated to assemble aptamer-attached DNA origami with several aptamers ranged from 0 to 166. An aptamer-protein interaction was examined by QCM measurement to optimize the density of aptamers on DNA origami. The frequency shifts at several concentrations of target protein (alpha fetoprotein, AFP) were measured to compare the sensing performances on two kinds of QCM-based sensors using aptamer-attached DNA origami or directly-modified aptamer.

5.2 Experimental details

M13mp18 single stranded DNA was purchased and all 226 staple strands were purchased from Integrated DNA technologies Int., USA. Tris(hydroxymethyl)aminomethane, ethylenediaminetetraacetic acid (EDTA), magnesium chloride, potassium chloride, 1/15 mol phosphate powder, glacial acetic acid, polyethylene glycol (molecular weight: 8000, PEG8000), tris(2-carboxyethyl)phosphine Hydrochloride (TCEP-HCl) was purchased from FUJIFILM Wako Pure Chemical Corp. Agarose powder for electrophoresis was purchased from VWR Life Science. 6-Mercapto-1-hexanol (MCH) was purchased from Sigma Aldrich. All other reagents were consisted of guaranteed grade and used without any further purification. All solutions were prepared with ultrapure water of 18MΩ cm purified from a Milli-Q purification system (Milli-Pore, Bedford, MA, USA).

The sequences of other ssDNA with lyophilized form and the providers were represented following Table 5-1. The sequence of AFP-specific ssDNA aptamer was

referred from a paper of a developer [5-9].

Table 5-1 Sequences of ssDNA used in this study

Name	Sequences 5' to 3'	Provider
Extended AFP-specific ssDNA aptamers	GGAAGTTGATATGGTTGATGACTCG TGACGCTCCTAACGCTGACTCAGGT GCAGTTCTCGACTCGGTCTTGATGT GGGTCCTGTCCGTCCGAACCAATC	Sigma Aldrich
Thiol modified AFP-specific ssDNA aptamers	[ThiC6]- GTGACGCTCCTAACGCTGACTCAGG TGCAGTTCTCGACTCGGTCTTGATG TGGGTCCTGTCCGTCCGAACCAATC	Biomers.net
Thiol modified anchoring DNA	[ThiC6]- CGTGAGGTGTGGTAGATGATGTG	Biomers.net

QCM-based sensor (QA-A9M-AU(M)(SEP), SEIKO EG&G) had the Au electrode on both sides of quartz as the electrode diameter of 5 mm and thickness of 300 nm. The fundamental frequency of the standard QCM-based sensor was 9 MHz. A QCM analyzer (QCM 922A, Seiko EG&G) scanned resonance frequency with overtone (N=3) from 26.8 MHz to 26.9 MHz. QCM-based sensor combined with a measurement cell, which connected to a flow injection system. The measurement cell had a circle-shaped flow path, an inlet, and an outlet made of poly(dimethylsiloxane) (PDMS). The depth and diameter of the flow path were 1 and 5.5 mm, respectively. The QCM-based sensor and the measurement cell placed at the constant-temperature chamber to maintain the room temperature. A syringe pump controlled a flow rate of 10 µL/min. A volume of loading

sample was 100 µL. A buffer containing phosphate + 200 mM NaCl at pH = 7.4 was the carrier buffer to transport the injected sample. This buffer solution was flowed continuously at 10 µL/min by the flow injection system.

An admittance measurement analyzed resonance characteristics of QCM-based sensors with aptamer-attached DNA origami or thiol modified aptamer. The measurement was performed in each modification steps of the sensor surface. In this study, thiol modified anchoring DNA or thiol modified aptamer were reduced with 20 mM of TCEP/HCl for 30 min. 100 µL of sample solution containing 100 nM of thiol modified anchoring DNA was loaded on the sensor surface. The thiol modified anchoring DNA was immobilized on the gold electrode surface of the sensor via thiol linkage. After rinsing the sensor surface by the buffer solution, 100 µL of sample solution containing 2 nM of aptamer-attached DNA origami was loaded as dropwise on the sensor surface. Finally, aptamer-attached DNA origami was hybridized to the complementary thiol modified anchoring DNA, and then anchored onto the electrode surface. For directly-aptamer-modified QCM-based sensor, 100 µL of sample solution containing 100 nM of thiol modified aptamer was loaded on the sensor surface. After rinsing the sensor by the buffer solution, 75 µL of MCH with 10 mM passivated the sensor surface by incubation for 30 min. The analysis of both resonance characteristics was performed in air phase to estimate the mass changes of thiol modified anchoring DNA, DNA origami, thiol modified aptamer, and MCH modifications.

DNA origami was designed by CaDNAno [5-10], which is an open-source software package with a graphical user interface. In the design, DNA origami folds onto a 1-layers sheet of size ~70 nm×90 nm×2 nm. Eight extended staples with 24-nucleotides were located at the edge of DNA origami. Each extended staple aimed to hybridize the

thiol modified anchoring DNA on an electrode surface. The DNA origami had several supporting staples evenly and symmetrically at its body. The length and number of supporting staples were 24-nucleotides and 0-166, respectively. According to the location of supporting staples, aptamers with extension sequences were hybridized to the staples and evenly located at the DNA origami.

A rectangular-shaped DNA origami (~70 × 90 nm) was assembled from 7249 bases M13mp18 single-stranded scaffold strand and 226 staple strands in a buffer solution containing 1× TAE/Mg^{2+} (40 mM Tris, 20 mM acetic acid, 2.5 mM EDTA, 12.5 mM magnesium chloride, pH 8). The staple strands and aptamers endowed complementary extended sequence to hybridize each other. The concentrations of these DNA strands were 12 nM of M13 scaffold, a fivefold molar excess of staples and a tenfold molar excess of aptamer. DNA mixtures were annealed using a PCR machine (BioRad DNA Engine) at the following settings: for the one-pot assembly and 1st annealing: 80 °C for 10 min, with a subsequent temperature decrease from 80 °C at 1 °C/5 min until 65 °C, 1 °C/30 min until 45 °C, and 1 °C/15 min until 25 °C. The concentration was determined by UV-Vis absorption spectroscopy (Nanodrop, Sigma Aldrich).

Assembled aptamer-attached DNA origami was separated from excess of unmodified staple strands by a purification using a buffer solution containing 15 v/v% PEG8000, 5 mM magnesium chloride, 5 mM tris(hydroxymethyl)aminomethane, 505 mM potassium chloride, and 1 mM EDTA. A precipitation buffer solution was mixed with sample in 1.5 mL tube at same volume and incubated for 5 min at room temperature. The mixture was spin down at 13,400 rpm by a table-top centrifugal machine. A supernatant was removed from the tube by pipet. The sample tablet including DNA origami was remained on the bottom of the tube. The tablet was resuspended in 1×

TAE/Mg^{2+} buffer by adding initial sample volume. The resuspended DNA origami sample was incubated at 37 ℃ and vortexed at 1000 rpm for 10 min to eliminate aggregation of each DNA origami.

1 wt% agarose gel was prepared from agarose powder and 1× TAE/Mg^{2+} buffer. 10 μL of sample solution with 4 nM was loaded for analysis in each lane and 100 V of potential was applied to chamber of electrophoresis at 4 °C for 2 hours. The gels were subsequently stained with SYBR Gold for 25 min and visualized on a UVP Benchtop (2UV Transilluminator) at 302 nm. In the electrophoresis, a running buffer was 1× TAE/Mg^{2+} buffer.

DNA origamis were imaged by AFM (Bruker, Dimension XR). Subsequent to annealing and incubation, an aliquot (1–2 μ L) of sample was deposited onto the surface of a freshly cleaved mica, followed by the addition of 50 μL of TAE/Mg^{2+} buffer. Samples were imaged using a micro cantilever with spring constant at a scan rate of 1.95 Hz in peak force tapping mode in fluid.

5.3 Design of aptamer attached to DNA origami

Three types of DNA origamis with eight anchoring extensions were designed to be immobilized onto the gold electrode via thiol modified anchoring DNA. Fig. 5-1 showed schematic images of three DNA origamis with anchoring extensions. One of the DNA origami was not modified with extension (DNA origami without anchoring extensions). The second and third DNA origamis were modified with the flexible and adhesive anchoring extensions at the 3’ or 5’ end of staple DNA. DNA origamis with anchoring extensions were assembled by mixing M13 scaffold and 226 staple strands,

annealing them at 80 ℃ for 10 min and cooling down -1 ℃/min from 80 to 25 ℃ (in total an hour). After purification of DNA origamis, agarose gel electrophoresis (AGE) confirmed the assembly of DNA origamis with anchoring extensions. In Fig. 5-2 (a), lanes 2, 3, and 4 showed three DNA origami samples with no, flexible, and adhesive anchoring extension, respectively. These bands, which indicated DNA origami samples, shifted to upper position comparing to the control line 1 (M13 scaffold). The slower mobility of DNA origami resulted from planar-shape nanostructure formation. The excess of staple strands was not confirmed under main bands in lines 2, 3, and 4. Purification succeeded to remove the excess of staple strands from sample solution. Atomic force microscopy proved that DNA origamis form a rectangle shape with 64 ×90 nm, according to our design, as shown in Fig. 5-2 (b). The yield of well-formed DNA origami was over 90 %.

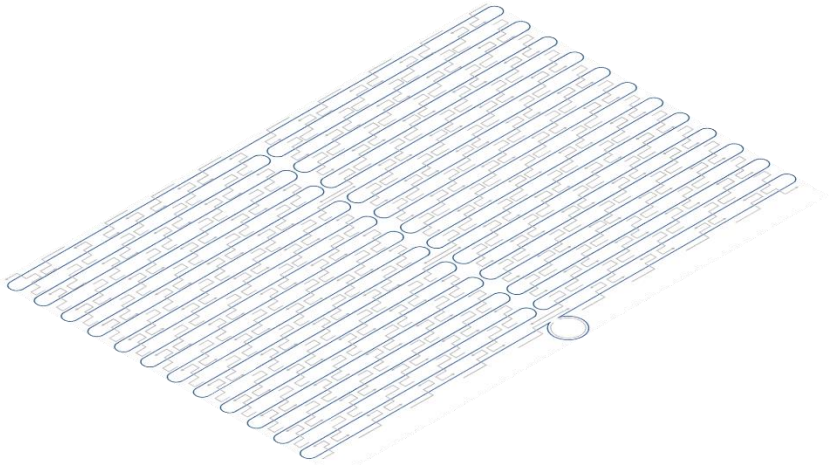

DNA origami without anchoring extensions

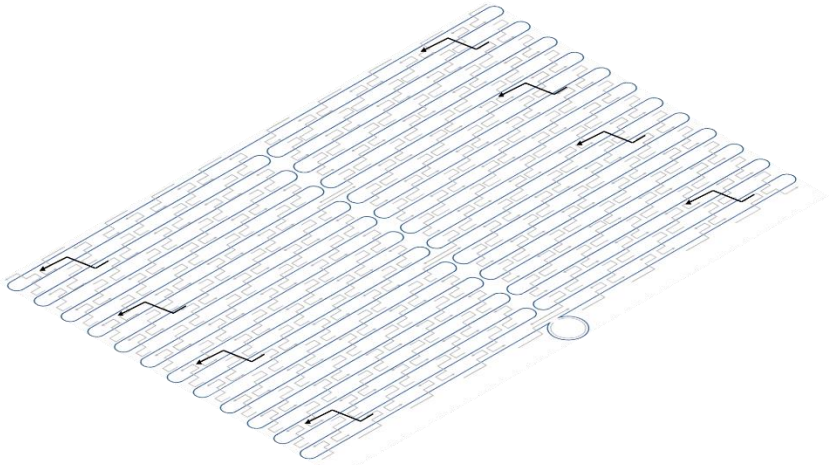

DNA origami with flexible anchoring extensions

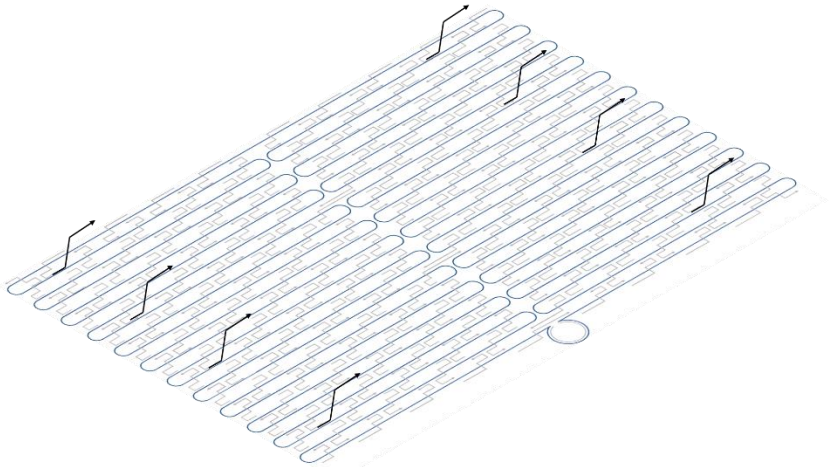

DNA origami with adhesive anchoring extensions

Fig. 5-1. Schematic images of three DNA origamis with anchoring extension

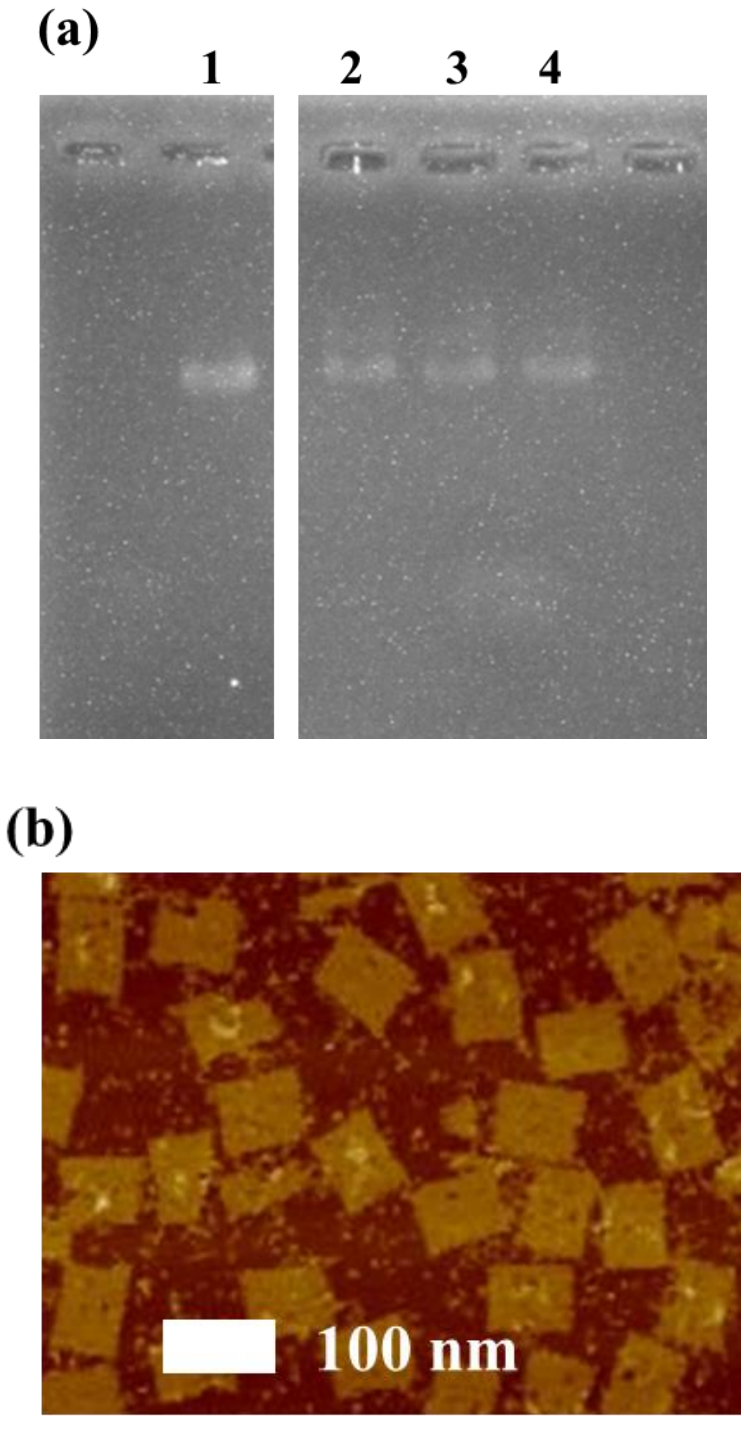

Fig. 5-2. (a) AGE image of the mobilities of three DNA origamis with anchoring extensions. Samples were loaded from left side following; M13 scaffold (line 1), three DNA origamis with no (line 2), flexible (line 3), and adhesive (line 4) anchoring extensions, and (b) AFM image of DNA origami with flexible anchoring extensions.

5.4 Determination of anchoring extension in DNA origami to be immobilized onto a gold electrode

QCM measurement was performed to demonstrate immobilization of all DNA origamis with anchoring extensions onto the electrode surface of a QCM-based sensor. Thiol modified anchoring DNA was coated on the gold electrode in advance as an anchor for the DNA origamis. DNA origamis with anchoring extensions could be hybridized with the thiol modified anchoring DNA. Frequency shifts on the hybridization were compared to determine which DNA origami with anchoring extensions are suitable for aptamer-protein interaction. In this experiment, 1×TAE/Mg2+ buffer solution was flowed to carrier a sample solution into a measurement cell. Fig. 5-3 showed results of QCM measurement for anchoring of DNA origami by hybridization. After loading DNA origamis with anchoring extensions, the frequency shifts were generated from hybridization between DNA origami and thiol modified anchoring DNA on the electrode surface. The excess of DNA origami dissociated from the sensor surface after flowing the sample solution. Flexible anchoring extensions allowed DNA origami to hybridize with thiol modified anchoring DNA with the most massive frequency shift. However, DNA origami with no anchoring extensions also bound significantly on the electrode surface, as shown in a red line. This shift indicated non-specific absorption between thiol modified anchoring DNA and DNA origami. One possibility of the non-specific absorption was considered as that magnesium cross-linkages was built between the anchoring DNA and the DNA origami. Continuous loading of DNA origamis with 0.2 nM generated further the frequency shift only by DNA origami with flexible anchoring extensions. This additional shift indicated that DNA origami with flexible anchoring extensions was bound

in large quantity with thiol modified anchoring DNA on the electrode surface. These results showed that DNA origami with flexible anchoring extensions would be suitable for the detection of aptamer-protein interaction.

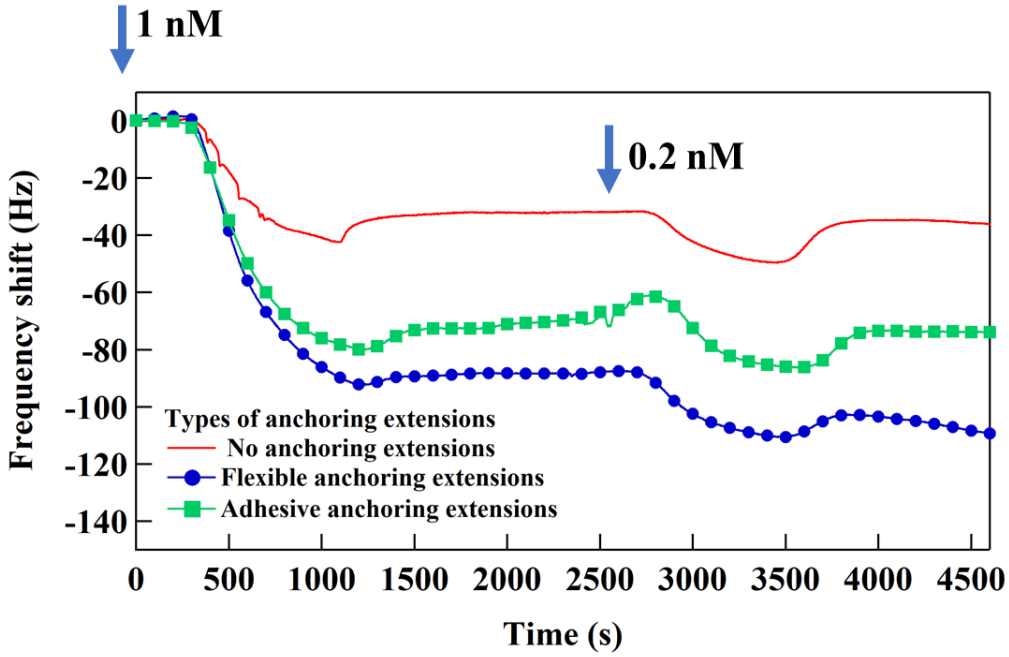

Fig. 5-3 Frequency shifts on hybridization between DNA origamis with several anchoring extensions and thiol modified anchoring DNA on the sensor electrode.

5.5 Comparison of two assembling methods for aptamer-attached DNA origami

Two assembling methods were demonstrated to assemble DNA origami with aptamer. DNA origami and aptamer had the extended oligos, called supporting extensions, with complementary sequences to hybridize each other. The design of DNA origami is showed in Fig. 5-4. In the design, aptamers located evenly at DNA origami, and its numbers were ranging from 0 ,36, 72, 108, 138, to 166. The positions of aptamers on DNA origami corresponded to Block number in the design. For examples, Block 1

indicated 36 aptamer-attached DNA origami. Similarly, Block 1+ 2 indicated 72 aptamer-attached DNA origami. In the case of 166 aptamer-attached DNA origami, the positions of aptamer were indicated by Block 1 - 5.

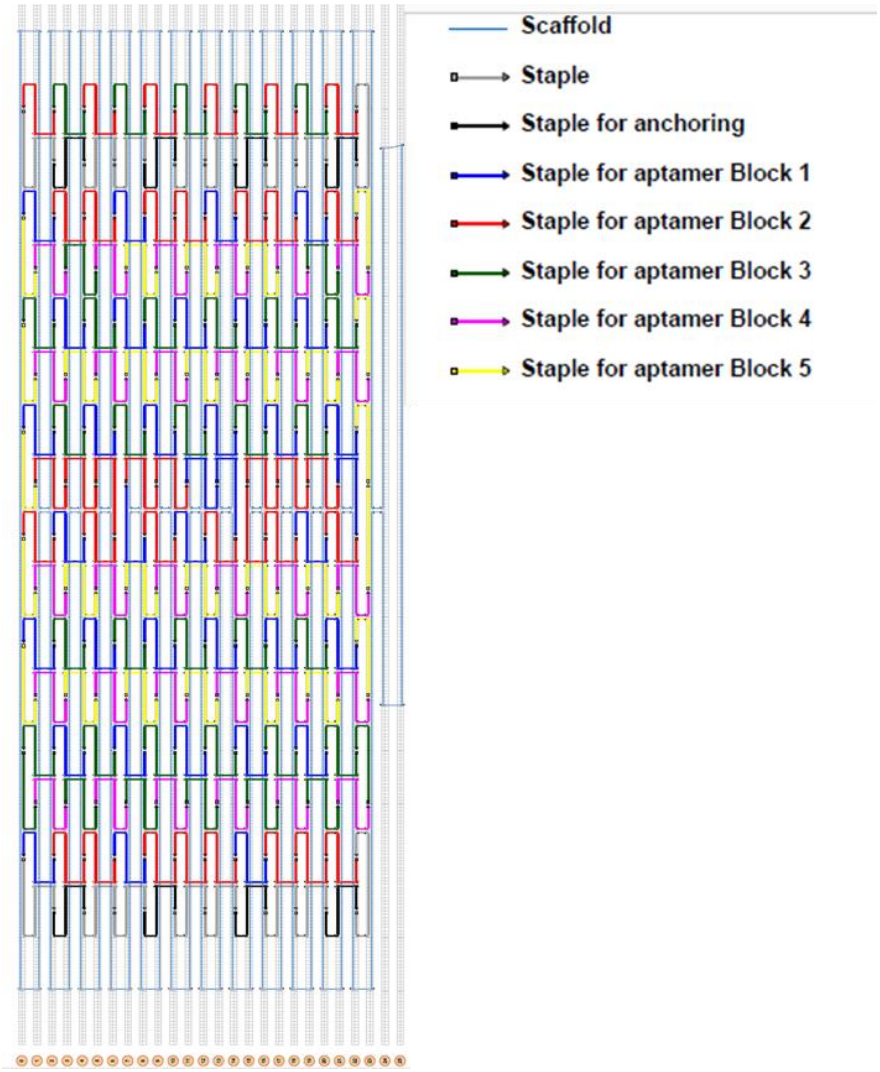

Fig. 5-4 Design of positions of aptamers on DNA origami. Each position of aptamers was indicated by colored symbols corresponding to Block number. Block 1 means 36 aptamers on DNA origami. Block 1+ 2 mean 72 aptamers on DNA origami.

On the method 1 (called 2-step annealing), aptamer-attached DNA origami was assembled by post-annealing of a mixture containing pre-assembled DNA origami and aptamers. The temperatures of annealing were 25, 42, 47, 53, 60, 70, and 80 ℃. On the method 2 (called one-pot annealing), aptamer-attached DNA origami was assembled by one-time annealing of the sample solution including M13 scaffold, staple strands, extending strands and several amounts of aptamers.

Fig. 5-5 (a) showed AGE image of 72-aptamer-attached DNA origami by 2-step annealing. The bands in line 3, 4, 5, and 6 shifted to upper position comparing to a band of DNA origami in line 2. The assembly of aptamer-attached DNA origami succeeded by annealing at 25, 42, 47, and 53 ℃. However, shifting downward of the bands in line 7, 8, and 9 was observed in the samples annealed at 60, 70, and 80 ℃. In AFM images of Fig. 5-5 (b), aptamer-attached DNA origami, which was annealed at 25 ℃, maintained its conformation. In constant, the partial disassembly of DNA origami was observed in a sample annealed at 53 ℃. DNA origami was collapsed entirely in the sample annealed at 80 ℃. Annealing at high temperature promoted to disassemble staple strands from M13 scaffold, as shown in AGE and AFM images.

Fig. 5-6 (a) showed several mobilities of aptamer-attached DNA origamis by one-pot annealing. The aptamer-attached DNA origamis were assembled with several aptamers ranged from 0 to 166. The bands shifted to the upper position according to the increasing amounts of added aptamers. Attachment of aptamers at DNA origami increased its molecular weight, and then the mobility of aptamer-attached DNA origami was decreased. AFM image in Fig. 5-6 (b) also showed well-formed 72 aptamer-attached DNA origami without missing parts. These results showed that the one-pot assembly was successful for formation of aptamer-attached DNA origami.

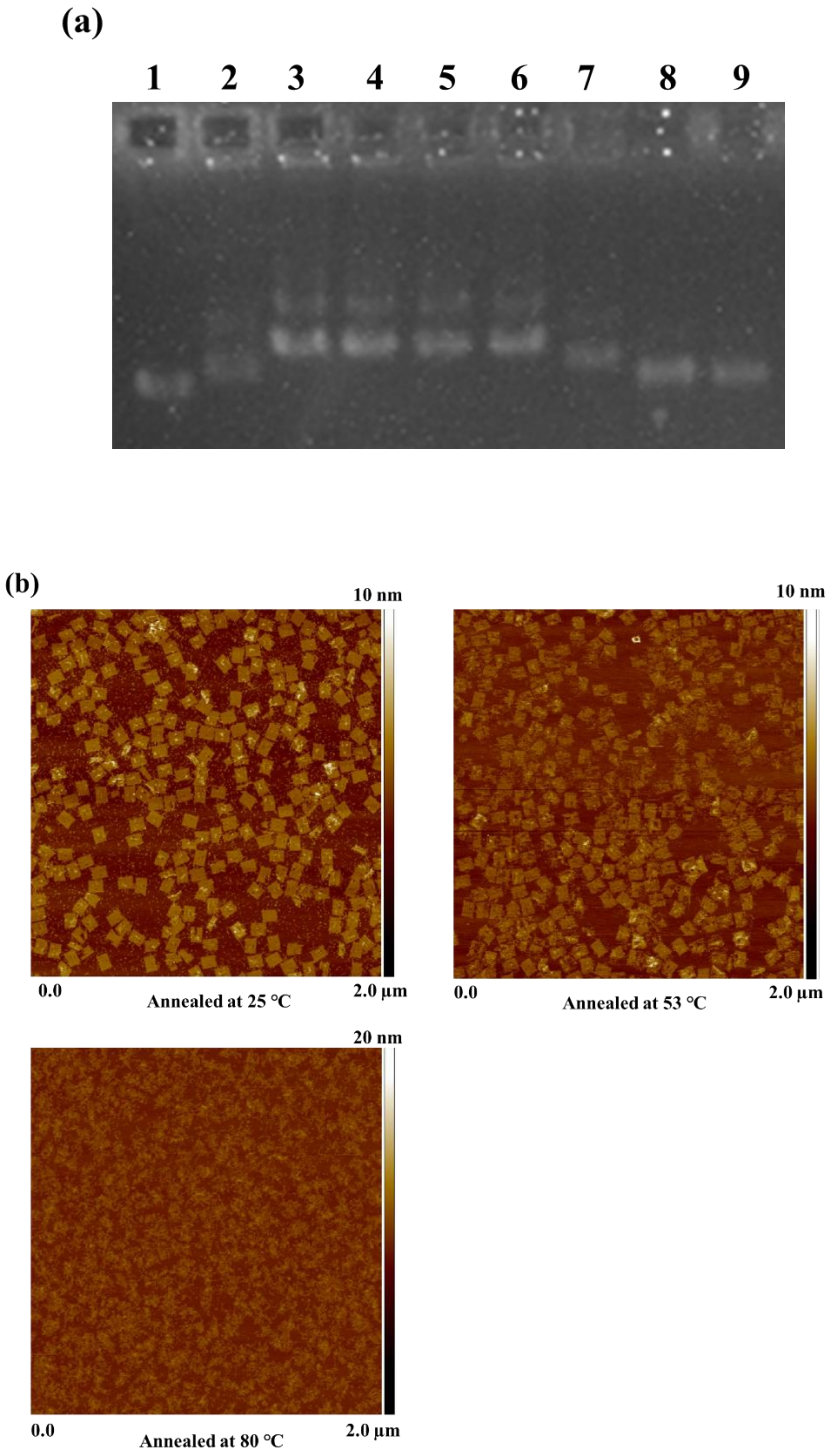

Fig. 5-5 (a) AGE image of aptamer-attached DNA origami assemble by two-step annealing at 25, 40, 47, 53, 60, 70, and 80 ℃. A sample following below was loaded in each line from left side: M13 scaffold (line1), DNA origami (line2), annealed at 25 ℃ (line3), 40 ℃ (line4), 47 ℃ (line 5), 53 ℃ (line 6), 60 ℃ (line 7), 70 ℃ (line 8), and 80 ℃ (line 9). (b) AFM images of aptamer-attached DNA origami assembled by two-step annealing at 25, 53, and 80 ℃.

Recognizing ability of aptamer-attached DNA origamis was demonstrated by QCM measurement for aptamer-protein interaction. The obtained frequency shifts were compared to determine a suitable assembling method. In this experiment, aptamer-attached DNA origami was anchored in advance on the electrode of QCM-based sensor. 5 μg/mL of AFP was used as an analyte. Fig. 5-7 (a) showed the frequency shifts on aptamer-protein interaction using several 72 aptamer-attached DNA origami. The maximum frequency shift of 25 Hz was obtained by using the one-pot assembled 72 aptamer-attached DNA origami. In a case of 72 aptamer-attached DNA origami by 2-step annealing at 25℃, the protein did not interact efficiently with the aptamers although 10 Hz of the frequency shift was obtained. On other measurements using 72 aptamer-attached DNA origami by 2-step annealing at 53 and 80 ℃, the interaction was slightly detected. Staple strands to capture aptamers could be dissociated during over 53 ℃ annealing, as shown in AFM images. Therefore, some residue of aptamer in DNA origami caused slight interaction. The efficiency of aptamer-protein interaction was also confirmed by using 36 aptamer-attached DNA origami, as shown Fig. 5-7 (b). These results indicated that the one-pot assembling method was suitable for aptamer-attached DNA origamis with several aptamers ranging from 0 to 166.

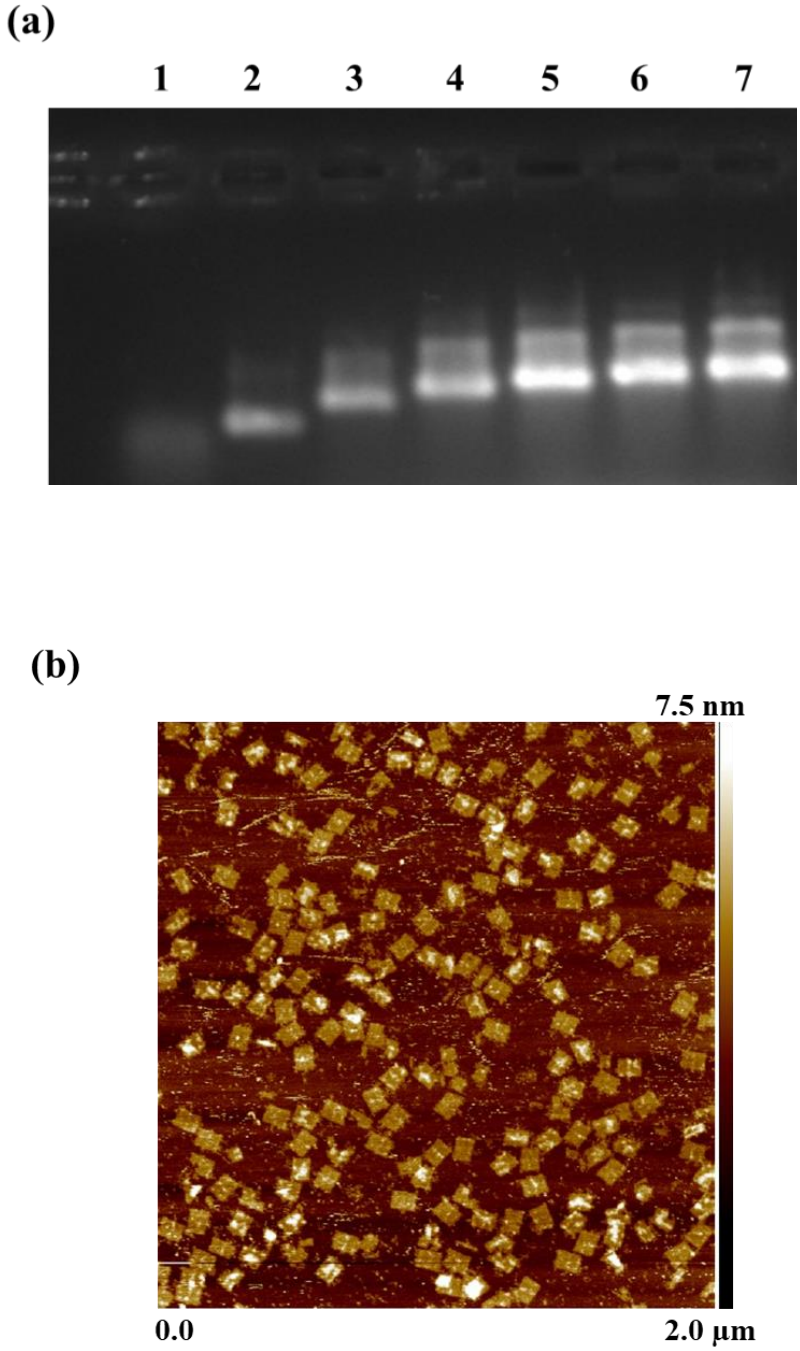

Fig. 5-6 (a) AGE images of aptamer-attached DNA origami with several aptamers by one-pot assembly. Each sample in line were represented following; line 1: M13 scaffold, and line 2, 3, 4, 5, 6, and 7: 0, 36, 72, 108, 138, 166 aptamer-attached DNA origami, and (b) AFM image of 72 aptamer-attached DNA origami by one-pot assembly.

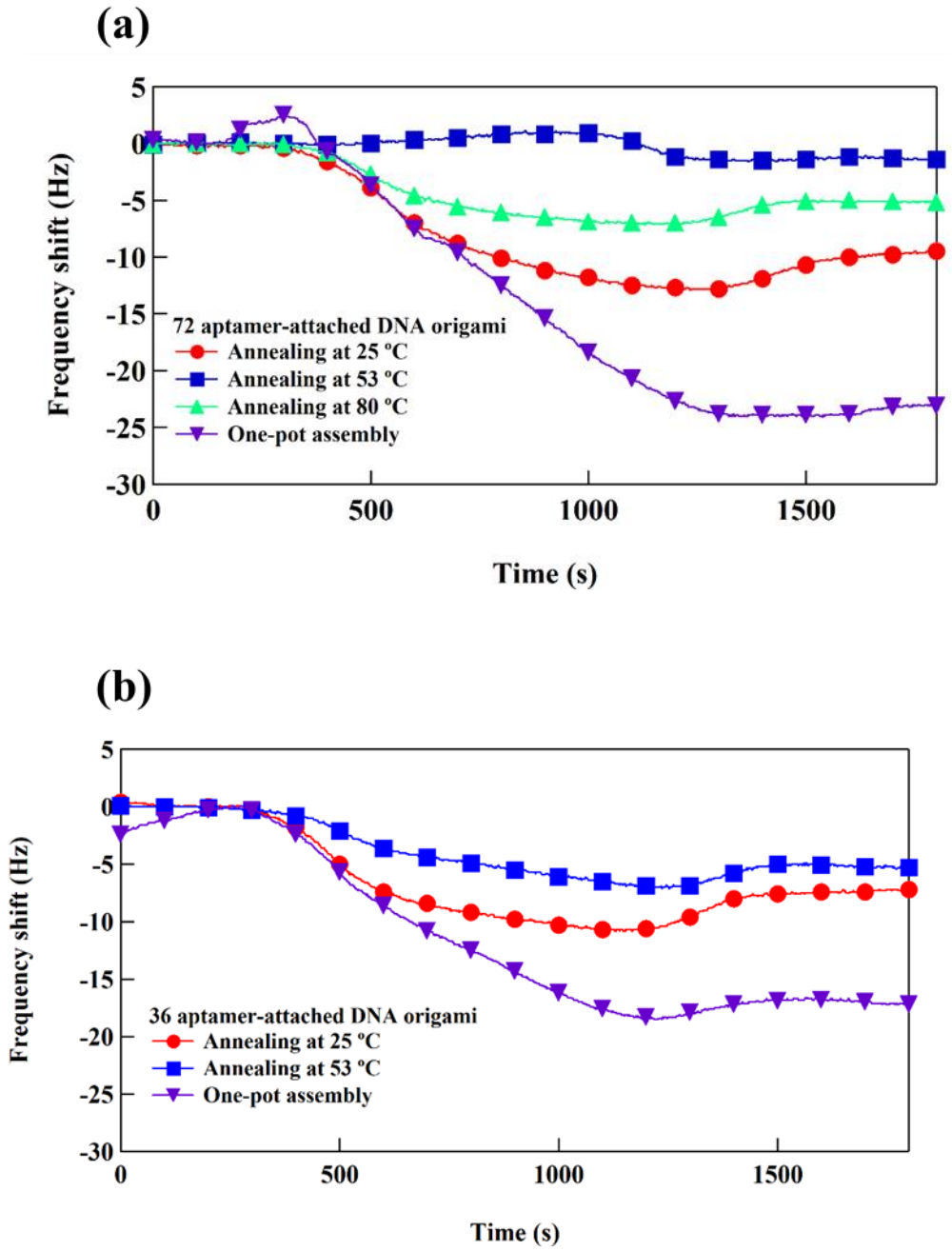

Fig. 5-7 Comparison of frequency shifts on aptamer-protein interaction using 72 (a) and 36 (d) aptamer-attached DNA origamis assembled by two assembling methods.

5.6 Optimization of aptamer attached DNA origami for QCM measurement to detect aptamer-protein interaction

Aptamers can be attached to DNA origami, ranging from 0 to 166. The aptamer-protein interaction would depend on the number of aptamers on DNA origami. Therefore, QCM measurement was performed to investigate an optimal amount of aptamer on DNA origami for aptamer-protein interaction. In this experiment, aptamer-attached DNA origami was immobilized in advance on the gold electrode surface via thiol modified anchoring DNA. Phosphate+200 mM NaCl buffer solution was flowed with 10 μL/min by a flow injection system as a carrier buffer. The aptamer-protein interactions on several aptamer-attached DNA origamis were measured by loading 5 μg/ml of AFP, and then the frequency shifts were compared to determine an optimal aptamer-attached DNA origami. Fig. 5-8 showed frequency shift of aptamer-protein interaction depended on the number of aptamers on DNA origami. In all case using aptamer-attached DNA origami, the frequency shift decreased during passage of the sample solution and then increased slightly by the dissociation of excess of AFP. The frequency shifts after passage of the sample solution were used to analyze the aptamer-protein interaction. The use of directly-modified aptamer provided smaller frequency shift of -22 Hz than aptamer-attached DNA origamis. Especially, the use of 72 aptamer-attached DNA origami provided -40 Hz, which was the two times against the use of directly-modified aptamer. Fig. 5-9 showed distribution of the average frequency shifts dependent on the number of aptamers on DNA origami. The measurements were performed at three times to calculate the standard deviation. The maximum frequency shift was obtained by using 72 aptamer-attached DNA origami. Although increasing the attached aptamers on DNA origami was proved

by AGE image, the magnitude of frequency shift decreased with aptamers, ranging from 108 to 166, on DNA origami.

On considering the decrease, the attachment of a large amount of aptamer onto DNA origami could narrow the spatial distance between each aptamer, and then disturb physically its conformational change. Because the size of the aptamer was around 5 nm, and the minimum pitch between each aptamer was c.a. 4 nm in the design.

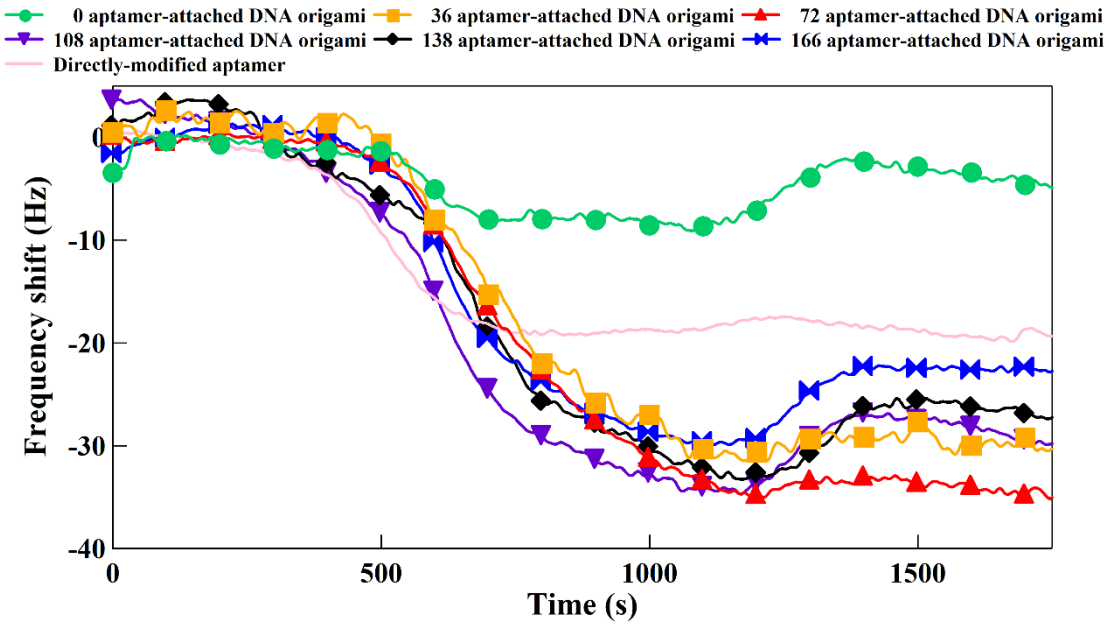

Fig. 5-8 Comparison of frequency shifts on aptamer-protein interaction using aptamer-attached DNA origamis with several aptamers ranged from 0 to 166.

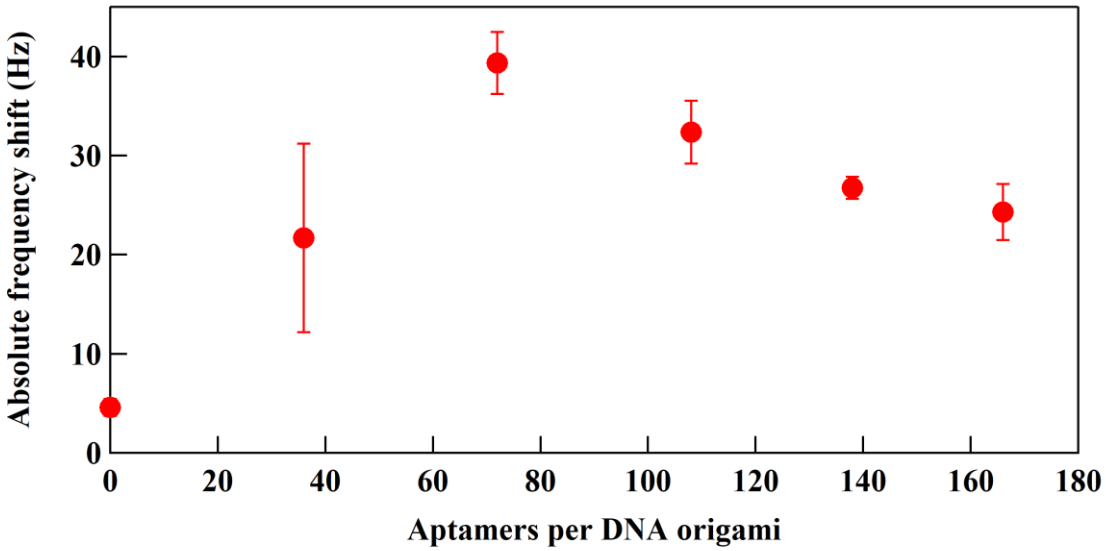

Fig. 5-9 Distribution of frequency shifts depending on the several number of aptamers on DNA origami.

5.7 Redesigning of aptamer position at DNA origami and evaluation of aptamer-protein interaction dependent with its position

A large amount of aptamer on DNA origami strictures could disturb aptamer-protein interaction physically. The positions of aptamers were redesigned to be aligned locally at the center of DNA origami, as shown in Fig. 5-10, and then the special distance between each aptamer was narrowed. In the design, colored symbols indicated the positions of aptamers; pink: 36 aptamers and pink + yellow: 72 aptamers. AGE image of Fig. 5-11 showed a comparison of bands of evenly and locally aligned 72 aptamer-attached DNA origami. The bands of both 72 aptamer-attached DNA origami were placed at the same level. In addition, AFM image of Fig. 5-11 showed well-formed locally aligned 72 aptamer-attached DNA origamis. The locally aligned aptamer-attached DNA origami was successfully assembled equivalent with evenly aligned sample. Fig. 5-12

showed a comparison of frequency shifts on aptamer-protein interaction by using several evenly or locally aligned aptamer-attached DNA origamis. The number of aptamers on DNA origami were 36 and 72 for both alignments. The measurements were performed at three times with the same condition as shown above experiments. The use of locally aligned 72 aptamer-attached DNA origamis provided smaller frequency shifts of -26 Hz comparing to evenly aligned 72 aptamer-attached DNA origamis. This decrease of frequency shift was observed by using locally aligned 36 aptamer-attached DNA origami. The density of aptamer on DNA origami related to the association rate of aptamer-protein interaction. These results proved that evenly aligned 72 aptamer-attached DNA origami was suitable for biosensing application.

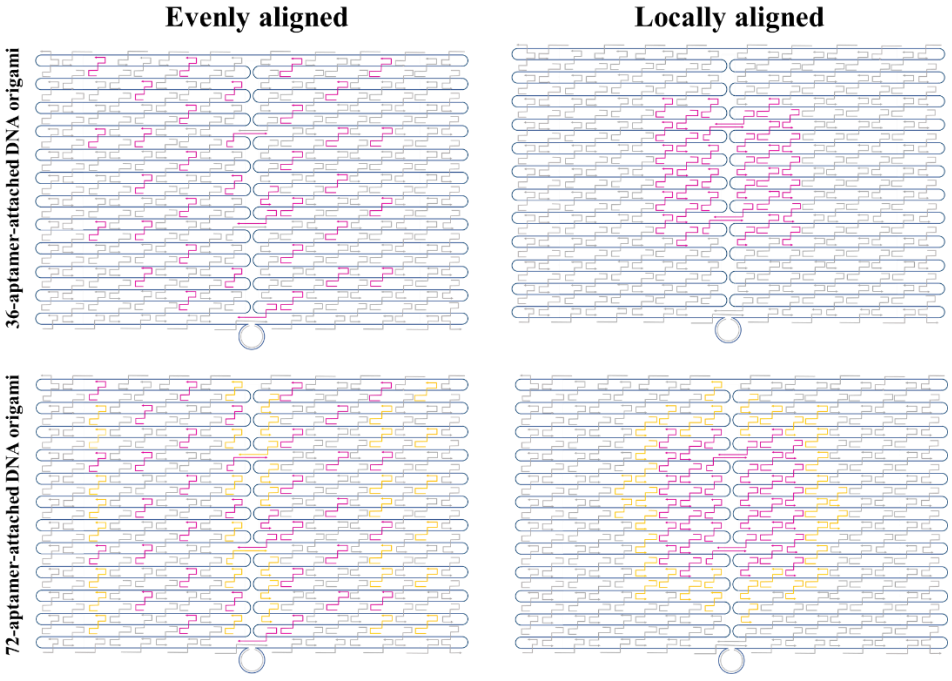

Fig. 5-10 A comparison of redesign of 72 aptamer-attached DNA origami. The position of aptamer was indicated by colored symbol: pink shows the positions of 36 aptamer and both of orange and pink shows the positions of 72 aptamers.

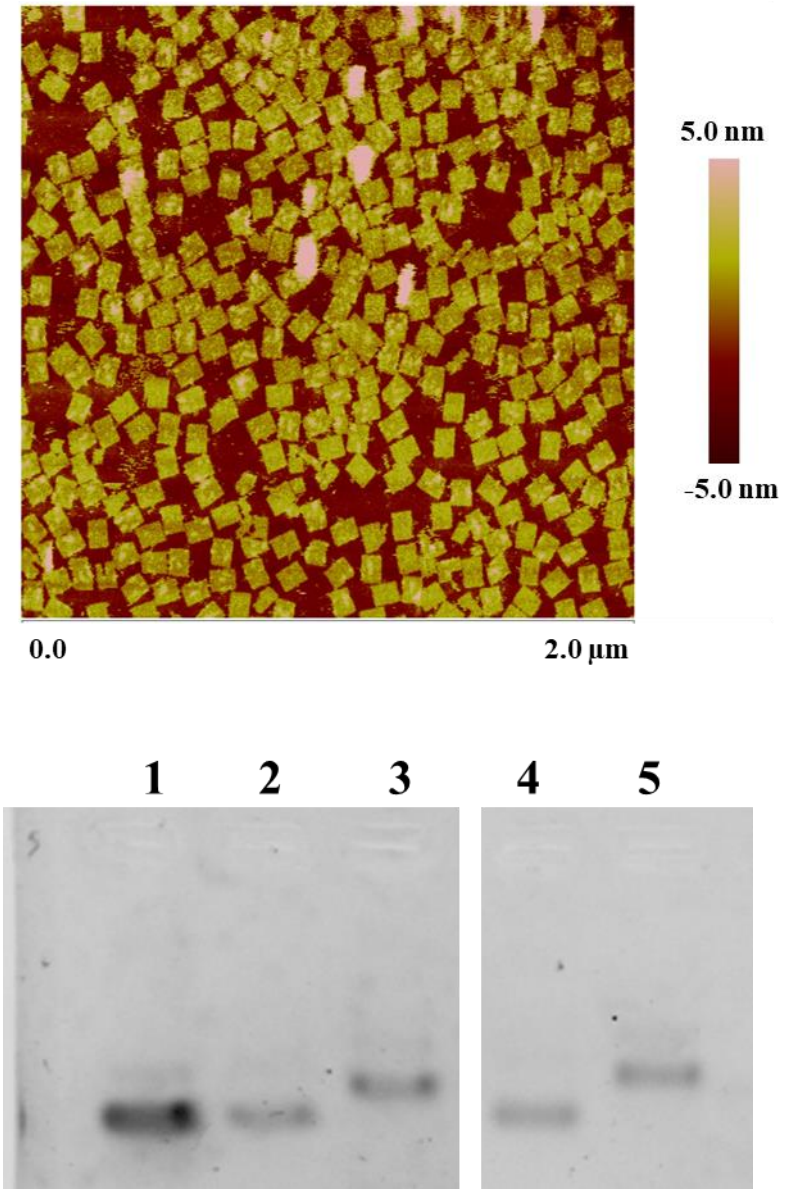

Fig. 5-11 AFM image of locally aligned 72 aptamer-attached DNA origami (top) and AGE images of evenly and locally aligned 72 aptamer-attached DNA origami (bottom). The samples following were loaded in each line: M13 scaffold (line 1), DNA origami 0 apt (line 2), evenly aligned 72 aptamer-attached DNA origami (line 3), DNA origami 0 apt (line 4), locally aligned 72 aptamer-attached DNA origami (line 5).

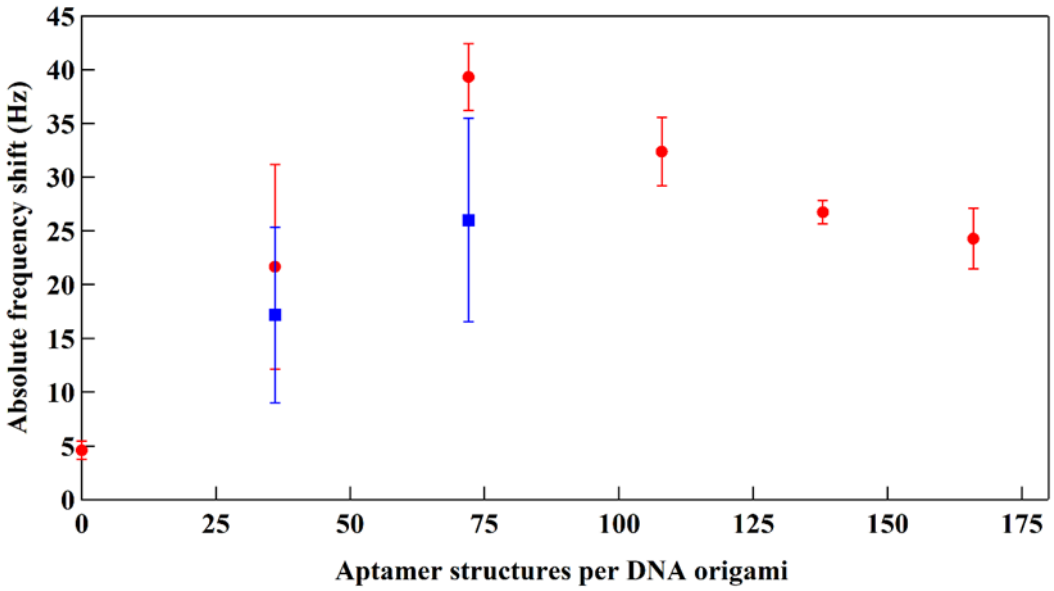

Fig. 5-12 Comparison of frequency shifts by using evenly or locally aligned aptamer-attached DNA origami. Red plot indicated evenly aligned aptamer-attached DNA origami. Blue plot indicated locally aligned aptamer-attached DNA origami.

5.8 Evaluation of aptamer-attached DNA origami for biosensing application.

Fig. 5-13 showed analytical curves of absolute frequency shifts against AFP concentrations. In this experiment, 72 aptamer-attached DNA origami and directly-modified aptamer were coated in advance on the electrode surface of QCM-based sensor. The average frequency shifts were plotted from three times measurements. The AFP concentrations ranged from 0.1 to 5 μg/mL. Error bars show standard deviations. The both absolute frequency shifts increased logarithmically with the AFP concentration from 0.25 to 5 μg/mL, as shown in Fig. 5-13 When logarithmic fitting was applied to the analytical curves, correlation coefficient (R^2) were 0.9961 for 72 aptamer-attached DNA origami and 0.9999 for directly-modified aptamer, respectively. Limits of detection (LOD) were calculated as 0.1 μg/mL for 72 aptamer-attached DNA origami and 0.5

μg/mL for directly-modified aptamer, respectively. On the calculation, signal-to-noise ratio was 3. As the results, the use of aptamer-attached DNA origami improved an efficiency of aptamer binding with target protein.

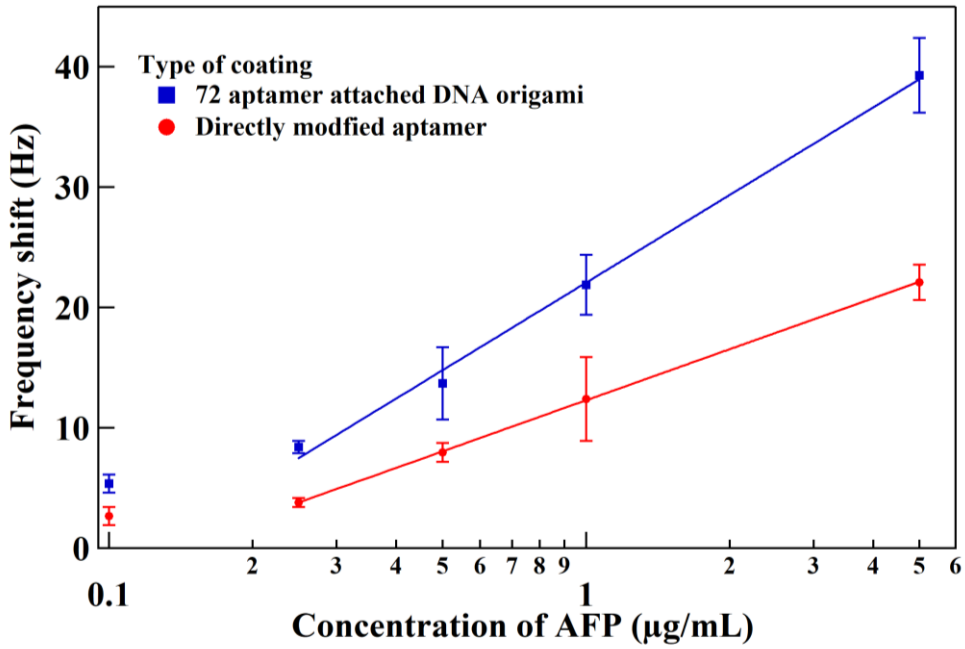

Fig. 5-13 Frequency shifts on aptamer-protein interaction at several concentration of AFP ranged from 0.1 to 5 μg/mL. Blue plot indicated that obtained by 72 aptamer-attached DNA origami, and orange plot indicated that obtained by aptamer-only sensor.

In Table 5-2, an electrical admittance measurement analyzed how many aptamers immobilized on the electrode of both QCM sensors with 72 aptamer-attached DNA origami and directly-modified aptamer. The sensitivity of the QCM sensor was defined as 1.18 ng/Hz. The frequency shift was measured in air phase to analyze the mass loaded of aptamer-attached DNA origami and directly-modified aptamer on the electrode. The admittance measurement in air phase avoided overestimating the mass load by coupled water surrounding both DNA structures. The frequency shifts were divided by 3 because of overtone of 3 at the measurements. For the directly-modified aptamer, the mass loaded

of aptamers was calculated as 125.9 ng. From the mass change divided by its molecular weight: 23212 Da, the mole of aptamers on the electrode was 5.47 pmol. For 72 aptamer-attached DNA origami, the total surface area of DNA origami was calculated as 102.29 mm^2 that was fourfold over the surface area of the electrode. On the calculation of total surface are. the dimension of DNA origami was obtained by AFM imaging. The calculation estimated that the 72-aptamer-attached DNA origami were vertically immobilized against the electrode. The aptamers on DNA origami were calculated as 1.65 pmol from the molecular number of aptamers and the attached DNA origami. The quantity of aptamers on DNA origami was smaller than that of the directly-modified aptamer. However, the use of 72-aptamer-attached DNA origami provided the more massive frequency shifts on aptamer-protein interaction. As mentioned in Fig. 5-9 and 5-12, the density of aptamers on DNA origami related to the association rate of aptamer-protein interaction. Therefore, movable ranges, which is surface area enabling conformational change, of aptamers were estimated in both cases of 72 aptamer-attached DNA origami and directly-modified aptamer. The movable range of 72 aptamers on DNA origami was calculated as 79.02 nm^2 from dividing the surface area by the number of aptamers (72). In the case of directly-modified aptamer, the movable range of aptamers was calculated as 6.012 nm^2 from dividing an electrode area by the number of attached aptamers. Additionally, the diameter of directly-modified aptamer was also calculated as 2.76 nm equivalent mostly to double helix structure of DNA. Thus, the electrode surface was fully covered by aptamers without significant space for conformational change. These results proved that movable range of aptamer influenced on the association rate of aptamer-protein interaction. The use of aptamer-attached DNA origami provided large movable range of aptamer and improved the association rate of aptamer-protein

interaction.

Table 5-2 Analysis of immobilization of aptamer-attached DNA origami and directly-modified aptamer on an electrode of QCM-based sensor, and evaluation of movable ranges of aptamer.

	Unit	72 aptamer-attached DNA origami	Directly-modified aptamer (100 nM)
Sensitivity	(ng/Hz)	1.18	1.18
Frequency shift	(Hz)	420	320
Frequency shift	(1/3 Hz)	140	106.67
Mass loaded	(ng)	165.2	125.867
Molecular weight	(Da)	7201677	23212
DNA origami area	(nm^2)	5689.6	
Attached number	(pmol)	0.023	5.422
DNA origami attached number	(-)	13809339130	
Aptamer	(pmol)	1.65	5.42
Aptamer number	(-)	9.94×10^{11}	3.26×10^{12}
Electrode area	(mm^2)	19.625	19.625
Aptamer movable range	(nm^2)	79.02	6.012

5.9 Conclusions

Aptamer-attached DNA origami was applied as recognition elements to detect efficiently aptamer-protein interaction. Three types of DNA origamis were assembled with no, flexible, and adhesive anchoring extensions. QCM measurement investigated the anchoring of DNA origami onto an electrode surface of a QCM-based sensor. DNA origamis with adhesive or flexible anchoring extensions were immobilized onto the electrode via thiol modified anchoring DNA. The flexible anchoring extension enhanced efficiency of hybridization between DNA origami and thiol modified anchoring DNA. From the demonstration of assembly, one-pot assembly method was successful in assembling aptamer-attached DNA origami with several aptamers ranged from 0 to 166.

QCM measurement on an interaction between AFP and aptamer showed the frequency shifts depended on the number of aptamers on DNA origami. A QCM-based sensor with 72-aptamer-attached DNA origami was employed as recognition elements in QCM measurement. Because the sensor using 72 aptamer-attached DNA origami provided the maximum frequency shift on the aptamer-protein interaction. The maximum frequency shift was -40 Hz larger than -25 Hz when aptamer was directly modified on the sensor electrode. The sensing performances were investigated by measuring frequency shifts depending on several AFP concentrations. QCM-based sensor with 72 aptamer-attached DNA origami had 0.9961 of correlation coefficient ranged from 0.25 to 5 μg/mL, and the limit of detection was 0.13 μg/mL. These sensing performances were more excellent than those of QCM-based sensors with directly-modified aptamers.

However, the magnitude of frequency shift decreased depending on the number of aptamers from 72 to 166. The positions of aptamers were redesigned to demonstrate distance of aptamer dependent on the interaction. The local alignment of 72 aptamers

decreased the frequency shift to -25 Hz. This decrease in frequency shift was also obtained by local alignment of 36 aptamers. These results showed the locally aligned aptamers on DNA origami disturbed physically aptamer-protein interaction. An admittance measurement analyzed the mass loaded of 72 aptamer-attached DNA origami and directly-modified aptamer to compare quantity of aptamer. Although the quantity of directly-modified aptamer was larger than 72 aptamers on DNA origami, the movable range was oppositely varied. 72 aptamers on DNA origami had 10-folds range comparing that of directly-modified aptamer. Therefore, the density of aptamer on DNA origami related to the association rate of aptamer-protein interaction. The accurately aligned aptamer influenced the association rate of aptamer-protein interaction. The results in this chapter showed that 72 aptamer-attached DNA origami contributed to detect aptamer-protein interaction by making significant space for conformational change of aptamer.

References

5-1	N. Asai, T. Shimizu, S. Shingubara, and T. Ito, Fabrication of highly sensitive QCM sensor using AAO nanoholes and its application in biosensing. Sens. Actuators B Chem., 2018 276, 534-539.
5-2	H. Ahmed, Nanostructure fabrication. IEEE Proc., 1991 79, 1140-1148.
5-3	N. Asai, H. Terasawa, T. Shimizu, S. Shingubara, and T. Ito, Highly sensitive quartz crystal microbalance based biosensor using Au dendrite structure. Jpn. J. Appl. Phys., 2018 57, 02CD01.
5-4	E. Winfree, F. Liu, L. A. Wenzler, N. C. Seeman, Design and self-assembly of two-dimensional DNA crystals. Nature, 1998, 394, 539
5-5	H. Chandran, A. Rangnekar, G. Shetty, E. A. Schultes, J. H. Reif, and T. H. LaBean, An autonomously self-assembling dendritic DNA nanostructure for target DNA detection. Biotechnol. J., 2013 8, 221–227
5-6	Wenjing Wang, Sha Yu,a Shan Huang, Sai Bi, Heyou Han, Jian-Rong Zhang, Yi Lu and Jun-Jie Zhu Bioapplications of DNA nanotechnology at the solid–liquid interface. Chem. Soc. Rev., 2019, 48, 4892
5-7	Y. Zhao, H. Wang, W. Tang, S. Hu, N. Li and F. Liu, An *in situ* assembly of a DNA–streptavidin dendrimer nanostructure: a new amplified quartz crystal microbalance platform for nucleic acid sensing. Chem. Commun., 2015, 51, 10660-10663.
5-8	M. Godonoga, T. Lin, A. Oshima, J. G. Heddle A DNA aptamer recognising a malaria protein biomarker can function as part of a DNA origami assembly. Sci. Rep., 2016 6, 21266.
5-9	L. Dong, Q. Tan, and W. Ye. Screening and Identifying a Novel ssDNA Aptamer against Alpha-fetoprotein Using CE-SELEX. Sci. Rep. 2015 5, 15552.
5-10	S. M. Douglas, A. H. Marblestone, S. Teerapittayanon, A. Vazquez, G. M. Church, and W. M. Shih, Rapid prototyping of 3D DNA-origami shapes with caDNAno. Nucleic Acids Res., 2009 37, 5001–5006.

Chapter 6: Achievement of this thesis

In this thesis, four kinds of nanostructure were employed to improve sensing performances of QCM based-sensor. In the sensing principle of QCM measurement, a surface area of electrode is proportional to the sensitivity. Since nanostructures have large surface area, many analytes can be absorbed onto the surface of nanostructures. Therefore, the sensitivity could be improved by formation of nanostructures onto to the electrode surface.

In chapter 2, 3, and 4, three inorganic nanostructures were fabricated on the electrode by different convenient wet-processes. In chapter 5, DNA origami, which is one of DNA nanostructure was formed with self-assembly. Here, fabrication methods of these nanostructures and its contribution to the sensing performances were summarized below.

Chapter 2

Two different Au nanostructures were obtained according to the applied potential on anodizing of a gold electrode of QCM-based sensor. Sponge-like Au nanostructures were formed by applying potential over 3 V. Low applied potential with 2 V formed sphere-like Au nanostructure. Although sponge-like Au nanostructures had large surface area in apparent as observed by SEM, the effective surface areas of every sponge-like Au nanostructures were smaller than that of Au nanosphere on electrochemical measurement. In addition, the structural strength of the sponge-like Au nanostructure was so fragile that the structure dissociated from the electrode by flowing buffer. Therefore, the Au nanosphere was used to improve the sensitivity of QCM-based sensor.

Chapter 3

Au dendrite nanostructure was fabricated on a gold electrode surface by electroplating. Several electroplating conditions varied the morphology of Au dendrite nanostructure. Therefore, the condition to obtain a dendrite Au nanostructure with numerous branching was optimized. As the results of optimization, applied potential of 2V and PEG1000 concentration of 50 ppm were suitable to form Au dendrite structure. However, the numerous branching decreased the sensitivity and precision in QCM measurement. When a tall dendrite structure was vertically formed on the electrode, the large noise occurred in the measurement due to high resonant resistance. Therefore, short Au dendrite nanostructure was electroplated on the electrode of QCM-based sensor to improve the sensitivity.

Chapter 4

AAO nanostructure was fabricated by anodizing aluminum film pre-deposited as an electrode of QCM-based sensor. Several fabricating conditions varied the nanohole diameter and depth of AAO nanostructure. The optimal dimensions of AAO nanostructure on QCM measurement were 60 nm in diameter and 700 nm in depth. The sensitivity of QCM-based sensor was improved five times by optimizing the condition of AAO nanostructure. The large surface area, low density, and high material rigidness of AAO nanostructure contributed to the improvement of the sensitivity from 0.48 to 0.20 μg/mL in mouse IgG concentration. In addition, AAO-nanostructured QCM-based sensor was used to evaluate PPIs using Bax and Bcl-2. The AAO-nanostructured QCM-based sensor detected successfully the interaction with significant frequency shift. Therefore,

the dissociation rate constant was calculated as 53.5 nM from the increased frequency shift.

Chapter 5

Aptamers were integrated into DNA origami to capture many target AFP. One-pot assembly of aptamer-attached DNA origami allowed 0-166 aptamers to incorporate efficiently into DNA origami. The number of aptamers on DNA origami was optimized to detect aptamer-protein interaction on QCM measurement. The frequency shifts increased with the aptamers ranged from 0 to 72 in aptamer-attached DNA origamis. However, frequency shifts decreased by using over 108 aptamer-attached DNA origami. The use of 72 aptamer-attached DNA origami produced -40 Hz, which was the maximum frequency shift. A sensitivity of QCM-based sensor was improved from 0.55 to 0.13 μg/mL by using 72 aptamer-attached DNA origami.

Position of aptamer on DNA origami was redesigned to investigate how density of aptamers on DNA origami affected on the interaction. Large quantity of aptamer was attached on DNA origami in case of 108, 138, and 166 aptamer-attached DNA origamis. By redesigning, 72 aptamers on DNA origami were locally aligned at the center. As the result, the sensitivity on aptamer-protein interaction was decreased by localizing the positions of aptamers in 72 aptamer-attached DNA origami. An admittance measurement also showed the density of aptamers related to the association of aptamer-protein interaction. 72 aptamer-attached DNA origami contributed to detect aptamer-protein interaction by making significant space for conformational change of aptamer.

As conclusions, the sensing performance of QCM-based sensor was improved by using AAO nanostructure and aptamer-attached DNA origami. However, some problems are still remained in application of them. An ideal nanostructure to improve the sensing performance should have high uniformity, high biocompatibility, high material rigidness, low density, large surface area, enough space for capturing analyte, and so on. Looking to application to other biosensor, good conductivity and optical property are also required. However, it is difficult to fabricate a perfect nanomaterial. If such nanomaterial is developed and applied to any biosensor, that will contribute to detail analysis of biological phenomena deeply.

Chapter 7: List of publications

Accepted journals

Peer-reviewed		
1	"Nano-honeycomb electrode based QCM sensor and its application for PPI detection," IEEE Sensors Journal, vol. 19, pp. 4025-4030, 2019	**N. Asai**, N. Matsumoto, N. Kazama, Y. Nagaoka, T. Sumiyoshi, T. Shimizu, S. Shingubara, and T. Ito
2	"Fabrication of highly sensitive QCM sensor using AAO nanoholes and its application in biosensing," Sensors and Actuators B Chemical, vol. 276, pp. 534-539, 2018	**N. Asai**, T. Shimizu, S. Shingubara, and T. Ito
3	"Highly sensitive quartz crystal microbalance based biosensor using Au dendrite structure," Japanese Journal of Applied Physics, vol. 57, pp. 02CD01, 2018	**N. Asai**, H. Terasawa, T. Shimizu, S. Shingubara, and T. Ito
4	"Sensitized mass change detection using Au nanoporous electrode for biosensing," Japanese Journal of Applied Physics, vol. 56, pp. 06GG04, 2017	**N. Asai**, H. Terasawa, T. Shimizu, S. Shingubara, and T. Ito
5	"Fabricating a QCM Device with the Nanostructures Using the AAO Template," ECS Transaction, vol. 75, pp. 229-232, 2016	**N. Asai**, T. Ito, T. Shimizu, and S. Shingubara,
No peer-reviewed		
1	"Fabricating a Highly Sensitive QCM Sensor Using AAO Nanoholes and Its Application for Biosensing," Proceeding, vol. 1, pp. 495, 2017	**N. Asai**, T. Shimizu, S. Shingubara, and T. Ito

Related articles

1	"Fabrication and characterization of nano porous lattice biosensor using anodic aluminum oxide substrate," Japanese Journal of Applied Physics, vol. 56 pp. 06GG02, 2017	T. Ito, Y. Mastuda, T. Zinba, **N. Asai**, T. Shimizu, S. Shingubara
2	"Nonenzymatic detection of glucose using BaCuO 2 thin layer," Japanese Journal of Applied Physics, vol. 56, pp. 01AH02, 2017	T. Ito, T. Asada, **N. Asai**, T. Shimizu, S. Shingubara
3	"Antibacterial Property of Si Nanopillar Aray Fabricated using Metal Assisted Etching; Mimic a Cicada Wing," ECS Transaction, vol. 75, pp. 1-5, 2017	T. Ito, K. Nakde, **N. Asai**, T. Shimizu, S. Shingubara
4	"Electrodeposited ZnO thin Film on twin sensor QCM for Sensing of Ethanol at Room Temperature," Procedia Engineering, vol. 168, pp. 411-414, 2016	T. Ito, Y. Fujii, N. Yamanishi, **N. Asai**, T. Shimizu, S. Shingubara

Presentations at international conferences

1	(Invited Oral) **N. Asai**, Y. Sakai, J. Heddle, T. Tomohiro, S. Shingubara, T. Ito, "Investigation of a cancer biomarker-aptamer attached DNA origami interaction by QCM and its application for biosensor", EMRS2019 Fall, Warsaw, Poland, 2019.
2	(Poster) **N. Asai**, Y. Sakai, J. Heddle, T. Tomohiro, S. Shingubara, T. Ito, "Detecting cancer biomarker using DNA origami nanoarray", M&BE 10, Nara, Japan, 2019.
3	(Poster) **N. Asai**, N. Matsumoto, N. Kazama, Y. Nagaoka, T. Sumiyoshi, T. Shimizu, S. Shingubara, T. Ito, "Highly sensitive detection of Bcl-2 and Bax interaction by nano-honeycomb electrode-based QCM sensor" The 3rd international Workshop by the 174th Committee JSPS "Symbiosis of Biology and Nanodevices", Nara, Japan, 2019.
4	(Invited Poster) **N. Asai,** T. Shimizu, S. Shingubara, T. Ito, "Fabrication of highly sensitive QCM sensor with a nano-honeycomb structure and the demonstration for biosensing", EMRS2018 Fall, Warsaw, Poland, 2018.
5	(Poster) **N. Asai**, Y. Sakai, J. Heddle, "Biosensor nanoarray with amplified sensor output by DNA origami", Bionano2018, Krakow, Poland, 2018.
6	(Poster) **N. Asai**, T. Shimizu, S. Shingubara, T. Ito, Fabricating a Highly Sensitive QCM Sensor Using AAO Nanoholes and Its Application for Biosensing, Eurosensors2017, Paris, France, 2017.
7	(Oral) **N. Asai**, H. Terasawa, T. Shimizu, S. Shingubara, T. Ito, Highly sensitive QCM based biosensor using Au dendrite structure, EM-NANO 2017, Fukui, Japan, 2017
8	(Poster) **N. Asai**, T. Ito, T. Shimizu, S. Shingubara, Fabricating a QCM device with the nanostructures using the AAO template, PRiME 2016, Honolulu, USA, 2016

Presentations at domestic conferences

1	(Oral) **N. Asai**, Y. Sakai, J. Heddle, I. Yamashita, T. Tomohiro, S. Shingubara, T. Ito, Biosensor with DNA origami-nanoarray for detection of cancer biomarker, The 67th JSPS Spring Meeting, 2019
2	(Oral) **N. Asai**, T. Shimizu, S. Shingubara, T. Ito, Improvement of a sensitivity of QCM-based sensor by anodic aluminum oxide nanostructure for biosensing application, The 85th ECSJ Spring Meeting, 2018
3	(Poster) **N. Asai**, T. Shimizu, S. Shingubara, T. Ito, Fabrication of nanostructured QCM sensor, The 34th Symposium of Sensor/Micromachine and Applied system, 2017
4	(Oral) **N. Asai**, T. Shimizu, S. Shingubara, T. Ito, Fabrication of anodic aluminum oxide nanostructured QCM sensor, The 64th JSAP Spring meeting, 2017
6	(Oral) **N. Asai**, T. Shimizu, S. Shingubara, T. Ito, Fabrication of QCM sensor with anodized gold nanostructure, The 83th ECSJ Spring Meeting, 2016
7	(Poster) **N. Asai**, T. Shimizu, S. Shingubara, T. Ito, Fabrication of QCM sensor with controllable nanostructure by using AAO template, The 77th JSAP Autumn meeting, 2016

Chapter 8: Acknowledgement

The studies in this thesis were partially supported by below foundations and programs.

The Formation of Research Center Project at Kansai University.

The MEXT Supported Program for the Strategic Research Foundation at Private Universities, “Creation of 3D nano-microstructures and their application to biomimetics and medicine,” 2015–2019.

The Murata Science Foundation.

POLONEZ3 (2016/23/P/NZ1/04097) of Polish National Science Centre (NCN)

co-funded by the Marie Skłodowska-Curie action of the European Union (665778)

本学位論文を執筆するにあたり，研究および研究生活を支えてくださいました皆様にこの場を借りて厚く御礼申し上げます.

私という不出来かつ扱いづらい学生を，修士課程時代から 5 年間も熱心な指導をしていただきました指導教員である伊藤健教授に心から感謝いたします．留学や共同研究など多種多様な研究生活をおくることができたのは，伊藤健教授のご助力のおかげと心得るとともに，その機会を与えていただいたことに再度感謝いたします．私のサイエンスへの考え方や論文の書き方など，まだ至らぬ点が多いと存じますが，伊藤健教授にご指摘いただいたことを胸に秘め，これからの研究活動に邁進する所存です．また，学部生時代からの 6 年間ご指導いただいた新宮原正三教授，清水智弘准教授の両氏に深く感謝いたします．学部生時代の私は，非常に不真面目で研究室に来ない日々でした．それにも関わらず，熱心なご指導をしていただき，大学院進学を許可していただいたことに深く感謝いたします.

博士課程の間，私をリサーチアシスタントとして雇用していただいた関西大学システム理工学部機械工学科ロボット・マイクロシステム研究室の青柳誠司教授に深く感謝いたします．また，同研究室所属かつ関西大学 HRC クリーンルーム実行委員として実験環境の整備などでお世話になりました，鈴木昌人准教授，高橋智一准教授に

深く感謝いたします.

AAOナノ構造化センサを持ちいたタンパク質間相互作用の検出の共同研究でお世話になった関西大学化学生命工学部生命・生物工学科医薬品工学研究室の長岡康夫教授と住吉孝明准教授の両氏に深く感謝いたします．この共同研究を通して，タンパク質間相互作用への知見が深まり，結果的に本学位論文の質も向上いたしました．特に，本学位論文の副査を快く引き受けていただきました長岡康夫教授に心から感謝いたします.

他大学の学生にも関わらず，3 年以上も熱心なご指導をしていただきました大阪大学大学院工学研究科の山下一郎教授に心から感謝いたします．山下一郎教授のサイエンスへの厳格な姿勢は，今後の研究生活を邁進する上で非常に勉強になりました．加えて，山下一郎教授の紹介がなければ，私の留学はそもそも実現していませんでした．私の人生を変えるチャンスをくださった人たちの一人といっても過言ではありません．ここに重ねて感謝いたします.

留学先である Heddle lab, Malopolska Centre of Biotechnology, Jagiellonian University, Poland の Prof. Jonathan Heddle 氏と同研究室に所属している酒井雄介博士研究員の両名に感謝の意を表します．特に酒井雄介氏には，実験面からコミュニケーション面まで面倒を見ていただき非常に感謝しています．英語ができないまま留学したために，非常に意思疎通が難しい状況のなか，快く協力いただいた Heddle lab の全メンバーにも感謝いたします.

ポーランドから帰国後，DNA origami 用の実験環境を設備することができなかったために，関西大学化学生命工学部化学・物質工学科知能分子学研究室の葛谷明紀教授のご助力をお借りしました．葛谷明紀教授のご助力がなければ，日本で実験を再開することは難しく，この学位論文も完成しなかったと存じます．ここに葛谷明紀教授への深い感謝の意を表します.

ナノ機能工学研究室(旧応用物理研究室)で出会った先輩方と後輩に深く感謝いたします．優秀だった彼らと議論を交わすことは，固まった思考を凝りほぐす良い刺激となりました.

最後に， 27 年間迷惑をかけ続けてきたにも関わらず，生活を支えてくれた両親と姉に心から感謝いたします.